Optische signaalmonitoring en regeneratie
op basis van optische versterkerschakelingen

All-Optical Signal Monitoring and Regeneration
Using SOA-Based Circuits

Sam Verspurten

Promotoren: prof. dr. ir. G. Morthier, prof. dr. ir. R. Baets
Proefschrift ingediend tot het behalen van de graad van
Doctor in de Ingenieurswetenschappen: Elektrotechniek

Vakgroep Informatietechnologie
Voorzitter: prof. dr. ir. P. Lagasse
Faculteit Ingenieurswetenschappen
Academiejaar 2005 - 2006

UNIVERSITEIT
GENT

ISBN 90-8578-082-9
NUR 959
Wettelijk depot: D/2006/10.500/40

Promotoren:

Prof. dr. ir. G. Morthier	Universiteit Gent, INTEC
Prof. dr. ir. R. Baets	Universiteit Gent, INTEC

Examencommissie:

Prof. dr. ir. R. Verhoeven (voorzitter)	Universiteit Gent, Civiele Techniek
Prof. dr. ir. J. Vandewege (secretaris)	Universiteit Gent, INTEC
Prof. dr. ir. H. De Waardt	TU/e Eindhoven
Prof. dr. ir. J. Vanfleteren	Universiteit Gent, ELIS
Prof. dr. ir. G. Morthier	Universiteit Gent, INTEC
Prof. dr. ir. R. Baets	Universiteit Gent, INTEC
Prof. dr. ir. P. Bienstman	Universiteit Gent, INTEC

Universiteit Gent
Faculteit Ingenieurswetenschappen

Vakgroep Informatietechnologie (INTEC)
Sint-Pietersnieuwstraat 41
B-9000 Gent
België

Tel.: +32-9-264.33.24
Fax: +32-9-264.35.93
http://www.intec.ugent.be

Dit werk kwam tot stand in het kader van een specialisatiebeurs van het IWT - Instituut voor de Aanmoediging van Innovatie door Wetenschap en Technologie in Vlaanderen.

This work was carried out in the context of a specialization grant from the Flemish Institute for the Industrial Advancement of Scientific and Technological Research (IWT).

Voorwoord

Hoewel ik eerder denk dat de mensen die ik zou willen bedanken dit wel weten, volgt hier dan toch een kort dankwoordje. Na 5 jaar in het Technicum te hebben gekampeerd zijn er natuurlijk een heleboel mensen de revue gepasseerd.

Vooreerst wil ik natuurlijk Prof.Lagasse bedanken voor het bestaan van INTEC en voor het feit dat ik hier deel mocht van uit maken.
Geert en Roel wil ik bedanken voor de geboden kans een vervolg te breien aan onze thesis en voor het promotorschap van dit werk. Vooral bij Geert kon ik te pas en te onpas efkes den bureau binnenlopen met grote dan wel kleine problemen. Vooral de laatste jaren heeft dit mij op bepaalde momenten toch (al wou ik het zelf niet altijd onmiddellijk geloven) goed vooruit geholpen. Thanx!! Ook wil ik de juryleden van lees- en examencommissie van harte bedanken de moeite te doen dit werk eens door te nemen.

Op gebied van "lotgenoten" die ook actief waren in de optische signaalverwerkingstak kan ik spijtig genoeg vrij kort zijn. Ongetwijfeld de meeste (en beste) hulp heb ik gekregen van Jan, die spijtig genoeg (voor mij) veel te snel INTEC heeft verlaten! Jan, ongelooflijk bedankt voor alle kleine en grote tips en je mag het gerust weten: ik heb u (en uw ervaring) gemist ze!! I would also like to thank Mingshan for all the very useful measurement tips. I'm very glad for him that now he's reunited with his family such that he can use their support in times of need! Als laatste SOA-fellow hebben we natuurlijk handy-man D'oos. Wreed bedankt voor alle hulp bij de metingen, VPI, soldeerwerk, inkoppeling en nog veel meer. Hou het SOA-werk nog efkes levend hé op den INTEC! Wij gaan zeker nog wel wat terraskes doen.
Massive respect goes out to "measurement"-Hendrik! Big it up for yourself, Aight!!! Veel succes in je nieuwe studie-avontuur en tot op de Gentse Feesten.

De mensen waarmee je het grootste deel van de dag mee doorbrengt zijn natuurlijk je bureaugenoten. In het begin werd ik als groentje gedropt bij allemaal ervaren ratten. Moet zeggen dat ik dit (meestal ;)) wel de max vond. Had mijzelf eigenlijk geen betere plaats binnen INTEC kunnen bedenken. De mix van dat eerste bureau-gezelschap was zalig, al leidde dit in vele gevallen tot zeer hoog oplaaiende discussies. Mathias, Danae, Kurt, Vjeeke en Jan, merci en vanaf het moment dat ik een huis heb is het BBQ in mijnen hof! Later in het doctoraat begin je meer en meer te beseffen dat je niet meer de jongste van den hoop bent. Gelukkig mocht het verse bloed er ook best wezen. Ik wens Freddie, John en Peter dan ook het allerbeste voor het vervolg van hun doctoraat. Reinhard, veel succes in je nieuwe job!
Het is natuurlijk onbegonnen werk iedereen bij naam te noemen, dus wil ik iedereen van de groep bedanken voor de companie! De vrijdagavond uitspattingen (met of zonder een zak brood) zal ik ongetwijfeld het meest van al missen. Salut!

Minstens even belangrijk voor het slagen van dit doctoraat zijn de mensen/dingen die het leven buiten het werk kleur gaven. Zo heb ik enorm veel gehad aan mijn ouders en broer die op woensdagavond meestal al bij het binnenkomen konden merken hoe het op mijn werk gesteld was. Ma en pa, bedankt voor alles en je ziet dat het uiteindelijk allemaal wel in orde komt he! XXX

Ook de uitlaatklep die ik vond gedurende de avonden, nachten en weekends met mijn vriendjes en vriendinnetjes van o.a. de "Leievrienden"-clan was SUPER. Hopelijk mogen er nog vele feestjes e.d. volgen, ook al komen er hier en daar misschien gezinsuitbreidingen....

Last but not at all least wil ik natuurlijk een ongelooflijk grote merci zeggen tegen Annelies. Echt schat, zonder u was ik hier niet geraakt, en dat meen ik!! Hopelijk vinden we in de toekomst alle 2 de juiste weg, en kan dit nog zo lang mogelijk blijven duren, want zo iemand vind ik NOOIT meer!!

Voila, en nu ben ik weg, hasta luego!

Dizzee spittin' for real
Gent, 12 mei 2006

Contents

Nederlandstalige Samenvatting

Dit deel geeft een overzicht van het verrichte doctoraatsonderzoek, tesamen met de belangrijkste behaalde resultaten.

Optische signaalmonitoring

Mede door de toenemende complexiteit van de optische telecommunicatienetwerken is degelijke optische signaalmonitoring heel belangrijk geworden. Een grote variëteit aan technieken kan gebruikt worden om nuttige informatie i.v.m. de signaalkwaliteit te bekomen. Idealiter zou deze informatie de signaalkwaliteit moeten kunnen kwantificeren en daarenboven informatie omtrent de mogelijke oorzaak van een plotse degradatie bevatten.
Er werd reeds verschillende malen aangetoond dat de constructie van een synchroon of een asynchroon histogram bijzonder nuttig kan zijn. Asynchrone histogrammen bezitten de mogelijkheid om degradaties veroorzaakt door optische ruis, chromatische dispersie, overspraak en niet-lineariteiten te detecteren en te identificeren. De zogenaamde "gemiddelde Q-factor", die een logische uitbreiding is van de klassieke (synchrone) Q-factor naar asynchrone histogrammen, bleek in verschillende gevallen een heel bruikbare kwaliteitsparameter te zijn. Vandaar dat het ook deze grootheid is die gebruikt werd gedurende het onderzoek om de nauwkeurigheid van de voorgestelde monitoringsmethode te kwantificeren.

Tot op heden worden signaalhistogrammen altijd geconstrueerd gebruik makend van bemonsteringssystemen, waardoor de configuraties duur en complex worden. In dit werk werd een eenvoudige, goedkope manier voorgesteld om een asynchroon histogram te construeren zonder gebruik te maken van enige bemonsteringssystemen of hoog-

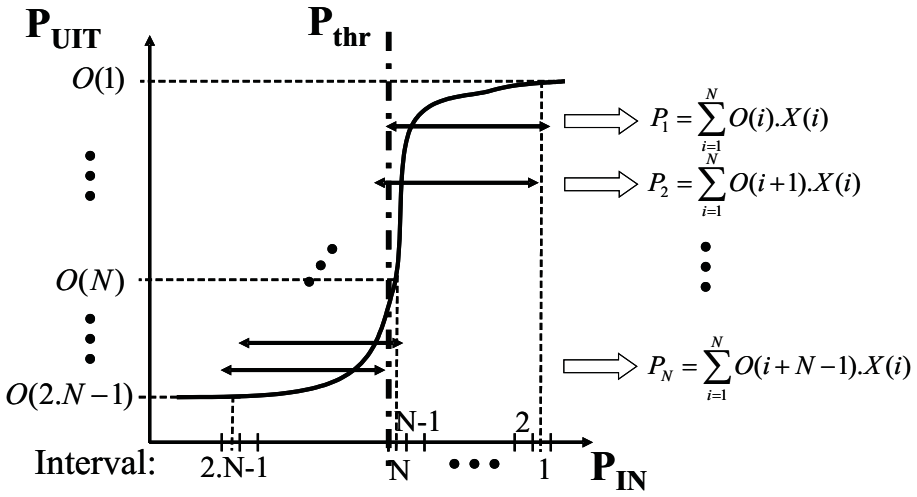

Figuur 1: Het werkingsprincipe van de voorgestelde methode is schematisch weergegeven. De dubbele pijlen duiden telkens het vermogenbereik aan waarin het signaal gelegen is tijdens de constructie van de respectievelijke vergelijkingen.

frequente elektronica.
De methode bestaat uit de constructie van een linear stelsel van vergelijkingen met de probabiliteiten aanwezig in het histogram als onbekenden. De verschillende vergelijkingen worden bekomen zoals schematisch weergegeven in Fig. 1. Het gemiddelde uitgangsvermogen van een snelle sterk niet-lineaire opto-elektronische component wordt gemeten voor verschillende versies van het datasignaal. Deze bestaan uit geattenueerde versies van hetzelfde datasignaal met een toenemende attenuatie. Het is duidelijk dat vanaf het moment dat er meer gemiddelde vermogens zijn opgemeten dan er onbekenden zijn, dan het stelsel in principe opgelost kan worden. Merk op dat enkel **gemiddelde** vermogens hoeven opgemeten te worden.

Aangezien het bekomen stelsel zeer slecht geconditioneerd is, resulteert eenvoudige inversie van de systeemmatrix in extreem onnauwkeurige oplossingen. Daarom werden verschillende oplossingsmethoden onderzocht die de nauwkeurigheid konden verhogen. Regularizatiemethoden, gebaseerd op het introduceren van een zekere beperking van de(semi-)norm van de gevonden oplossing, kunnen de nauwkeurigheid aanzienlijk verhogen. Het bleek dat voor ons probleem de *"afgebroken singuliere waarden ontbinding"* gecombineerd met de *"veralgemeende kruisvalidatie"* ter bepaling van de regularizatieparameter de

meest geschikte methode was. Om de nauwkeurigheid nog verder te verbeteren werden twee minimalisatie methoden ontwikkeld. Deze methoden brachten a priori informatie in rekening m.b.t. de vorm van de histogrammen. De verhoogde extractie nauwkeurigheid ging weliswaar gepaard met een afname van de transparantie van de methode.

Het werd aangetoond dat om een geschikte niet-lineaire configuratie te vinden, het conditiegetal van de resulterende systeemmatrix kon gebruikt worden als een eerste indicatie. Uit een theoretische studie kon worden besloten dat de meest geschikte niet-lineare component een statische transfertkarakteristiek had die een zo steil mogelijke overgang vertoonde en bovendien een zo groot mogelijk relatief verschil in vermogen. Natuurlijk moesten praktische eigenschappen zoals snelheid, stabiliteit, reproduceerbaarheid, e.d. ook in rekening gebracht worden. Het bleek dat de steile overgang bekomen in het uitgangsvermogen van een laserdiode, gekoppeld met een halfgeleiderversterker de meest geschikte kandidaat was voor een praktische implementatie in ons laboratorium.

Uit een uitgebreide theoretische studie kon worden besloten dat gemiddelde Q-factor extractie mogelijk moest zijn indien de statische vermogenskarakteristiek perfect gevolgd werd eenmaal een dynamisch signaal aangelegd werd. Wel moest ook gezorgd worden dat de meetruis voldoende laag werd gehouden. Het werd echter ook snel duidelijk dat een zeer nauwkeurige extractie van de gemiddelde Q-factor sowieso zeer moeilijk zou zijn. Dit is echter een algemeen gekend probleem bij histogram gebaseerde methoden.

Een lage snelheids experimentele opstelling werd gebouwd om de werking van de methode aan te tonen. Hieruit bleek dat een trend in de kwaliteit van het optische signaal zeker kon gemonitored worden. D.w.z. een plotse afname van de kwaliteit van het signaal kan zeker gedetecteerd worden. Dit kan handig zijn aangezien uit de plaats waar dit alarm optreedt waarschijnlijk ook al veel kan afgeleid worden i.v.m. de mogelijke oorzaak van de plotse degradatie. Een nauwkeurige parameter extractie kon echter niet worden bereikt. Dit kwam hoofdzakelijk door een afwijking van het dynamische gedrag van het veronderstelde statische gedrag.
De studie toonde echter wel aan dat indien een zeer snelle niet-lineare component gebaseerd op bijvoorbeeld het Kerr-effect kon worden gebruikt, veel nauwkeurigere resultaten mogelijk moeten zijn.

Kleinsignaal gedrag van twee types van winstvergrendelde halfgeleiderversterkers

In het onderzoek naar verschillende regeneratorconfiguraties, gebruikten we verschillende types winstvergrendelde halfgeleiderversterkers. Dit leidde tot een grondige studie van het kleinsignaal gedrag van twee types. Een theoretische studie werd getoetst aan experimentele resultaten. De twee types winstvergrendelde halfgeleiderversterkers zijn opgebouwd uit een klassieke halfgeleiderversterker in dewelke een lasercaviteit wordt geïntegreerd. In het geval van de GCSOA is dit een longitudinale caviteit, terwijl bij de LOA een verticale caviteit wordt gebruikt. Voor de modellering van de LOA werd een één-dimensionaal tijdsdomein model ontwikkeld, terwijl voor de GCSOA een voorhanden zijnd simulatiepakket kon gebruikt worden.

De versterking van een zwak sinusoïdaal signaal dat voor- resp. achteraan de versterker werd geïnjecteerd werd bestudeerd, terwijl er gelijktijdig een constant sterk optisch signaal werd geïnjecteerd aan de voorkant. In het geval beide aan de voorkant geïnjecteerd werden, werd een duidelijke resonantie waargenomen in de modulatie van het laservermogen en de elektronendichtheid. Dit resulteerde in een dip in de kleinsignaal versterking. De resonantiefrequentie verschoof naar lagere waarden indien meer vermogen werd geïnjecteerd. In het geval van de GCSOA was deze dip veel duidelijker aanwezig t.g.v. de ”zwakke”lokale vergrendeling van de winst. De ”sterke”lokale winstvergrendeling bij de LOA kan de ingangsvermogen variaties beter opvangen.
In het geval de beide signalen in tegengestelde zin propageren bekomen we een vrijwel frequentie onafhankelijke signaalversterking. Dit werd veroorzaakt door de kleinere sterkte van de sinusoïdale component in het deel van de versterker dat het gevoeligst is voor variaties van het ingangsvermogen (i.e. het achterste gedeelte).

In beide injectieschema's gebruikt voor de studie van de kleinsignaal versterking werd de overspraak op een zeer zwak probesignaal onderzocht. Dit probesignaal werd eveneens aan beide kanten van de component geïnjecteerd. Een duidelijke resonantie werd nu waargenomen voor beide types versterkers. Indien het ingangsvermogen van de constante signaalcomponent werd verhoogd had een overgang naar de gekende laagdoorlaat karakteristiek van een normale halfgeleiderversterker plaats. In de GCSOA gebeurde deze overgang heel bruusk, terwijl in de LOA een veel geleidelijkere overgang werd waargenomen.

Voor het probesignaal dat tegen de signaalrichting in propageerde werd een snellere afname van de overspraak waargenomen voor hogere frequenties. Dit is het zogenaamde "walk-off" effect.

In de kleinsignaal versterkingskarakteristieken resulteerden de verschillende vergrendelingsmechanismen duidelijk in een verschillend gedrag, terwijl dit voor de overspraak minder uitgesproken was. Alle bevindingen werden bevestigd door experimenten.

Optische signaal vormverbetering op basis van een eenvoudige MZI

Een nieuwe interferometer configuratie werd voorgesteld bestaande uit één actieve arm met een halfgeleiderversterker en een regelbare attenuator, gecombineerd met een transparante arm. Het voordeel in vergelijking met de volledig actieve uitvoering is het betere regime waarin de halfgeleiderversterker kan gebruikt worden. Deze kan namelijk dieper in verzadiging worden gebruikt, wat een beter dynamisch gedrag oplevert. Indien een lineaire versterker wordt toegevoegd aan de configuratie, kan 2R regeneratie worden bereikt.

Een tijdsdomein halfgeleiderversterker model werd ontwikkeld, rekening houdend met de niet-lineare winstonderdrukking. Dit maakte een theoretische studie van het dynamisch gedrag van de configuratie mogelijk. Er werd aangetoond dat het signaal kon worden omgezet naar een signaal met een duidelijk verbeterde vorm. Dit betrof hoofdzakelijk een verbetering van de extinctieverhouding, gecombineerd met een zekere ruisonderdrukking. De werking tot datasnelheden van 40 Gb/s werd aangetoond indien een geoptimaliseerde halfgeleiderversterker gebruikt kon worden.

Een vezelgebaseerde interferometer gebruik makend van een prototype halgeleiderversterker werd gebouwd om oogdiagrammametingen uit te voeren. Duidelijke extinctieverhoudingsverbetering werd bereikt voor 10 Gb/s signalen, gecombineerd met een klein beetje ruisonderdrukking. BER metingen konden niet worden uitgevoerd t.g.v. de onstabiele aard van een vezelgebaseerde interferometer. Een geïntegreerde versie is momenteel in fabricage.

Summary

An overview of the research performed in the framework of this PhD will now be given, together with the most important results.

All-optical signal monitoring

Due to the increased complexity of optical telecommunication networks, optical signal monitoring has become an important issue. A variety of strategies can be followed in order to extract useful signal quality information. This information should ideally quantify the actual signal health, but in addition provide information concerning the main cause of degradation.
It is first discussed that the use of synchronous as well as asynchronous signal histograms can be very interesting. Asynchronous histograms proved their ability to detect and identify signal degradations due to noise, crosstalk, chromatic dispersion and non-linearities. The average Q-factor, a logical extension of the well-known (synchronous) Q-factor to asynchronous histograms was demonstrated as being a very powerful tool. Therefore it was the accuracy of the extracted Q_{avg} that was used as an indication of the quality of the proposed monitoring method.

Current histogram construction methods always use some kind of sampling system, thereby resulting in expensive and complex monitoring configurations. In this work we have presented a low cost method for the construction of an asynchronous signal histogram that did not require any sampling system or high frequency electronics.
The method consists of the construction of a linear system of equations, where the different probabilities of the signal histogram are the unknowns. The different equations are obtained as depicted in Fig. 2. The average output power of a fast non-linear component is measured for different versions of the data signal under investigation. The different

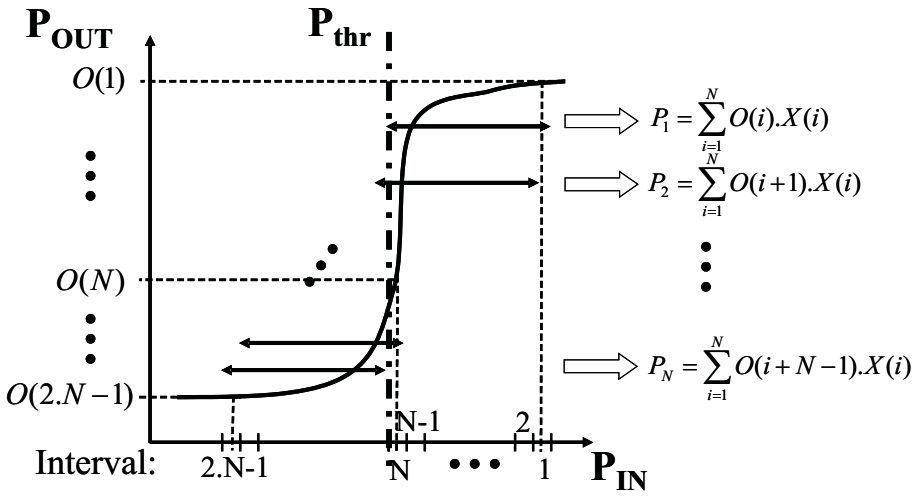

Figure 2: The principle of the proposed method is schematically displayed. The double arrow next to each equation depicts the power span in which the signal is located during the measurement of the corresponding average output power.

versions consist of the same signal to which an increasing attenuation is applied. It is obvious that once more average powers than the number of power intervals are available, the linear system can be solved. Note that only an **average** output power measurement is needed.

Since the resulting linear system is highly ill-conditioned, simple inversion leads to extremely inaccurate solutions. Therefore different approaches were studied to enhance the robustness. Regularization methods, based on the introduction of some constraint on the (semi-) norm of the solution can enhance the accuracy significantly. It turned out that the *"truncated singular value decomposition"* using the *"generalized cross-validation"* technique to choose the regularization parameter was the best option for our specific problem. To obtain even better results, two fitting approaches were developed. They included a priori information concerning the shape of the histograms. The increased extraction accuracy was unfortunately accompanied by a decrease of the transparency.

In order to find a decent non-linear component, it was demonstrated that the condition number of the system matrix can be used as a first indication of the suitability. It could be concluded that theoretically the best static power transfer should show a very steep transition in combination with a large relative power jump. Of course, practical issues

such as speed, stability, reproducibility, etc. should also be taken into account. It turned out that the steep laser power characteristic obtained as output of a SOA/DFB laser combination was the best option available at our laboratory.

An extensive theoretical study revealed that accurate Q_{avg} extraction should be possible, if the dynamic power transfer followed the assumed (static) transfer very accurately. In addition the measurement noise should be kept sufficiently low. It became clear however rather quickly that a very accurate extraction will be very difficult to achieve. This is a common problem for all the histogram based methods.

A low bit rate proof-of-principle experimental setup was build using a commercial SOA/DFB combination device. Monitoring experiments revealed that trends in the signal quality could certainly be monitored. I.e. a sudden decrease of the signal quality could be detected. This can be already interesting, since the place at which this sudden drop of signal health occurs can help in identifying the possible origin. An accurate parameter extraction was however not achieved. This was mainly due to the deviation from the static power transfer once a dynamic signal was applied.
The study presented does however indicate that if an ultra-fast nonlinear component based on the Kerr-effect could be used, much more accurate results will be achieved.

Small-signal optical modulation characteristics of two types of gain-clamped SOAs

In the study of several regenerator configurations, we used different types of gain-clamped SOAs. Therefore, the dynamical performance of two types under small-signal optical modulation was studied in depth, theoretically as well as via experiments. The gain-clamped SOAs consist of classical traveling wave SOAs in which a laser cavity is incorporated. In the case of the GCSOA this is a longitudinal cavity, whereas in the LOA a vertical cavity is used. In order to enable the theoretical study of the LOA, a one dimensional rate equation model was developed. To model the GCSOA, a simulation tool was already available.

The amplification of a RF signal component was studied, co- or counter-propagating with a CW optical signal. In the co-propagating case, a clear resonance in the modulation of the laser power and the carrier density was observed, resulting in a dip in the RF gain in the

vicinity of the resonance frequency. This resonance frequency shifted to lower frequencies for higher injected powers. In the case of the GCSOA this dip was clearly more pronounced due to the "weak" local clamping mechanism of the signal gain. In the LOA on the other hand the "stronger" local clamping could absorb the input power variations more efficiently. In the counter-propagation setup, in both amplifier types a much more frequency independent gain was obtained. This was caused by the smaller amplitude of the RF signal in the part being most vulnerable to perturbations (i.e. the back part).

In the two injection schemes mentioned, the crosstalk on a weak probe injected at both facets was investigated. A clear resonance was now observed for both types of amplifiers. A gradual transition to the low pass characteristic of a classical SOA took place when increasing the CW input power. In the GCSOA this transition happened in all investigated cases much more instantly, compared to a gradual transition in the LOA. For the probe propagating in the opposite direction of the RF signal, a walk-off effect was observed for the higher frequencies.

In the RF gain characteristics the different clamping mechanisms were clearly rendering a different behavior, whereas in the crosstalk this was less pronounced. All the conclusions were confirmed by experiments.

All-optical reshaping based on a simple MZI

A new interferometer configuration was proposed consisting of one active arm containing a SOA and a variable attenuator, while the other arm was left transparent. The advantage compared to the all-active interferometer stems from the possibility to use the SOA in deep saturation, resulting in enhanced dynamic properties. If combined with a linear amplifier, the configuration can perform 2R regeneration.

A time domain SOA model including non-linear gain suppression was developed to enable a theoretical dynamical study. It was demonstrated that all-optical reshaping, consisting mainly of extinction ratio improvement combined with some noise suppression could be achieved up to bit rates of 40 Gb/s if a high speed SOA was used.

A fibre based interferometer using a prototype SOA was build to perform eye diagram measurements. Clear extinction ratio improvement could be achieved for 10 Gb/s NRZ signals combined with a small amount of noise suppression. BER measurements could not be

performed due to the unstable nature of the interferometer. An integrated version of the configuration is currently under production.

English Text

Chapter 1

Introduction

Before starting the technical part of the PhD, the work will be generally situated in the present telecommunication network evolutions. A brief overview of what can be found in the manuscript will also be given.

1.1 Optical telecommunication networks

A press release from Computer Industry Almanac Inc. in September 2004 stated [1]:

> The worldwide number of Internet users will reach nearly 935 million in 2004 and will top 1 billion in mid 2005. The U.S. continues to lead with over 185M Internet users forecasted for year-end 2004. There is little Internet user growth in the developed countries, but in the next five years many Internet users will be supplementing PC Internet usage with Smartphone and mobile device Internet usage. Internet usage is growing strongly in China, which surpassed Japan for second place in 2003. The growth of Internet users will continue in the developing countries for another decade.

Reading this, together with noticing the ever-increasing bandwidth demands of the delivered services and applications makes it easy to understand that a huge explosion of the capacity of the telecommunication networks took and still takes place, while ever more reliability is required. This fast increase in bandwidth demand is mainly fulfilled by incrementally implementing parts of the networks optically, since the potential of the optical fibre as transmission medium is significantly

higher than that of copper, which is used for the transmission of electrical signals. Wavelength Division Multiplexing (WDM) and Dense WDM (DWDM) are technologies widely used in the backbone of today's high capacity telecommunications networks. In those systems it is mainly the transmission that is performed in an optical way (using multiple wavelengths per optical fibre, each wavelength corresponding to a different channel), whereas the control and monitoring is still done by an overlaying layer (e.g. SDH/SONET). Bit Error Rates (BER's) and Q-factors are calculated at line termination points from information included in the digital frame structure, or simple LOS (Loss of Signal) alarms originating from power monitoring taps are produced [2]. The functionalities using digital information encoded onto the signal are inherently bit rate and coding format dependent, which decreases the overall transparency of the communication network. Moreover, due to the large variety of bit rates present in packet-based data streams, the encapsulation in fixed transport modules (e.g. SDH modules) sometimes leads to an inefficient use of the available bandwidth.
All this explains why there is a lot of research going on, investigating possible configurations that can lead to an all-optical transparent platform technology where IP-based traffic can be directly transported over this optical layer (e.g. IST-STOLAS project [3]). An important note to be made is that the elimination of e.g. the SDH layer, whether it is complete or partial (it can still act as a client to the underlying optical layer), comes together with the elimination of its incorporated functionalities such as routing, monitoring, error detection, etc. It is clear that the construction of new all-optical network architectures also consists of the development of new all-optical equivalents of those lost functionalities. A schematic of an optical network serving as transport layer for a diverse range of clients is depicted in Fig. 1.1. Note the flexible optical path configuration, achieved by the use of a.o. optical add-drop multiplexers (OADM's) and optical cross-connects (OXC's) [4].

1.2 Optical Performance Monitoring

Why Optical Performance Monitoring?

The previous paragraph described the evolution to more complex optically switched, meshed data transmission networks with large channel counts, which are vulnerable to network malfunctions, misconfigurations and traffic affecting signal impairments. Moreover, also the

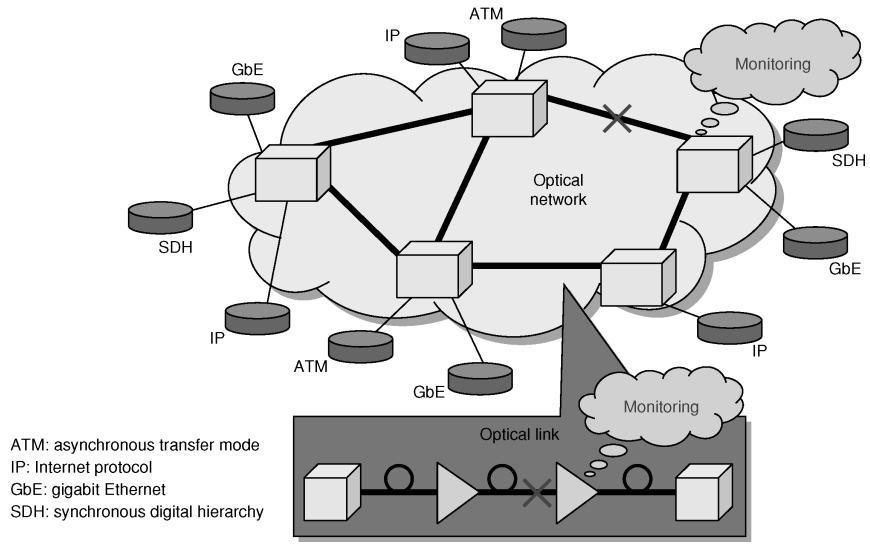

Figure 1.1: Schematic of an optical network with diverse clients. [4] ©NTT

increase of per channel data rates poses significantly more stringent requirements on the tolerable transmission margins and engineering rules [5]. All this leads to a high demand for decent fault management. Optical Performance Monitoring (OPM) will therefore be very important to supervise the network and make fault localizations possible in order to perform the necessary reconfigurations [6]. A possible definition of OPM can be: *"Physical layer monitoring of the signal quality, i.e. for the purpose of determining the health of the signal in the optical domain "* [7]. Guaranteeing SLA's (Service Level Agreements) between the network operators and their clients is one of the primary applications of OPM, but also routing can be based on information gathered from OPM. This was a.o. demonstrated in [8], where a path performance prediction function using OPM was used to choose the best path to transport the high priority traffic. In general, distributing relevant OPM information to the correct instances within the network can be helpful to keep the network management scalable. Therefore it is very important to gather the quality information in such a way that it also contains information that can help to localize and identify bad functioning network elements. Moreover it would be interesting if this monitoring signal could be directly used for active compensation techniques, such as active gain ripple compensation or Polarization Mode Dispersion (PMD)

compensation.
OPM can be implemented in either a shared or dedicated, a disruptive or non-disruptive way in a system. Ultimately one could even have an in-line device performing its own functionality, e.g. an optical 2R regenerator [9], from which a monitoring signal can be deduced.

Degradation mechanisms

Before briefly introducing the different OPM strategies it is important to mention the different optical degradation mechanisms present in an optical network. Roughly speaking they can be divided into two groups: noise and distortion. Distortion is classified as an unwanted *deterministic* change of the signal whereas noise results in an unwanted *stochastic* contribution to the signal [10]. Within these categories there are innumerable root causes, which are however not always easily classified in a specific category, a 'gray' zone exists in between. On one hand we have the transmission impairments, caused by the propagation of the optical signal through the network consisting of fibre, amplifiers, OXC's,... In addition we also have the components faults, caused by malfunctioning or improperly installed or configured network elements. The impairments the latter cause, are extremely diverse and cannot be comprehensively classified. Recently the ITU-T, a standardization organization in the field of telecommunication, defined attenuation, frequency drift, PMD, four-wave mixing, Amplified Spontaneous Emission, chromatic dispersion (CD), reflections, laser noise and crosstalk as the most common causes of signal degradations occurring in DWDM networks [11].

OPM Techniques

Contrary to electronic monitoring, a standard set of OPM parameters has not been identified up till now. This is also an extremely difficult task since it consists of the monitoring of a physical layer and thereby the weaknesses depend strongly on the implemented network architecture. Moreover in the case of the electronic monitoring all the monitoring can be easily integrated on one chip, whereas for the OPM different parameters will often require different equipment. Frequently suggested OPM parameters are given in Table 1.1 [7].

Digital monitoring techniques, such as BER extraction from forward error correction (FEC) information [12], have the best correlation with

OCM/WDM layer param.	Advanced/Signal quality param.
Aggregate power	In-band OSNR
Channel power	Q factor/BER/ESNR
Channel wavelength	PMD (Differential Group Delay)
Spectral OSNR	Accumulated chromatic dispersion
	Bit rate
	Jitter

Table 1.1: Frequently suggested OPM parameters

the signals BER but do not give any information concerning the origin of the fault. Analog properties of the optical signal on the other hand are much better correlated to the source of degradation. A huge set of analog measurement techniques have been developed, making it impossible to give a complete overview. We will however try to summarize the most important trends and give some references. A more extensive overview can be found in a.o. [7] and [13]. The classification used in [7] will be followed.
In general we can divide the OPM methods in time- and spectrum-based methods. The latter can be the optical as well as the amplitude power (RF) spectrum . The RF spectra in general contain information better correlated with the data signal quality. Such RF methods can also consist of the spectral post-analysis of RF tones superposed on the transmitted data signal, since they can provide information about a.o. chromatic dispersion (CD) (e.g. [14]) and PMD (e.g. [15]).

OSNR Measuring the Optical Signal to Noise Ratio (OSNR) by taking the ”noise” level adjacent to the signal peak in the optical spectrum is easy, but has proven to not always be that correct. Problems with this technique can e.g. arise in the case of densely packed optical channels where it is very difficult to distinguish between the effective noise level and the spectral edge of the adjacent channel [16]. This is illustrated in Fig. 1.2. In addition this consists of a DC measurement, and therefore no distortion effects are included. This can lead to a very weak correlation between the OSNR and the BER in some cases. Even in systems where noise is the only degradation mechanism problems can occur in certain setups (e.g. if an AWG DEMUX is used with a periodic transfer function which leads to ASE contributions from outside the WDM band) [17]. For optical amplifier performance monitoring in certain configurations it could on the other hand experimentally be

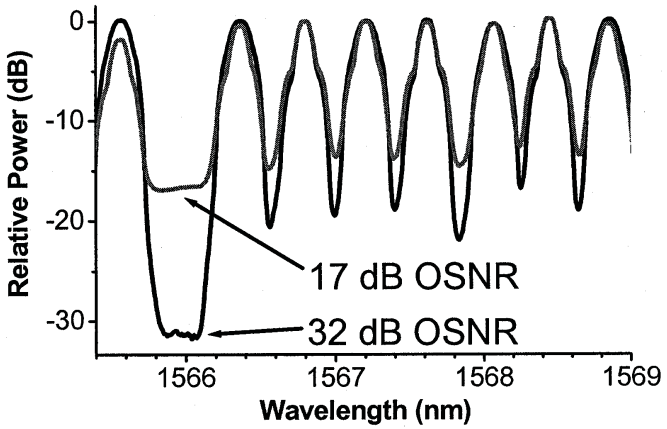

Figure 1.2: Illustration of the optical spectrum corresponding to a set of 10Gb/s DWDM signals. One signal is turned off in order to demonstrate that a significant error is made by taking the OSNR as being the value between subsequent peaks in the spectrum. We observe only a small difference in this minimum value, whereas the effective difference in OSNR is 15 dB [16]. ©IEEE

demonstrated that the system OSNR can be well correlated with the actual BER [18]. This illustrates that care should always be taken in interpreting the "systems" OSNR. A lot of measurement techniques not requiring an optical spectrum analyzer have been developed so far, all differing in the way the necessary discrimination between noise and signal is done. E.g. based on the polarizations [19] or on RF monitoring of places within the amplitude power spectrum where no signal is present.

Dispersion Dispersion monitoring gained a lot in importance due to the transition to dynamically configured optical networks, in which every signal arriving at a certain point in the network can possess a different amount of dispersion-induced distortion due to the different paths they traveled. This will make the formerly used static compensation methods unviable, and replacement by dynamic methods using real-time dispersion monitoring becomes necessary. One of the first CD monitoring techniques was the detection of a phase modulated signal into an amplitude modulated signal [20]. Adding SCM RF tones to the data signal also showed to be very interesting. A lot of different strategies depending on the type and number of RF tones added were

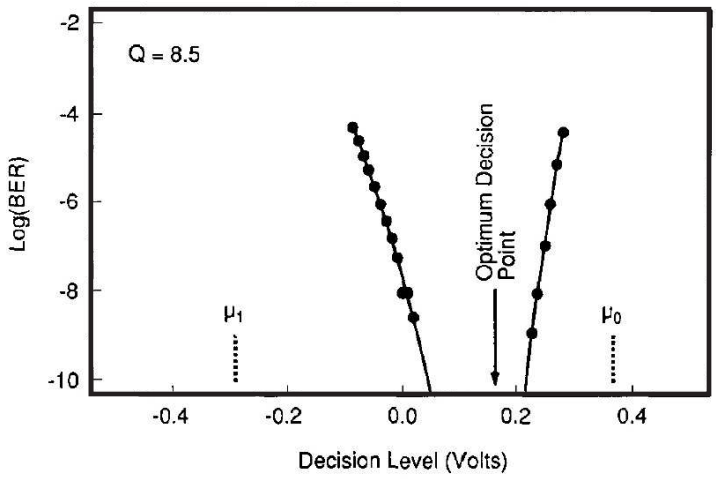

Figure 1.3: An illustration of the method used to calculate low BER's out of measurements of the BER in function of the decision threshold. The dots show the measured BER's, the line represents the fitted curve. A Q of 8.5, corresponding with a BER of 10^{-18} was found [28]. ©IEEE

developed (e.g. [2], [14], [21]). As will be discussed in depth in chapter 2 also signal histogram construction can help in analyzing the signal degradation caused by CD [22], [23].
The other source of dispersion induced distortion, called PMD is a very complex mechanism and is, with the increase of channel rates, identified as one of the most important degradations to be overcome in the future optical networks. To optimally perform active PMD compensation it is important to find a monitoring signal, strongly correlated to the performance of the system. Possibilities are the degree of polarization (DOP), the Stokes parameters and the mean square error (MSE) [24] [25] [26]. Again also the measurement of the RF spectrum at given frequencies can be very interesting [27].

Q-factor/BER Direct BER measurements are very time consuming when realistic BER-values have to be measured (e.g. for a 10 Gb/s signal a BER of 10^{-13} corresponds to approximately one error occurring every 15 minutes). Moreover they have to be performed off-line, which is not desirable from an operator point of view. Bergano et al. [28] developed a widely used technique to measure the BER (Q-factor) of realistic signals in a reasonable time. The principle they apply is to measure the BER for different values of the decision threshold

where more errors are made, thereby making the measurement much more reliable. Afterwards a fitting leads to the actual BER and corresponding Q-factor (Fig. 1.3 depicts an illustration as was given in [28]). This technique is also called the single decision threshold technique, which must however still be done off-line. A solution to this is the dual decision threshold technique introduced in [29]. Now the known Pseudo Random Bit Sequence (PRBS) used in the previous approach is replaced by the decisions resulting from the most optimal threshold choice. This makes in-service testing possible.
Alternatives to those BER measurements are the histogram based methods. Several techniques have been developed for extraction of the Q-factor of a signal, based on either synchronous or asynchronous signal histogram construction e.g. [30] and [31] respectively. Since the main part of this PhD is devoted to the development of a simple method for the construction of an asynchronous histogram, we will not go any deeper into the difficult and sometimes confusing interpretation of histogram data. This will be thoroughly explained in chapter 2. For completeness it is worthwhile mentioning that histograms can provide information concerning non-linearities, CD, noise, crosstalk and rise time.

Jitter Timing impairments are difficult to measure and are usually left to regenerators to deal with. A synchronous eye diagram, which is the superposition of all the bits in a bit stream onto one bit period, can be used to monitor the jitter, as was demonstrated in [32].

1.3 Regeneration issues

Due to the various degradation mechanisms present in fiber optic networks mentioned in the previous section, it is necessary to clean up data signals on a regular base. Ideally one should reamplify, retime and reshape the signal (3R-regeneration), but experiments [33] have shown that the achievable propagation distance can be significantly increased even if only 2R regeneration is performed.

To date, a lot of different components have been employed to serve as a basis for all-optical decision or reshaping elements. Saturable absorbers and electro-absorption modulators can perform a suppression of the zero level of the data signal, while being transparent for the one level. The resulting extinction ratio (ER) improvements were experimentally demonstrated at bit rates of 40 Gb/s [33, 34]. In a Non-linear Optical Loop Mirror (NOLM) on the other hand, the very weak but ul-

trafast Kerr-effect in an optical fibre is utilized in an interferometer configuration to give very good reshaping. This regenerator moreover has the potential of working at bit rates above 100 Gb/s, but very long fibre spans are needed to achieve the necessary non-linear phase shift [35]. Most of the all-optical regenerators are therefore based on the non-linear change of the complex refractive index in Semiconductor Optical Amplifiers (SOAs). When placed in an interferometer, the input power dependence of the phase shift can be translated into an input power dependent interference. 2R regeneration in combination with wavelength conversion was demonstrated at 10 Gb/s [36]. 10 Gb/s experiments were presented also for the so-called pass-through scheme, i.e. when used without wavelength conversion [37]. To improve the speed of optical interferometers, several schemes have been developed so far, mostly based on differential schemes. A drawback of these schemes is that they all suffer from a bit rate dependency. 2R and 3R regeneration with simultaneous wavelength conversion has been demonstrated in this way at bit rates of 40 Gb/s [38]. Another 3R regeneration schemes based on the non-linear effects in SOAs is the Ultrafast Non-linear Interferometers (UNIs), demonstrated at 84 Gb/s [39].

In this work we will propose a new reshaping element based on a Mach-Zehnder interferometer (MZI) in a pass-through scheme. The pass-through scheme has the advantage of not requiring a pump laser or an optical filter. In combination with a linear optical pre- or post-amplifier, all-optical 2R regeneration can be achieved. This will be discussed in chapter 6.

1.4 Overview PhD

Below we present a short overview of the topics discussed in this thesis.

As was discussed in the introduction, optical data signals can be degraded in several ways. It was already mentioned that a signal histogram can be used to extract information concerning the signal quality. In the next chapter, we will discuss the different strategies that can be used to obtain as much information as possible out of a signal histogram. Also the construction methods used up till now will be briefly introduced, together with a short description of the method investigated in this work.

In chapter 3 the monitoring method will be explained in detail, together with the developed simulation platform. Different strategies were followed to extract the actual histogram out of the measurement

data. They will be introduced and pro's and contra's will be discussed. A description of the methodology used to build a decent practical monitoring configuration in accordance to the proposed method will be given. Limitations and requirements are extensively studied.

Chapter 4 reports on the dynamical experiments performed with low bit rate optical data signals.

Since in this work we made use of different types of semiconductor optical amplifiers, chapter 5 reports on a study of the behavior of two types of gain-clamped semiconductor optical amplifiers under small-signal optical modulation. Experiments as well as simulation results will be discussed.

Also an all-optical reshaping element was investigated theoretically and experimentally. The results of this research are summarized in chapter 6.

Finally a global conclusion will be formulated, together with some perspectives with respect to possible continuations of this work.

1.5 Publications

The results obtained within this work have been published in a journal paper and were presented at various conferences. This paragraph gives an overview of the publications.

- S. Verspurten, G. Morthier, R. Baets, "Experimental and Numerical Small-Signal Analysis of Two Types of Gain-Clamped Semiconductor Optical Amplifiers,"*IEEE Journal of Quantum Electronics*, 42(3), p.302-312 (2006)
- S. Verspurten, G. Morthier, R. Baets, "Derivation of the amplitude histogram of an optical signal using an optical 2R regenerator,"*ECOC-IOOC*, 3, Italy, p.678-679 (2003)
- S. Verspurten, J. De Merlier, G. Morthier, D. Van Thourhout, R. Baets, "All-optical 2R regeneration at 10 Gb/s in a MZI-configuration with one active arm,"*Proceedings of the OSA Topical Meetings (Optical Amplifiers and Their Applications Integrated Photonics Research)*, United States, p.JWB 13 (2004)
- S. Verspurten, J. De Merlier, G. Morthier, R. Baets, "Experimental demonstration of all-optical 2R regeneration at 10 Gb/s in a MZI-configuration with a single SOA,"*IEEE/LEOS BENELUX Chapter - 2003 Annual Symposium*, Netherlands, p.43-46 (2003)

- G. Morthier, W. D'Oosterlinck, S. Verspurten, "The non-linear behaviour of laser diodes integrated with semiconductor optical amplifiers,"*ICTON 2005 (invited)*, 2, Spain, p.102-107 (2005)
- W. D'Oosterlinck, S. Verspurten, G. Morthier, R. Baets, M. Smit, "Experimental Demonstration at 10Gbit/s of a 2R-Regenerator Based on the Mutual Optical Feedback,"*IPRA 2005*, United States, p.IMC 2 (2005)
- G. Morthier, S. Verspurten, W. D'Oosterlinck, "Interferometric photonic circuits for optical signal processing,"*The 88th OSA Annual Meeting, Frontiers in Optics 2004, Laser Science XX, Collocated with Diffractive Optics and Micro-Optics and Optical Fabrication and Testing Topical Meetings (FiO/LS and DOMO/OF&T 2004)*, United States, p.FThU3 (2004)

Chapter 2

Monitoring strategies: state of the art & motivation of choice

As was mentioned in the introduction, the main part of this PhD thesis consists of the development of a new, simple method for the construction of an asynchronous signal histogram. The goal is to perform this without the use of any kind of sampling systems, as is the case in current systems. In section 2.1 we will explain what the different types of histograms are, followed by a thorough explanation of the different strategies used to analyze the resulting signal histograms (section 2.2). As will be seen, a lot of signal performance indicators can be extracted, however care should be taken with the interpretation.
Finally, currently used construction methods will be briefly explained and the main idea behind the method we propose will be introduced and motivated (sections 2.3 and 2.4 resp.).

2.1 Definition of a signal histogram

A signal histogram is the probability density distribution of the optical power of a data signal. This distribution can be constructed out of a sampled bit stream. This sampling can be performed either synchronously or asynchronously.
In the case of asynchronous sampling, the sampling rate is not correlated with the data signal bit rate. The moment within a bit at which the signal level is recorded is thereby continuously changing with respect

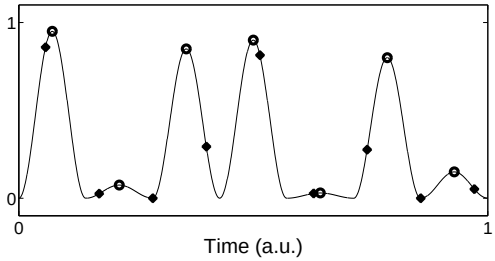

Figure 2.1: Illustration of a bit stream with marks representing the sampling times of a synchronous (circles) and an asynchronous (squares) sampling system.

to the decision time, as illustrated by the squares in Fig. 2.1. This has the big advantage that no clock recovery is required, making the method completely transparent to bit rate and coding format. The drawback is that a lot of extraneous and unwanted information is included (e.g. the flanks of the bits), which will never be taken into account during the final decision process. This degrades the accuracy of the extracted results.
Synchronous sampling on the other hand, measures the power levels only at moments within a bit equal to the ideal decision time, i.e. at the moment within a bit where the eye opening is maximal (circles in Fig. 2.1). This will result in histograms containing information more closely related to the effective decision process in the receiver, but requires the difficult and expensive clock recovery task. Moreover, this definitely undermines the bit rate transparency of the method. Fig. 2.2 depicts a synchronous eye diagram, combined with the synchronous as well as the asynchronous signal histogram. Note the plateau between the peaks corresponding to marks an spaces in the asynchronous histogram.
It is easy to understand there exists a trade-off between both strategies concerning complexity and cost on one hand and quality of the extracted information on the other hand. The following paragraph will prove that even out of the asynchronous histogram very useful information concerning the signal health can be deduced. Moreover this information can definitely be applied in the monitoring of trends of signal quality including the identification of the origin of degradations, which was one of the requirements for a decent OPM method.

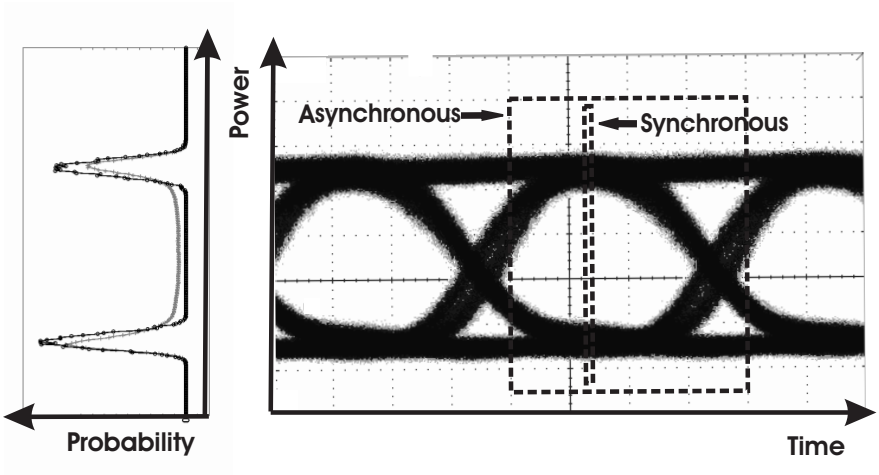

Figure 2.2: On the right a synchronous eye diagram of a NRZ PRBS signal is shown. On the left, the histograms corresponding to the 2 boxes drawn on the right are depicted. The 2 boxes enclose the samples taken into account for the construction of respectively the asynchronous (gray) and the synchronous (black) histogram.

2.2 Which information can be extracted and how?

In [23] system experiments were carried out in order to verify the sensitivity of an asynchronously obtained signal histogram to some of the most important signal perturbations. It was illustrated that by carefully observing the change of the shape of the histogram, an idea could be obtained with respect to the source of degradation.

- Amplifier noise added to the signal manifested itself as a decrease of the amplitudes and the relative distance between the peaks corresponding with the marks resp. the spaces.

- An increasing portion of intra-band crosstalk (generated by the addition of the signal with a delayed copy of itself) resulted in an emerging plateau surrounding the peak representing the transmitted ones.

- An increased amount of pulse distortion due to fiber dispersion acted mainly on the peak amplitudes of the histogram, combined with a little decrease of the distance between both peaks.

This qualitatively shows that studying an asynchronous histogram can indeed be interesting. However, some kind of quantification must be provided in order to become a potential candidate for OPM applications, thereby enabling the monitoring and adjustment of certain quality parameters in the network. The most important analysis methods will now be introduced. Where relevant the difference in applicability to asynchronous and synchronous histograms will be mentioned.

2.2.1 Averaged Q-factor method

The most "easy" way to extract info out of a **synchronous** histogram is to assume that the waveform distortions are sufficiently small and the signal is only perturbed by ASE noise which is assumed to have a Gaussian distribution. The fitting of the peaks of the histogram to such distributions results in standard deviations and means for the marks and the spaces rail, represented by σ_1, σ_0 and μ_1, μ_0 respectively. Under the given assumptions, the Q-factor and BER are given by [30]:

$$Q = \frac{|\mu_1 - \mu_0|}{\sigma_1 + \sigma_0} \tag{2.1}$$

$$BER = \frac{1}{2} erfc\left(\frac{Q}{\sqrt{2}}\right) \tag{2.2}$$

where erfc(x) is the complementary error function. This is a commonly used definition of the Q-factor. Although the actual probability distribution is not exactly Gaussian, a Gaussian approximation can often lead to close BER estimates [40] in an optical amplifier system.

As mentioned above, in an **asynchronous** histogram, also the edges of the bits are included. This leads to a histogram containing some information that is not directly related to the decision process. However it has been shown that applying a similar Q-based technique can also result in relevant information concerning the signal quality. This technique is widely used and commonly known as the **averaged Q-factor method**. It was almost simultaneously introduced by Shake et al. in [41] and by Mueller et al. in [42]. The technique consists of the fitting of two Gaussian probability distributions to an altered form of the asynchronously obtained histogram. Afterwards the Q_{avg} calculated as in Eq. 2.1 is linked to the actual synchronous Q, rendering an estimate of the systems BER.

The implementation of the averaged Q-factor method is in great detail explained in [43]. The paper also theoretically demonstrates the

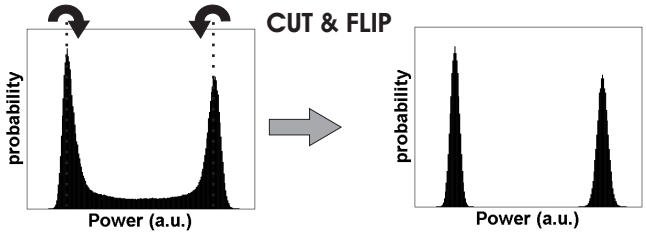

(a)

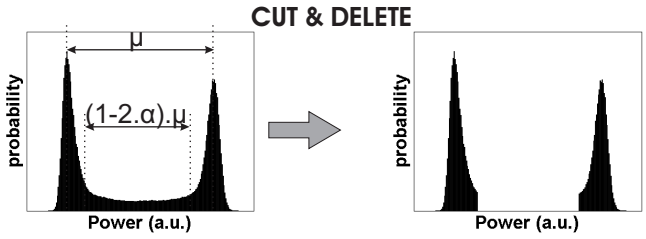

(b)

Figure 2.3: Illustration of cut-and-flip (a) and cut-and-delete (b) techniques. They can be applied to an asynchronous histogram to enhance the quality extraction, by partially replacing or removing the cross-point data.

potential of the method for the transparent monitoring of OSNR degradation. It is proven that, in a dispersion compensated system only being perturbed by noise there exists an almost linear relation between Q_{avg} and Q once the relevant parameters of the method are properly chosen.

In order to remove some of the unwanted information, several manipulations can be performed on the asynchronous histogram data before starting the actual calculations. They rely on the fact that most of the unwanted information is situated in between the peaks of the histogram, whereas the outer parts of the tails contain more "correct" information (this can also be seen in Fig. 2.2 where the outer flanks of the peaks of both histograms almost coincide). This can be easily understood by noting that most of the powers present in the flanks of the bits will be situated somewhere between the mean powers of marks and spaces. The techniques carry the self-explanatory names, cut-and-delete [41] and cut-and-flip [44], and are illustrated in Fig. 2.3. They can be utilized to improve almost every technique related to asynchronous histograms except if explicitly relying on the cross-point data. An important note to make is that the parameter α used to determine

what part of the histogram has to be discarded in the cut-and-delete approach has to be chosen with great care. This can e.g. be done by maximizing the correlation between Q_{avg} and Q. A value of $\alpha = 0.3$ seems to be ideal for the cut-and-delete case in the Q-average method presented in [43] (all samples between $\mu_0 + \alpha |\mu_1 - \mu_0|$ and $\mu_1 - \alpha |\mu_1 - \mu_0|$ are discarded). Since there is always a part of the cross-point data remaining in the asynchronous histogram, Q_{avg} will be limited once Q exceeds a certain limit.

In [45] experimentally obtained asynchronous Q-factors showed to reflect BER degradation due to noise and waveform distortion due to chromatic dispersion and non-linear effects. [46] on the other hand experimentally demonstrated the bit rate transparency in the case of 10 up to 100 Gb/s noise distorted RZ signals.

By deducing an extra parameter out of the fitting results (in addition to Q_{avg}), it was demonstrated that degradation due to noise and chromatic dispersion could be distinguished as being the main source of degradation [22]. This can improve the feasibility of the method for OPM purposes while remaining relatively simple, i.e. without complex mathematics being needed. The extra parameter relies on the different behavior of the distance between both peaks in the histogram in the presence of noise and dispersion. This means that if a decrease of Q_{avg} is detected, the examination of the changes in σ_1 and $|\mu_1 - \mu_0|$ can help to recognize the cause of the deterioration. Again also the bit rate transparency of the method was demonstrated, together with a strategy for implementing the method in a real network configuration. This is done by performing some kind of calibration procedure based on known signal degradations.

2.2.2 More complex approaches

Although it has been proven to be feasible in a lot of realistic optical network architectures, the averaged Q-factor method is still based on a relatively simple assumption of Gaussian distributions. This means that in cases where heavily distorted signals are present, poor results will be delivered. Also in the case of high quality signals, the Q will be underestimated. This is however not such a big problem concerning OPM-alarms etc. Nevertheless this lead to the development of several complex approaches for the analysis of the obtained histograms. The models aim for the incorporation of other effects such as crosstalk, ISI (Inter Symbol Interference), beat noise contributions, etc. in the mathe-

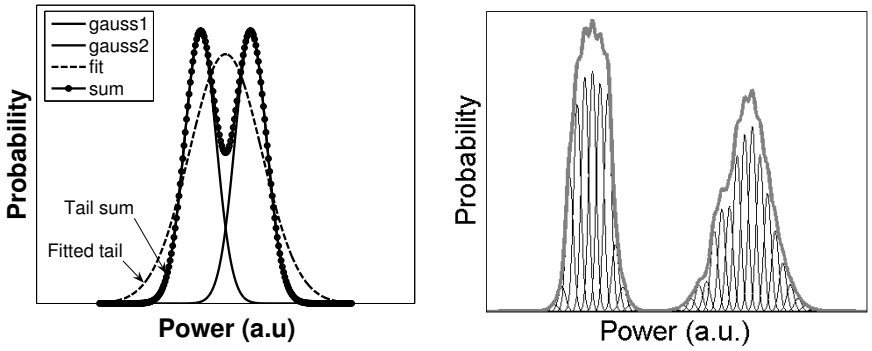

(a) (b)

Figure 2.4: In (a) two Gaussian distributions are depicted, together with the sum of both. The result of the fitting of one single Gaussian to this sum illustrates that σ will be overestimated. In (b) the sum of multiple Gaussian distributions is depicted (thick gray line), together with the individual distributions. This illustrates the method in which a histogram is interpreted as being the result of a sum of Gaussian distributions, where each histogram entry has its corresponding Gaussian distribution.

matical model. An overview will now be given of the most important models.

- If inter symbol interference (ISI) is present (e.g. caused by nonlinearities, dispersion, filtering,...), traditional Q-extraction based on one Gaussian distribution for mark and space levels respectively will lead to an overestimation of the standard deviations and consequently poor Q's [47]. This is illustrated in Fig. 2.4(a) where the sum of two Gaussian distributions with slightly different means is plotted, together with the result of the fitting of only one Gaussian to this data set. The individual Gaussian distributions originate from 2 different rails in e.g. the mark levels. It can be seen that the tail of the fitted curve extends further as compared to the real distribution (sum), rendering an overestimation of the BER. This was the motivation behind the development of some techniques aiming for the incorporation of distortion.
  In [44] an approach was presented that includes possible distortion effects observed in the histogram. Synchronous as well as asynchronous histograms can be used, the latter after the cut-and-delete technique is applied. The method interprets the different amplitude classes contained in the histogram as being the diffe-

rent sampled photocurrent values of a distorted signal. The statistical properties of the investigated signal are thus represented by a superposition of Gaussian processes (one at each point of the histogram), incorporating ASE-ASE and signal-ASE beating noise contributions. An example is depicted in Fig.2.4(b). The BER can now be calculated out of the summation of the integrations of the tails of the given distributions. The technique is experimentally demonstrated for signals degraded by dispersion and shows to give improved BER estimates as compared to the techniques using the single Gaussian model in the case where signal distortion is high. The same model, applied to an asynchronous histogram, showed to result in BER estimates within 5% of the actual BER in experiments exhibiting non-linearities in optical fibers [48]. The advantage of this technique is that no explicit assumptions are made concerning the origin of the distortion.
A similar technique was presented in [47] and [49]. The final probability distribution was assumed to be the result of the convolution of the distribution of the signal as such with the distribution of the noise on each of these signal components. Those signal components could e.g. be formed by the different bit patterns of three consecutive bits occurring in the data signal [47]. In this way, the actual Q has a contribution of the noise and of the ISI present in the signal. It was experimentally demonstrated that this ISI formulation can explain the word pattern dependence of the SNR [49]. It should be noted that this technique is used to interpret BER-measurements rather then as an analysis tool for histograms.

- Weinert et al. proposed a new synchronous histogram method for the identification of crosstalk [50]. The interferometric noise of a single dominant interferer leads to the typical U-shape of the mark distribution. In a real system this is however still combined with the Gaussian noise distribution. Considering this, it is possible to identify the effect of crosstalk and to evaluate the BER. This can be done by applying a deconvolution algorithm to the measured PDF of the marks with a Gaussian function with varying width. Only if the correct Gaussian is used, the interferometric noise structure of the pdf reappears. Thereby the amount of crosstalk can be calculated and the results can be used in a simple manner to obtain a good BER estimate. It should be stressed though that this is only demonstrated for synchronous histograms. How-

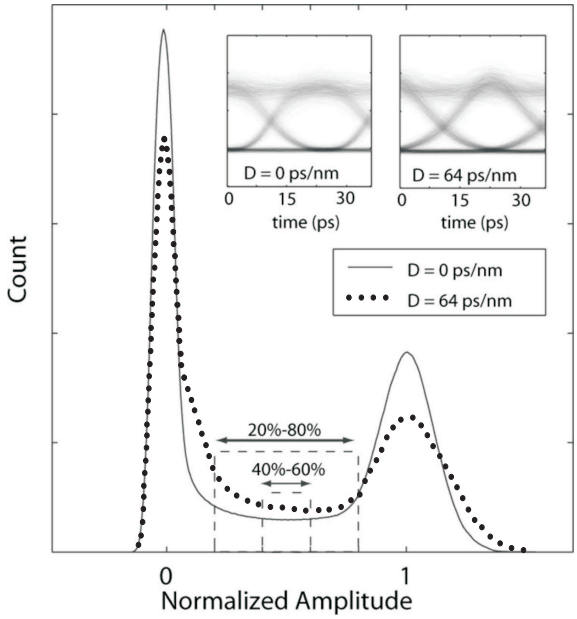

Figure 2.5: Two asynchronous histograms resulting from the simulation of a NRZ signal degraded by two different amounts of accumulated chromatic dispersion are drawn. Two different amplitude windows are shown. In the inset, the corresponding eye diagrams are depicted. ©IEEE [52]

ever, in [23] the appearance of similar plateau's could be observed in asynchronous histograms, so we believe a modified technique must be achievable for those histograms.

- Recently, a new method was presented in [51] for the monitoring of CD making use of the statistical moments of asynchronously sampled waveforms. The idea behind the method is the relation between odd statistical moments and the symmetry of the histograms on one hand and between even statistical moments and the sharpness of the histograms on the other hand. It is demonstrated experimentally as well as theoretically to be an interesting approach for CD monitoring, exhibiting a wider operating range as compared to methods requiring identification of marks and spaces (e.g. [22]).

2.2.3 Rise time calculations

The "unwanted"extra information included in an asynchronous histogram can also be converted into "interesting"information if estimates of rise and fall times of the bits present in the data streams are desired. This information can be helpful in identifying the source of degradation. Up till now two techniques have been proposed illustrating this.
The method proposed in [53] starts by inverting the amplitude versus time function of the basic pulse shape, incorporating a rise time parameter, without considering noise. This leads to a histogram function without noise addition, since this inversion represents the time the signal spends in each infinitesimal amplitude interval. Afterwards, this function is convolved with a Gaussian noise distribution. The resulting function is fitted to the measured histogram, and Q and rise time estimates can be extracted. It is demonstrated experimentally for 10 and 40 Gb/s NRZ signals that rather good estimates can be obtained.
A second method is based on the idea that most of the cross-point data present in an asynchronous histogram, originate from contributions of the flanks of the pulse shapes. Thereby the amount of cross-point samples relative to the total amount of samples should give us an estimate of the relative time it took a bit to rise and fall. In [52] it is demonstrated that choosing a 40-60 % amplitude window (relative to the mean of marks and spaces) is the best choice to define the cross-point data region, used for the counting. The general criterion to choose the amplitude window is to cover the part of the pulse edge that best represents the overall slope while keeping the window size adequately small to avoid an overestimation of the rise time due to noise effects. An illustration of the method is given in Fig. 2.5. The paper also experimentally reports on a PMD monitoring technique based on such rise time estimates, thereby confirming the potential of the method for OPM applications.

2.3 Current construction methods of optical signal histograms

The actual construction of the signal histograms discussed in the previous two sections, synchronous as well as asynchronous, is achieved by some kind of sampling procedure. Generally spoken there are three different configurations possible, summarized in Fig. 2.6.

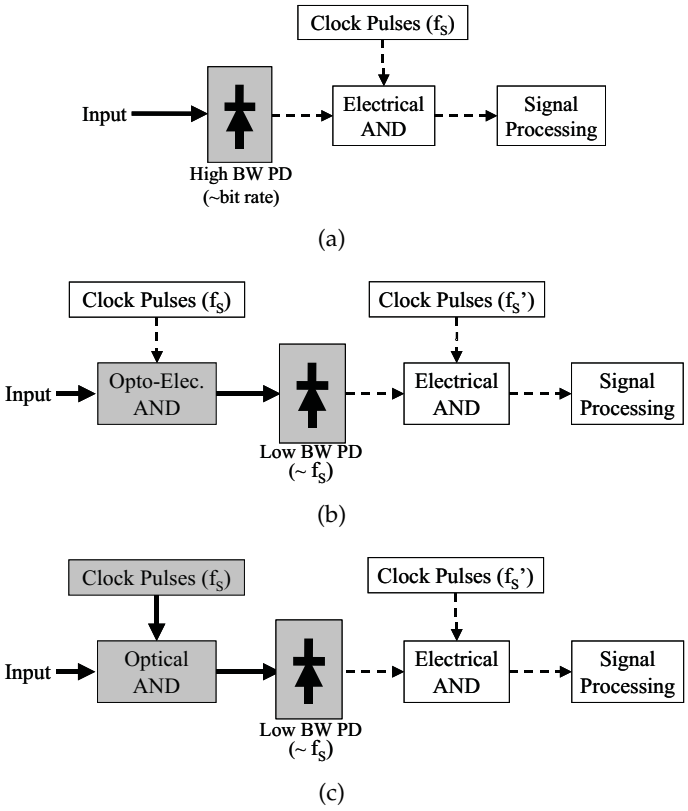

Figure 2.6: Different sampling approaches used to construct a signal histogram. f_s' is a clock frequency related to (but not always equal to) f_s. Optical components are depicted in gray. Optical signals are represented with thick arrows, whereas the dashed arrows represent electrical signals. PD: photodiode.

The most straightforward procedure (Fig. 2.6(a)) is to detect the optical signal with a high speed photodiode and sample the resulting electrical signal with a sampling frequency f_s (e.g. by a digital sampling oscilloscope). Important to note is that the bandwidth of the optical receiver and the electrical AND gate should be high enough (wider than that of the signal bit rate) in order to represent the optical waveform accurately.

In a second approach (Fig. 2.6(b)) the sampling is done electro-optically; this means that the signal is optically gated with electrical pulses. The resulting signal is detected by a photodiode of which the bandwidth can be much lower, since it is determined by the repeti-

tion rate (f_s) of the electrical pulses (e.g. a 1GHz pulse train for sampling a 40Gb/s data signal). In this case it is the width of the pulses that determines the maximum achievable bit rate. Finally the resulting electrical signal is sampled again electrically, now posing less stringent bandwidth demands on the electrical AND gate. In [54] an electroabsorption (EA) modulator was used as the sampling device. It was the only implementation found in literature where electro-optical sampling was used for histogram construction. The advantage over the sampling techniques discussed in next paragraph is that this device is small and relatively simple.

The last approach (Fig. 2.6(c)) is to perform the gating driven by an optical pulse train (with repetition rate f_s). This is called the all-optical sampling approach. Optical pulses can be achieved with subpicosecond resolution, extending the achievable bit rate to above 500 Gb/s. The pulse train can e.g. be generated by a mode-locked laser. As was the case in the previous approach, the sampling rate can be kept low (< 1 GHz) in order to avoid high-speed electronics [55]. A lot of research has been going on trying to reach a power efficient, accurate optical sampling gate, a complete overview will however not be given. Two effects are commonly used in order to achieve the non-linear optical AND gates. The first is the second-order non-linear effect $\chi^{(2)}$ in non-linear optical crystals (e.g. [41] and [56]). The optical sample is generated by SFG (sum frequency generation) or quasi-phase-matched mixing. The second effect consists of the third-order non-linearity $\chi^{(3)}$ in semiconductor optical amplifiers (SOAs) or optical fibers. Here the sample is formed by e.g. FWM (four wave mixing) [57] or due to interference based on XPM (cross-phase modulation) [58]. For a more complete overview of the all-optical sampling configurations we refer to e.g. [55].

The approaches described can all be used for both asynchronous and synchronous histogram construction. The difference consists of the correlation of sampling frequency f_s and signal bit rate. In the synchronous case f_s is deduced from the signal bit rate via a clock recovery circuit, while in the asynchronous case, both are independent. This has as a consequence that the former requires a pulse source with accurately adjustable repetition rate to compensate for drifts in the data clock frequency and make sampling of different data speeds possible. This requirement, in addition to the (difficult) synchronization process is the main reason for the significantly higher complexity and cost of the synchronous approach as compared to the asynchronous.

Asynchronous to synchronous conversion

Several techniques have been developed in order to achieve some kind of synchronization of the asynchronously obtained samples, since this can significantly improve the extracted information, while still avoiding the expensive and complex clock recovery circuitry.
In [55] and [59] similar techniques are presented, making use of advanced signal processing techniques to detect some kind of periodicity in the gathered samples by a Fourier-based analysis. They both prove it is possible to reconstruct a synchronous eye diagram out of an asynchronous sample set by accurately extracting the ratio of the sampling and data frequency. The drawback is of course the need for complex software calculations. We will not extensively describe the applied mathematics and refer to the cited literature.
A simpler, and very inventive approach was presented by Shake et al. [54] where a rough estimate of the signal bit rate was assumed to be known, e.g. from the data format (SDH/SONET, Ethernet, etc). If so, superposition of a limited set of the captured samples onto a time window roughly as wide as the bit period, can result in an opened eye diagram. This will not be an accurate reproduction of the actual eye diagram as was the case in the previous method, but however allows us to calculate a synchronous Q-factor that is better correlated to the actual BER as compared to the averaged Q-factor. This has been demonstrated by various experiments. The main advantage is the simplicity of the approach.

2.4 Proposed strategy for histogram construction

All the histogram construction methods developed up till now suffer from being rather complex and expensive. The direct electrical sampling requires very high bandwidth photodiodes, with a bandwidth being directly linked to the signals bit rate, thereby limiting the highest achievable data rates. The two other sampling approaches, electrooptical as well as all-optical, do relax the requirements of the photodiode, but use much more complicated configurations including extra pulse sources and sampling gates. The aim of this work was therefore the development of an asynchronous histogram construction method, combining the advantages of the different sampling approaches: a low cost, simple construction method that does not require any high frequency electronics or pulse sources.

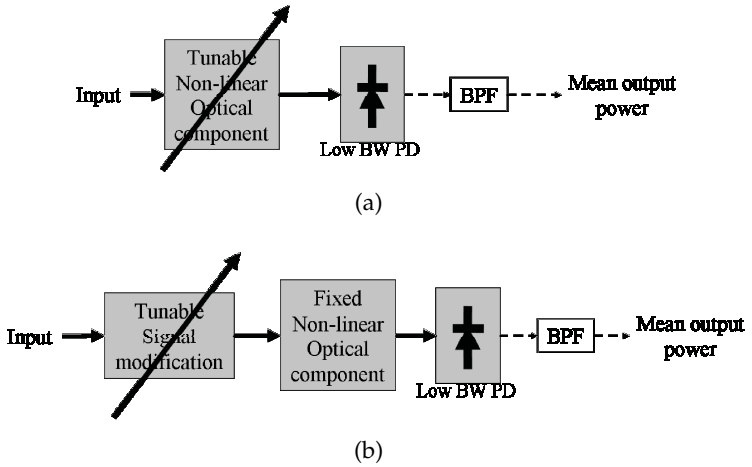

Figure 2.7: Schematic of one iteration of the proposed histogram construction methods. In (a) the non-linear characteristic is adjusted between the different iterations, in (b) it is the signal that is altered (e.g. attenuated).

In chapter 3 the methods actually investigated will be described in detail, but now we will give a general conceptual sketch of the rationale behind the proposed approach.

The methods rely on the fact that if we have an opto-electronic device, exhibiting a perfect step-like input-output relation, the average output power measured when a data signal is injected, is proportional to the relative time the signal has input powers located above the decision threshold. The link between this relative time and the probabilities present in a histogram is quite obvious. This means that a repetition of such measurements for different thresholds, or for altered forms of the optical signals, enables the construction of an asynchronous histogram. Both approaches are schematically depicted in Fig. 2.7.
The method depicted in Fig. 2.7(a) injects the data signal in a non-linear optical component with a bandwidth exceeding the signals bit rate. The resulting output signal can afterwards be detected by a low bandwidth photodiode, since only the average output power has to be extracted. If we can repeat this measurement for different non-linear input output relations of the component, it is intuitively clear that an asynchronous signal histogram can be calculated once sufficient measurements are performed. This can be understood by assuming a perfect step, with variable threshold. If we can sweep this threshold throughout the entire input power region, subsequently obtained averaged output powers

will line up as being the cumulative probability distribution of the signal. A simple derivation results in the asynchronous signal histogram. In the case of a non-ideal step the consecutive measurements will also enable histogram construction, be it with somewhat more complex calculations.
The second approach (Fig. 2.7(b)) uses a similar setup, with an extra building block added preceding the non-linear component, enabling the manipulation of the injected signal. Consecutive measurements will now consist of the averaged output powers resulting from altered forms of the data signal under investigation, while the non-linear component configuration is fixed. Altered forms can consist of e.g. different attenuations applied to the signal, different CW powers added to the signal, etc.. The analogy with the previous approach is clear, since now we shift "the signal over the threshold"whereas in the previous method we shifted the "threshold over the signal".
In both cases it will be the non-linear opto-electronic component which will be the most crucial element in the set-up, since this non-linear relation should be signal independent, thereby enabling transparent monitoring. The requirements for the electronics are however very reasonable since only the DC component has to be detected.

2.5 Conclusion

We have illustrated the great potential of an asynchronous signal histogram with respect to the extraction of useful quality information of an optical data signal. Various simulations as well as experiments have proven that degradations due to chromatic dispersion, amplifier noise, non-linearities and crosstalk can be detected and identified. The decrease of the accuracy of the information as compared to synchronously extracted quality measures is compensated by a significantly easier construction process.

We will propose a new method for the construction of an asynchronous signal histogram which uses no sampling systems or high frequency electronics. Only a fast non-linear optical component and some (relatively simple) processing circuitry are needed. The principle of the method was generally introduced, but will be studied in detail in the next chapter.

Chapter 3

Theoretical study of asynchronous histogram construction methods

As was described in the previous chapter, the goal of our work is to construct an asynchronous signal histogram without using any high frequency electronics, sampling systems, etc. The general idea behind the methods studied was explained in section 2.4. Now an overview of the different strategies we looked deeper into will be given, together with the motivation for the choice of the method used for further research. A theoretical study will be presented that leads to the requirements that need to be fulfilled in order to enable a practical implementation. The feasibility of several implementations will be investigated.

3.1 Methods

Assume we start from a known input-output power relation ($P_{OUT} = f(P_{IN})$) of a non-linear optical component. Once a certain power span (divided into N intervals) is chosen, we can express the average output power of the non-linear component as a weighted sum of the probabilities that the signal power is located within those intervals. The weights can be deduced from a discretized version of f. If we repeat this several times such that more than N equations in the N unknowns, being the probabilities, are obtained, it is theoretically possible to extract the probabilities uniquely if at least N equations are linear independent.

Roughly speaking we thought of two ways to obtain the different equations, i.e. by "moving" the characteristic or by "moving" the signal.

3.1.1 Variable characteristic

Here the idea is to change the relation $P_{OUT} = f(P_{IN})$ between every average power measurement. This is equivalent to the method used by Otheru et al. presented in [30] where an electronic decision circuit is used to compare a signal with a variable decision threshold at each bit. In that case, f is a perfect step function. If this threshold is shifted, the counted number of spaces during each step lines up as the cumulative probability distribution of the data signal. Simple derivation results in the synchronous signal histogram. Instead of performing the counting, it is intuitively clear that also the average output power of a non-linear optical gate showing a step-like input-output relation gives an indication of the time during which the signal power was smaller (or larger) than the threshold input power of the optical gate. Of course, in this case the entire signal is taken into account since no synchronization is performed. Therefore this results in the asynchronous probability distribution.

We can generalize this principle by assuming that we have N different configurations of a given non-linear optical component of which the input-output power relation is known. Applying each time the same signal makes it easy to build up N equations all having the same probabilities as unknowns. Solving the constructed linear system will result in the asynchronous probability distribution of the signal.

3.1.2 Variable signal

Assume we do not change anything to the non-linear gate between consecutive average power measurements, but instead apply each time a modified version of the original data signal. It is clear this can also result in N different linear equations. The only requirement is that each time the same probabilities are used in the equations. In other words, the same modification as applied to the signal should be applied to the interval edges. Two obvious choices of the modifications of the signal that ease the calculations are described in the following.

Additive scheme

If we choose the power intervals equally distributed on a linear scale, we can project adjoined intervals onto each other during subsequent measurements by adding an extra amount of CW optical power equal to the interval width. Doing this, we obtain a linear system with the unknowns being the probabilities associated with those intervals. The advantage is that this immediately provides us the real asynchronous histogram (i.e. on a linear scale) needed for further information extraction methods such as the Q-average method. A brief theoretical study of this method was presented in [60].

Multiplicative scheme

If on the other hand, we choose the power intervals equally distributed on a logarithmic scale, the projection of the adjoined intervals onto each other can be achieved by applying an extra amount of attenuation to the signal equal to the interval width on dB-scale. Again, repeating this will result in a linear system with the N unknowns now being related to logarithmically distributed intervals. A conversion to a linear scale, which is necessary for further processing, should be calculated in this case.

3.1.3 Discussion and motivation of the method choice

Despite the fact that all of the previous approaches can theoretically result in the construction of the asynchronous signal histogram, we opted to focus on one specific method. We believe the method using the **variable signal in the multiplicative scheme** shows several advantages for practical implementation as compared to the others.

First of all, the characterization of the method with variable signal is fairly simple, since only one input-output power relation has to be provided. In the case of the variable characteristic on the other hand at least as much input-output power relations as number of intervals have to be provided. Moreover they should be as frequency independent as possible in all the different working points of the non-linear component. The reproducibility of the different settings of the component will probably be worse than the reproducibility of a simple attenuation. This leads to a better definition of the system matrix. The scaling of the number of necessary characteristics with the number of intervals is also not very attractive concerning the transparency of the method with respect to

the handling of different signal types. In the case of the multiplicative scheme this only implies a change in the number of attenuations.

If we use the multiplicative scheme, the only extra component needed is an adjustable attenuator. In the case of the additive scheme a wavelength tunable laser source is needed of which the output power can be accurately adjusted (either by a tunable current source or an adjustable optical attenuator). The wavelength tunability is necessary to anticipate on possible wavelength dependencies of the non-linear component. Moreover we believe the reproducibility of the attenuation is much better as compared to the power additions. I.e. the reproducibility of the reaction of the component to the sum of the original data signal and a second CW signal is much lower than the reaction to an attenuated version of the original data signal.
The fact that a redistribution of the histogram data occurs when the histogram is converted to a linear scale slightly reduces the accuracy. Accurate results can however still be obtained if the increment of the attenuation is chosen sufficiently small. This is illustrated by calculating the average Q-factor as described in section 2.2.1 for a linearly scaled histogram with interval width equal to 0.1 mW which is derived from a histogram with logarithmically distributed interval edges with different widths. If we increase the original interval width, the table in Fig. 3.1 shows that in the studied case, it is only at a width of .25 dB that the Q_{avg} starts to be less accurate. This is however not a fixed limit for no matter which case, but it shows that still reasonable interval widths on dB-scale can be used. In Fig. 3.1 it can be seen that this loss of accuracy of Q stems from the loss of accuracy at higher powers. For clarity reasons only two histograms are depicted.

3.2 Detailed explanation of the proposed method

As explained in the previous section, we will focus on the **method using a variable signal in the multiplicative scheme**. A detailed explanation of the method, combined with the introduction of the symbols used during further discussions will now be given.

Assume that we have a non-linear gate with a perfect step-like power transfer. Subsequently we apply attenuated versions of the original data signal, with a constantly incremented attenuation. The corresponding average output powers will line up as the cumulative probability distribution with interval edges equally distributed on a logarithmic

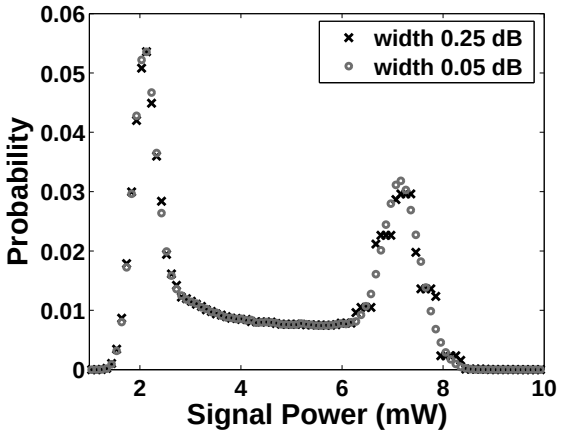

d (dB)	Q-avg
0.001	6.4570
0.01	6.4555
0.05	6.4280
0.1	6.3552
0.25	5.8881
0.5	4.7082

Figure 3.1: On the left two histograms, corresponding to the same data signal, with interval edges equally spaced on a linear scale (width=0.1 mW) are drawn. The histograms are obtained by conversion of a histogram with intervals equally spaced on logarithmic scale with two different widths (see legend). The table on the right contains the Q_{avg}-values obtained from linearly scaled histograms originating from logarithmic histograms with interval width d.

scale. Derivation and conversion to a linear scale will result in the asynchronous histogram.

If a practical optical gate is used, the situation changes somewhat. An explanation will be given using the input-output power relation and symbols as depicted in Fig. 3.2. It is worth mentioning that also an inverted decision characteristic can be used, i.e. high output for low input power and vice versa. In fact, theoretically spoken, any component showing any non-linearity in its input output power relation can be used. In practice however, some requirements will have to be fulfilled in order to become a potential candidate for the application.
Assume that the input-output power transfer P_{OUT}=$f(P_{IN})$ is accurately known and we can define an "input threshold power" (P_{thr}) which is smaller than the minimum signal power. We divide the original power span (interval 1 to N) in N intervals of equal width on a dB-scale (d), such that the minimum power of the span is equal to P_{thr}. This enables the expression of the average output power as the weighted sum of the probabilities that the signal power lies within these intervals (X(i)). The weights can be calculated from a discretized version of f, namely O(i). Incrementing the attenuation with d between

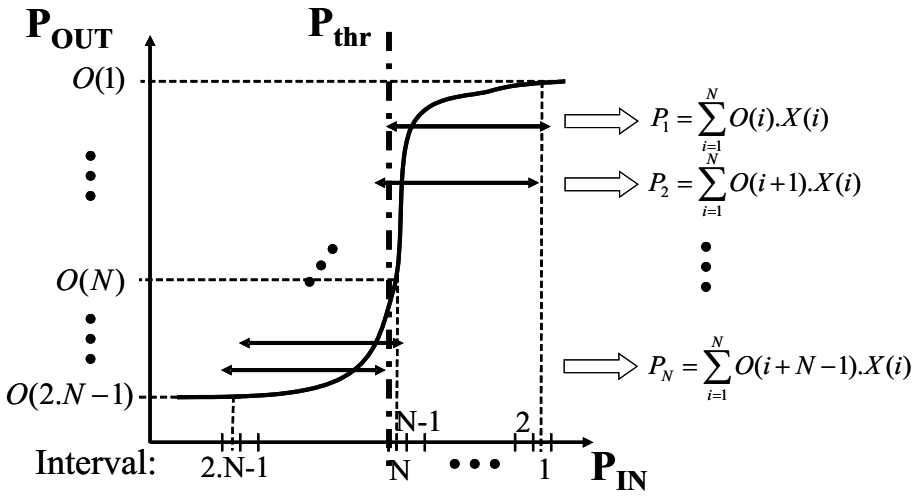

Figure 3.2: The principle of the proposed method is displayed, together with the symbols used in the discussion. The dash-dotted line indicates the "input threshold power" of the given non-linear gate. The double arrow next to each equation depicts the power span in which the signal is located during the measurement of the corresponding average output power.

each average power measurement results in a set of linear equations with the mentioned probabilities as unknowns. The projection of adjoining intervals onto each other during subsequent measurements is illustrated by the double arrows in Fig. 3.2. They represent the power span in which the signal is located during each power measurement. It is clear that as soon as we performed at least N measurements, the entire signal is shifted over the threshold power.
In this way we obtain at least N equations in N unknowns, i.e. a linear system $\mathbf{O}.\mathbf{X} = \mathbf{P}$. Subsequent rows of the system matrix $\mathbf{O}$ are formed by slightly shifted (with a power shift equal to d) parts of the decision characteristic. In theory the only requirement for a unique solution of the system is the existence of at least N linear independent rows. If we can achieve this, it is theoretically possible to calculate the logarithmically scaled asynchronous signal histogram.

A schematic of a practical setup is depicted in Fig. 3.3. It illustrates that besides a fast optical non-linear gate, only an adjustable attenuator, a low speed photodiode and some signal processing circuitry are needed. This means that the asynchronous histogram can be constructed without the need of any sampling system or high-speed electronics. The obtained accuracy will depend on several parameters, including

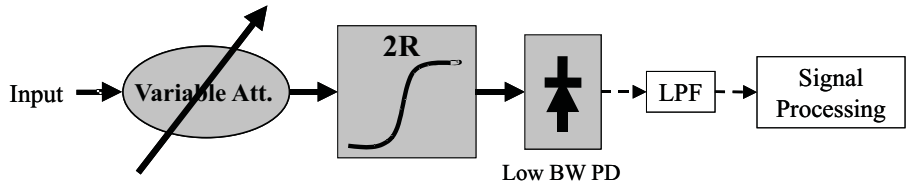

Figure 3.3: The proposed configuration is schematically depicted. Att.: attenuator, 2R: 2R regenerator, Low BW PD: low bandwidth photodiode, LPF: electrical low pass filter. full line: optical signal; dashed line: electrical signal.

the input-output power relation of the non-linear gate, the speed of the gate, the information extraction strategy, the stability of the configuration, etc. A compromise will always have to be made in a practical setup.

3.3 Simulation strategy

To study the theoretical feasibility of the method, together with the requirements imposed on the different components in a practical implementation, a simulation platform was developed. Several precautions were taken in order to bring the model as close to reality as possible, i.e. experimentally obtained data signals and decision characteristics were included.

A benchmark set of signals was constructed out of experimentally obtained asynchronous probability distributions. Two types of signals were investigated.

The first set of histograms consisted of signals mainly degraded by amplifier noise, while still showing rather steep transitions. Such histograms are still very well approximated by the sum of 2 separate Gaussian distributions, since the contributions due to the bit flanks are negligible. These signals will always be referred to as the **noisy signals**. An example of such a histogram is depicted in Fig. 3.4.

A second set of signals was achieved by propagating a high bit rate signal through a dispersive optical fiber, resulting in distortion by chromatic dispersion (CD). The rise time of the flanks of those signals is not negligible anymore as compared to the bit period, therefore some remaining power in between the marks and spaces is present in the asynchronous histogram. An example is depicted in Fig. 3.4. We note immediately that the fitting of two separate Gaussian distributions to

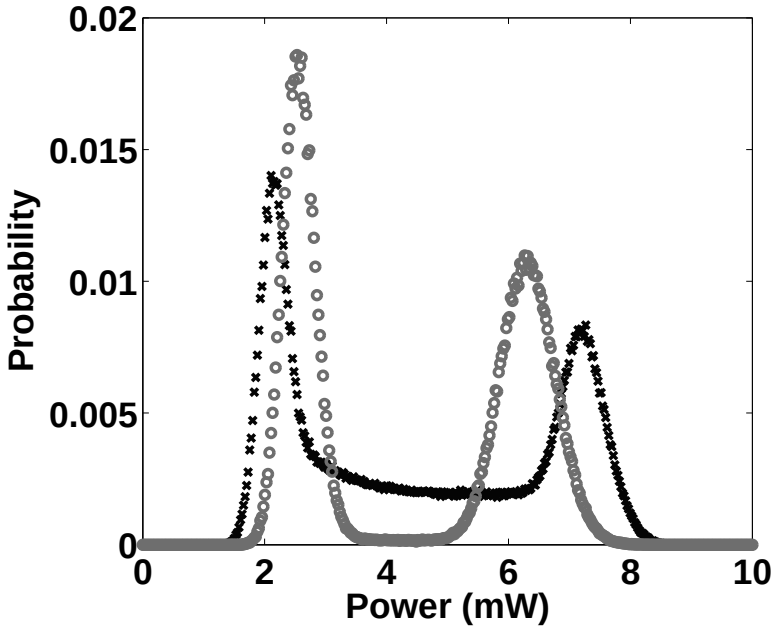

Figure 3.4: Two histograms obtained from realistic data signals are depicted. The circles correspond to a noisy signal and the crosses represent a signal distorted by CD. The resp. Q-average values are 5.14 and 6.50.

the complete histogram will be less successful in this case. Those signals will be referred to as the **distorted** set.
Within each set of signals, the Q-average was varied between 3.1 and 7.5. This corresponds to a range of approximately 10 dB to 17.5 dB if expressed on a logarithmic scale ($Q_{log} = 20.log_{10}(Q_{lin})$). In this way, high quality as well as low quality signals are included. The processability of those two sets of signals was used as a figure of merit of the different methods studied.

To model the optical non-linear gate, we used experimentally obtained regeneration curves of several types of 2R regenerators available at our lab. The choice of the regenerators will be motivated in a later section.

The combination of a signal and a non-linear power relation enabled the construction of the linear system $\mathbf{O}.\mathbf{X} = \mathbf{P}$. The system matrix $\mathbf{O}$ could be constructed once an initial power span, an interval width and the number of measurements were chosen. The average power

vector **P** could be calculated as described in section 3.2, i.e. by applying different attenuated versions of the same data signal to the gate.

To simulate measurement noise, a normally distributed perturbation with a relatively small standard deviation (σ_N) was added to **P**. This is relevant since measurements revealed that rather smooth mean power vectors could be obtained due to the averaging. This will be illustrated in chapter 4. In principle, the perturbations can be added either on a linear or a logarithmic scale, depending on the optical power unit used during the measurements. We will however always apply an addition on a logarithmic scale since the power measurements were performed on a dBm scale. In addition, the accuracy specifications of the optical power meter used in the experiments were defined as $\pm$ 2.5%, what is equivalent to $\pm$ 0.1 dB. This will probably be somewhat lower in our setup, due to the averaging of several measurements.

The described theoretical setup thus models the configuration if a fast non-linear gate characteristic is present, and deviations in average power are of random nature.

As will be described in the following section, different methods were developed to extract the histogram out of the constructed linear system. To compare the different extraction methods as well as the suitability of several regenerator configurations, a quantitative measure for the quality of the extracted histograms has to be provided. We opted for the Q-average method making use of the cut-and-delete technique explained in section 2.2.1 with an α-value equal to 0.3 [22]. This is motivated by the great potential of this technique in several practical applications.

3.4 Histogram extraction methods

As was explained previously, subsequent rows of the system matrix **O** consist of slightly shifted parts of the used power transfer (cf. the double arrows in Fig. 3.2, each corresponding to a row of **O**). Therefore subsequent rows are almost linear dependent, since they only differ in one single entry. This is the main reason why the linear system to be solved is **very ill-conditioned** in a lot of practical cases.
A linear system, $\mathbf{O}.\mathbf{X} = \mathbf{P}$, is called ill-conditioned if very small perturbations in **O** or **P** can lead to relatively large changes in the extracted solution **X**. This is of course highly undesirable in any practical implementation. The degree of conditioning of a matrix can be quantified by

calculating the condition number [1] of **O**, which is defined as:

$$\kappa(O) = \|O\| \,.\, \left\|O^{-1}\right\| \qquad \text{if} \qquad O \in \Re^{nxn} \tag{3.1}$$

$$\kappa(O) = \|O\| \,.\, \left\|O^{+}\right\| \qquad \text{if} \qquad O \in \Re^{mxn} \tag{3.2}$$

for square and rectangular matrices respectively. The + denotes the pseudo-inverse of a rectangular matrix, defined by

$$O^{+} = \left(O^{T}.O\right)^{-1}.O^{T} \qquad \text{if} \qquad rank(O) = n. \tag{3.3}$$

The condition can be interpreted as some kind of amplification factor of the influence of perturbations present in **O** or **P** on the final solution. This can be understood by inspecting equation 3.5, which gives an upper bound for the relative error of the solution of the perturbed square linear system of equation 3.4, obtained by some kind of matrix inversion [61]. It can be seen that the relative error in the solution can be $\kappa(O)$ times the relative error in **O** and **P**.

$$(O + \varepsilon.\delta O).X = (P + \varepsilon.\delta P) \tag{3.4}$$

$$\frac{\|X - X_{orig}\|}{\|X\|} \leq \kappa(O).\left(\varepsilon.\frac{\|\delta O\|}{\|O\|} + \varepsilon.\frac{\|\delta P\|}{\|P\|}\right) + \mathrm{O}(\varepsilon^2) \tag{3.5}$$

In this sense, $\kappa(O)$ quantifies the sensitivity of the given system. A system is called ill-conditioned if it has a large condition number, where "large" means roughly $log_{10}(\kappa(O)) \geq$ the precision of the matrix entries [62]. It is obvious that during further research, the condition number of a given configuration will be used as a first indication of its feasibility.

To conclude we can say that we have to deal with an unstable, ill-conditioned linear system. An interesting and important fact is that ill-conditioning does not mean that a meaningful, approximated solution cannot be computed. It only implies that standard algebraic methods to

[1] The definition of the condition number is linked directly with a definition of the matrix norm $\|O\|$. Different definitions exist. Throughout this work, we will always use the matrix 2-norm defined as $\|O\|_2 = \sup_{x \neq 0} \frac{\|Ox\|_2}{\|x\|_2}$ with $\|x\|_2 = \left(\sum_{i=1}^{n} |x_i|^2\right)^{1/2}$ being the 2-vector norm. ($\sup_{x \neq 0} \ldots$ stands for the x, different from the null-vector, that maximizes the argument.) In terms of the singular value decomposition of **O** (Equation (3.8)), the matrix 2-norm can also be expressed as $\|O\|_2 = \sigma_1$, i.e. the norm equals the biggest singular value of **O**. The condition number calculated in the 2-norm is therefore equal to the ratio of the biggest and the smallest singular value of **O** [61]

solve linear systems methods such as Cholesky, LU or QR-factorization can not be used in a straightforward manner, since they produce absurd results. Therefore, we had to search for other methods in order to find reasonable solutions for the problem. This brought us to two classes of extraction methods, which will be explained in the following sections.

3.4.1 Regularization

Discrete ill-posed problems occur in a variety of applications such as astronomy, electrocardiography, computerized tomography, mathematical physics, etc. Therefore, a lot of research has been done on how to tackle those kind of problems, such that reasonable solutions can be found. Most methods try to replace the problem with a "nearby" well-conditioned problem whose solution is a good approximation of the required solution, and in addition, is a more satisfactory solution than the ordinary (least squares) solution. This can be done by incorporating further information about the desired solution. Such methods are called **regularization methods** [63].

The most commonly used side constraint is to limit the norm, or an appropriate semi-norm, of the solution. Sometimes, if available, an initial estimate $\mathbf{X}^*$ can be included, thereby aiming for the minimization of the quantity

$$\Omega(\mathbf{X}) = \|\mathbf{L}.(\mathbf{X} - \mathbf{X}^*)\|_2 . \tag{3.6}$$

$\mathbf{L}$ typically is the unitary matrix ($\mathbf{I}_n$) or an p x n approximation of the $(n-p)$-th derivative operator. In principle $\mathbf{L}$ can also be a more complex linear combination of the previously mentioned choices. In fact it always results in the control of the smoothness of the solution in some way. By introducing this side constraint, the requirement $\mathbf{O}.\mathbf{X} = \mathbf{P}$ (for $m = n$) or $min\ \|\mathbf{O}.\mathbf{X} - \mathbf{P}\|$ (for $m > n$) of course has to be relaxed. In other words we try to find a good compromise between both the residual norm $\|\mathbf{O}.\mathbf{X} - \mathbf{P}\|$ and the semi-norm $\|\Omega(\mathbf{X})\|$. The relative weight of both minimizations is controlled by means of a regularization parameter. For the best-known regularization method, Tikhonov regularization, this results in the following minimization problem:

$$\mathbf{X}_\lambda = \arg\min \left\{ \|\mathbf{O}.\mathbf{X} - \mathbf{P}\|_2^2 + \lambda^2 . \|\Omega(\mathbf{X})\|_2^2 \right\} . \tag{3.7}$$

One can clearly see the influence of the regularization parameter λ on the solution of the problem. A carefully chosen λ will be as important as the solution of the resulting minimization problem. If λ is chosen

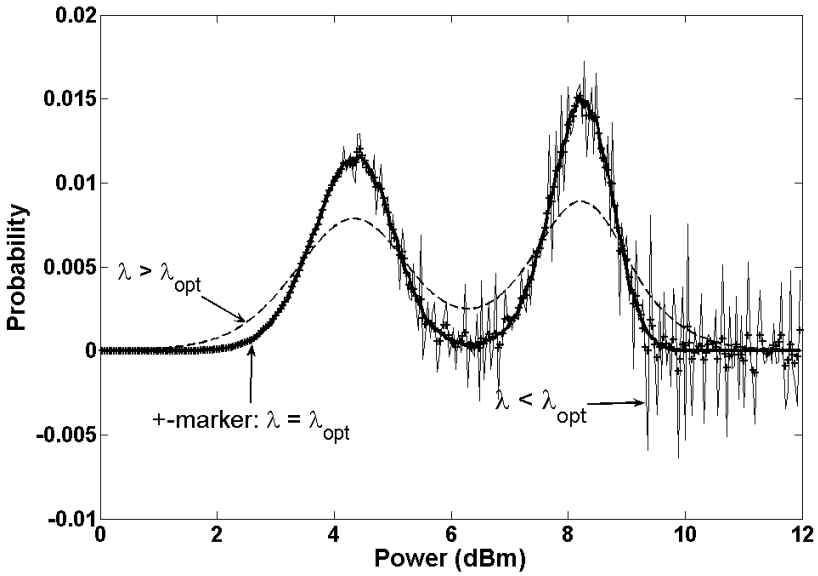

Figure 3.5: Illustration of different histograms resulting from the Tikhonov method with $\mathbf{L}=\mathbf{I}_n$ (equation (3.7)) corresponding to different values of the regularization parameter λ. λ_{opt} was calculated using the L-curve method. We see clearly the smoothing effect of the regularization. The thick full line represents the real histogram.

too large, an overregularized or oversmoothed solution will be found, showing a semi-norm which is too small. If on the other hand λ is chosen too small, we will again obtain a chaotic, high-frequency solution, as was the case when using classical calculation methods. This is illustrated in Fig. 3.5 where the Tikhonov solution resulting from equation 3.7 is plotted for some different values of the regularization parameter. The practical configuration, i.e. the regeneration characteristic, used to compute this example is of no interest here. This example clearly illustrates the great importance of a decent λ-choice.

The Tikhonov method is only one of many possible regularization methods. The methods can be divided in direct, iterative and hybrid methods. A good overview of the different regularization strategies can be found in [64]. The accompanying Matlab package developed by P.C. Hansen ([65]) was used to test the feasibility of the different approaches in our specific case.

regu method	L	λ choice	I	II	III
pseudo inverse			0.06	0.05	0.06
Tikhonov	I	L curve	**0.99**	0.85	0.29
Tikhonov	L1	L curve	**1.00**	0.2	0
Tikhonov	L2	L curve	0.82	0.04	0
Tikhonov	L3	L curve	0.46	0.06	0
Tikhonov	I	GCV	**1.00**	0.89	0.55
Tikhonov	L1	GCV	**1.00**	**0.91**	0.54
Tikhonov	L2	GCV	**1.00**	**0.93**	0.53
Tikhonov	L3	GCV	**1.00**	**0.95**	0.54
Tikhonov	I	quasi-opt	0.47	0.08	0
Tikhonov	L1	quasi-opt	0	0	0
Tikhonov	L2	quasi-opt	0	0	0
Tikhonov	L3	quasi-opt	0	0	0
Truncated SVD	I	L curve	**0.95**	**0.90**	0.66
Truncated SVD	L1	L curve	0.86	0.45	0.48
Truncated SVD	L2	L curve	0.56	0.39	0.29
Truncated SVD	L3	L curve	0.37	0.41	0.17
Truncated SVD	I	GCV	**1.00**	**0.94**	0.65
Truncated SVD	L1	GCV	**1.00**	**0.94**	0.68
Truncated SVD	L2	GCV	**1.00**	**0.94**	0.68
Truncated SVD	L3	GCV	**1.00**	**0.95**	0.7
Truncated SVD	I	quasi-opt	**0.90**	0.75	0.5
Truncated SVD	L1	quasi-opt	0.72	0.56	0.36
Truncated SVD	L2	quasi-opt	0.15	0.1	0.03
Truncated SVD	L3	quasi-opt	0	0	0
Damped SVD	I	L curve	0.69	0.03	0
Damped SVD	L1	L curve	0.05	0	0
Damped SVD	L2	L curve	0	0	0
Damped SVD	L3	L curve	0	0	0
Damped SVD	I	GCV	**0.93**	0.82	0.51
Damped SVD	L1	GCV	**0.98**	0.85	0.55
Damped SVD	L2	GCV	**1.00**	0.88	0.54
Damped SVD	L3	GCV	**1.00**	**0.92**	0.55
Damped SVD	I	quasi-opt	0	0	0
Damped SVD	L1	quasi-opt	0	0	0
Damped SVD	L2	quasi-opt	0	0	0
Damped SVD	L3	quasi-opt	0	0	0

Table 3.1: Column I, II and III denote the fraction of the tested signals that rendered a Q_{avg} with a 10% accuracy when normally distributed error vectors were added with an amplitude of resp. .05, .1 and .2 dB. Interval width of .02 dB was chosen. λ choice: method used for choosing the regularization parameter. L gives the smoothness operator used (I=Unitary matrix, L1, L2 and L3 are approximations of resp. the first, second and third derivative operator). quasi-opt: quasi-optimality criterium.

Apart from the different regularization methods, also different approaches exist to choose an appropriate regularization parameter. Two types exist, differing in whether they incorporate a priori information about the error or not. Of course we will only use the latter, in order to maintain the transparency of the method. The most famous one is the L-curve method, which searches for the best compromise between the residual and the semi-norm by plotting the logarithm of both norms in a XY-plane for different values of λ. This results in the typical L-shape, where the best value of λ is the one in the corner of the L.

In search of the "best" regularization strategy for our specific problem, we investigated the suitability of all the methods described in [64]. The different regularization methods were combined with the different methods to choose the regularization parameter. The feasibility was mainly evaluated by the overall quality of the extracted results in case several versions of the benchmark set of signals were applied.
In our study, it turned out that one method to choose the regularization parameter performed significantly better as compared to the others. It consisted of the **Generalized Cross-Validation method (GCV)**, first introduced by Golub et al. [66]. Of the regularization methods, the **Truncated (Generalized) Singular Value Decomposition (T(G)SVD)** performed the best, be it somewhat less pronounced than the difference in quality between the methods to choose the regularization parameter. It should be noted that finding **"the best"** method is not straightforward. More appropriate to say is that we looked for the method that produced the best results for most of the tested cases. This is a common problem with ill-posed problems. In [67] it was stated that any technique for choosing regularization parameters in the absence of information about the error level can be defeated by suitably constructed counterexamples. Therefore it is almost impossible to find a method that will produce accurate results in any possible case.

Table 3.4.1 illustrates that it is indeed the method for choosing the regularization parameter that is the most important. The table contains the percentage of a benchmark set of signals that resulted in a Q_{avg} estimation with a 10% accuracy if applied to a static power transfer as in Fig. 3.19. The calculated mean power vectors are disturbed by a noise component with the mentioned strengths. The set of signals were deduced from theoretically constructed asynchronous histograms consisting of the sum of two perfect Gaussian distributions such that linear Q_{avg}-values between 3 and 7 were obtained. Note that only the results corresponding to the direct methods tested are given. As a reference,

also the accuracy of the solution obtained by simple pseudo inversion is given (cf. Eq.3.3). The poor results of this method clearly illustrates the importance of the regularization methods.
Since the combination of T(G)SVD with GCV will be used throughout the rest of this work, those methods will now be explained in some more detail.

Two very interesting tools in the analysis of discrete ill-posed problems are the singular value decomposition (SVD) and the generalized singular value decomposition (GSVD) of the system matrix.
If $\mathbf{O} \in \Re^{m\text{xn}}$ with $m \geq n$, then the SVD of **O** is given by

$$\mathbf{O} = \mathbf{U}\Sigma\mathbf{V}^T = \sum_{i=1}^{n} \mathbf{u}_i \sigma_i \mathbf{v}_i^T, \tag{3.8}$$

where **U** and **V** are matrices with orthonormal columns, i.e. $\mathbf{U}^T\mathbf{U} = \mathbf{V}\mathbf{V}^T = \mathbf{I}_n$ ($\mathbf{I}_n$ is the n x n unitary matrix) and $\Sigma = diag(\sigma_1, ..., \sigma_n)$. The numbers σ_i are called the singular values of **O** and are ordered in a decreasing way. The least squares solution of **O**.**X**=**P** can be expressed as follows:

$$\mathbf{X}_{LSQ} = \sum_{i=1}^{n} \frac{\mathbf{u}_i^T \mathbf{P}}{\sigma_i} \mathbf{v}_i. \tag{3.9}$$

An important property of the singular values associated with an ill-posed problems is that they decay gradually to zero with no particular gap in their spectrum [64]. Moreover the singular vectors corresponding to those small singular values tend to have a lot of sign changes in their elements. Observing equation (3.9) it is clear that the solution will be dominated by the terms corresponding to the smallest σ_i, thereby having a lot of sign changes and appearing completely random. The purpose of a regularization method is therefore to filter out or dampen those high frequency components.
The GSVD can be constructed out of a given matrix pair (**O**, **L**) and is useful in the handling of ill-posed problems where an extra constraint related to the semi-norm is included. Assume we have $\mathbf{O} \in \Re^{m\text{xn}}$ and $\mathbf{L} \in \Re^{p\text{xn}}$ with $m \geq n \geq p$, then the GSVD is given by the following decompositions:

$$\mathbf{O} = \mathbf{U} \begin{pmatrix} \Sigma & \mathbf{0} \\ \mathbf{0} & \mathbf{I}_{n-p} \end{pmatrix} \mathbf{Y}^{-1} \qquad \text{and} \qquad \mathbf{L} = \mathbf{V}\,(\mathbf{M}, \mathbf{0})\,\mathbf{Y}^{-1}. \tag{3.10}$$

$\mathbf{U} \in \Re^{m\text{xn}}$ and $\mathbf{V} \in \Re^{p\text{xp}}$ are again orthonormal and $\mathbf{Y} \in \Re^{nxn}$ is non-singular, $\Sigma = diag(\sigma_1, ..., \sigma_p)$ and $\mathbf{M} = diag(\mu_1, ..., \mu_p)$. The σ_i are now

ordered in an increasing way, whereas σ_i monotonically increase with i. Moreover they are normalized such that

$$\sigma_i^2 + \mu_i^2 = 1 \qquad i = 1, ...p. \tag{3.11}$$

The generalized singularized values of (**O**,**L**) are defined as

$$\gamma_i = \sigma_i/\mu_i, \qquad i = 1, ...p \tag{3.12}$$

and appear in a non-decreasing order. The same remark about the amplitude of the generalized singular values corresponding to ill-posed problems can be made as for the singular values.
The same symbols appear in both equation (3.8) and (3.10), while having a different definition. In the discussion it will however always be clear from the context which definition is used. The GSVD is the same as the SVD if $\mathbf{L} = \mathbf{I}_n$, except from the ordering of σ_i.
As was explained, regularization aims at filtering out the high frequency contributions corresponding to small (generalized) singular values. In the TSVD (and TGSVD) method, this is done by replacing the system matrix **O** by a rank deficient well-conditioned matrix $\mathbf{O}_k$, by truncating the SVD-expansion 3.8.

$$\mathbf{O}_k = \sum_{i=1}^{k} \mathbf{u}_i \sigma_i \mathbf{v}_i^T \qquad \text{with} \qquad \mathrm{k} \leq \mathrm{n}. \tag{3.13}$$

TSVD and TGSVD can therefore be formulated as the solution of:

$$min\,|\mathbf{X}| \qquad \text{subject to} \qquad \min|\mathbf{O}_\mathrm{k}\mathbf{X} - \mathbf{P}| \tag{3.14}$$

$$min\,|\mathbf{L}\mathbf{X}| \qquad \text{subject to} \qquad \min\left|\overline{\mathbf{O}}_\mathrm{k}\overline{\mathbf{X}} - \overline{\mathbf{P}}\right|, \tag{3.15}$$

where $\overline{\mathbf{O}}$, $\overline{\mathbf{X}}$ and $\overline{\mathbf{P}}$ are matrices obtained from resp. **O**, **X** and **P** by a transformation described in [64]. This will not be explained in detail, since it is only a numerical issue. $\overline{\mathbf{O}}_k$ is again a truncated version of **O** analog to equation (3.13). The solution of the resp. minimization problems can be written as:

$$\mathbf{X}_k = \sum_{i=1}^{k} \frac{\mathbf{u}_i^T \mathbf{P}}{\sigma_i} \mathbf{v}_i. \tag{3.16}$$

$$\mathbf{X}_{k,\mathbf{L}} = \sum_{i=p-k+1}^{p} \frac{\mathbf{u}_i^T \mathbf{P}}{\sigma_i} \mathbf{y}_i + \sum_{i=p+1}^{n} (\mathbf{u}_i^T \mathbf{P}) \mathbf{y}_i. \tag{3.17}$$

Note that the σ_i in both equations are different, since they are calculated by equation (3.8) and (3.10) respectively. The discrete parameter k is the regularization parameter, i.e. we will regularize by discarding all the contributions corresponding to singular values smaller than σ_k.

As was mentioned previously, the method used to choose a good value for k that produced the best results was the GCV-method. This method is based on the statistical consideration that a good value of k should predict missing values in **P**. This leads to the minimization of the GCV-function

$$GCV(k) = \frac{\|\mathbf{OX}_{reg}(k) - \mathbf{P}\|_2^2}{\left(trace\left(\mathbf{I}_m - \mathbf{OO}^I(k)\right)\right)^2}, \tag{3.18}$$

where $\mathbf{O}^I(k)$ is the matrix producing the regularized solution $\mathbf{X}_{reg}(k)$ after multiplication with **P**. In [63] it is shown that GCV indeed searches for a good compromise between the regularization error and the perturbation error. It is interesting to mention that GCV fails if a correlated perturbation is present. In our simulations the errors are random, thereby rendering good results. If the errors would become correlated, better results can be obtained using the L-curve described previously.

To summarize we can state that different regularization methods were studied in order to find a realistic solution for the ill-posed linear system we have to deal with. In our test cases, the **T(G)SVD-method combined with the GCV-method for the choice of the regularization parameter** produced the most accurate results. Changes to the type of perturbations may lead to somewhat poorer results in some cases (e.g. if the errors are correlated). However, due to the use of a mathematical package containing implementations of a whole series of regularization algorithms extension to other methods is easily achievable [65].

3.4.2 Forward Multiplication

Apart from the regularization approach we developed a fitting algorithm to find a reasonable solution for the ill-conditioned linear system. The idea originated from the fact that by avoiding the calculation of the inverse of the system matrix, or a suitable approximation, a much more stable mathematical operation could be performed, i.e. simple forward multiplication of the system matrix. This can be understood by the expression of the product **OX** in terms of the singular values of **O** [64]:

$$\mathbf{OX} = \sum_{i=1}^{n} \sigma_i \left(\mathbf{v}_i^T \mathbf{X}\right) \mathbf{u}_i. \tag{3.19}$$

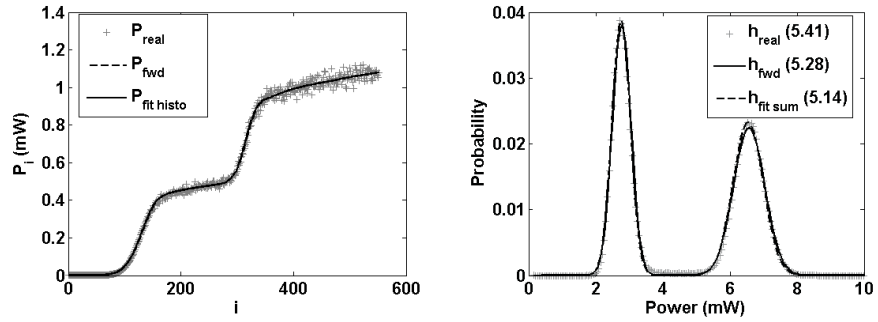

(a) (b)

Figure 3.6: Illustration of the forward multiplication approach using the sum of two Gaussian distributions in the case of a noisy signal. In (a) the slightly distorted **P**-vector is depicted (P_{real}), together with the **P**-vector resulting from the described algorithm (P_{fwd}). In (b) the corresponding histogram is depicted (h_{fwd}), together with the original histogram (h_{real}). h_{fitsum} in (b) depicts the result of a direct fitting of the sum of two Gaussian distributions to the original histogram, while in (a) the corresponding back-calculated **P**-vector is also drawn. Note that in this case the difference between both approaches is almost negligible. The regenerator characteristic used in this example is depicted in Fig. 3.19. In the legend the extracted Q_{avg}-values are given.

Remember that an important property of a discrete ill-posed problem was the presence of very small singular values, combined with singular vectors with a lot of sign changes in their elements. This leads to an amplification of the high frequency of **P**, as could be seen from equation (3.16). The forward multiplication in equation (3.19) does avoid the inversion of the small singular values, thereby achieving in fact a damping of the high frequency components present in **X**. Intuitively it is therefore easy to understand that this forward multiplication is much less sensitive to perturbations. This was verified by applying perturbations to a known solution **X** and to the corresponding **P**, and then comparing the results of equation (3.16) and (3.19). It came forward that in the case of the inversion, very small perturbations lead to extremely poor results, while in the forward multiplication scheme big deviations still rendered accurate representations of **P**.

A drawback of this approach is of course the fact that we have to specify the possible set of solutions by choosing a certain parameterized representation of the considered histograms. This results in a de-

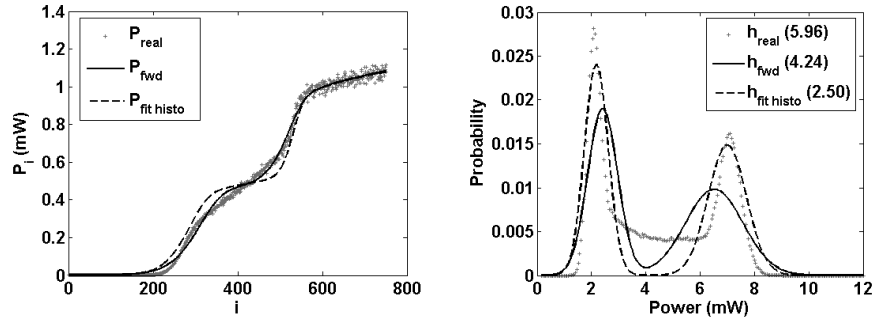

(a) (b)

Figure 3.7: The same explanation as the caption of Fig. 3.6 holds for this figure, showing the results corresponding to a distorted signal. Note that now there is a significant difference between both fitting approaches.

crease of the transparency of the monitoring method. Two different approaches were studied.

Sum of Gaussian distributions

The most obvious choice of possible solutions is the set of histograms consisting of a sum of two Gaussian distributions. This assumption results in a description of the possible solution in function of only 4 parameters:

$$f(t) = \frac{1}{2}\sum_{i=1}^{2} \frac{1}{\sqrt{2\pi}\sigma_i} \exp\left(\frac{-(t-\mu_i)^2}{2\sigma_i^2}\right), \tag{3.20}$$

where t represent the interval centers equally distributed on a linear scale (with intervalwidth $= dt$). This assumption can be used in the case we are investigating NRZ-signals (non-return-to-zero) with equal probability for a one, resp. a zero. The resulting minimization problem can be formulated as:

$$\mathbf{X}_{sol} = \min_{\mathbf{X}\in f(t)} \|\mathbf{O}.\mathbf{X} - \mathbf{P}\|_2 . \tag{3.21}$$

An advantage is that the fitting parameters of equation 3.20 can immediately be used to calculate the averaged Q-factor of the signal under investigation. To improve the speed and quality of the fitting, an initial estimate is provided to the minimization problem, resulting from the

fitting of two Gaussian distributions to the derivative of a smoothed version of the average power vector.

The results obtained by this approach are of course heavily correlated with the signal type under investigation. For the noisy signals introduced in section 3.3 the fitted curve can accurately reproduce the original histogram, whereas for the distorted set of signals this good agreement is much more difficult to achieve. It is important to understand that the fitting that occurs is the fitting of the product **OX** to the measured averaged power vector **P**, where **X** consists of a sum of two Gaussian distributions. In Fig. 3.7 it is illustrated that this fitting does not always result in the same solution as the direct fitting of a sum of two Gaussian distributions to the original probability distribution (note that this is of course not a practical possibility, since the original distribution is exactly the unknown). This is caused by the different relative importance of the data entries related to the transitions between the zeros and the ones in both fittings. Those are taken more into account in the first approach. Therefore the poor results in the case of the distorted histograms have two origins. First there is the fact that perfect agreement is unachievable as such, combined with the difference in the result between the two fitting approaches mentioned. Note that in the case of the noisy signals these problems do not occur. In that case both fitting approaches do almost coincide (Fig. 3.6).
At the moment the simulation results will be discussed (section 3.6 and 3.7.3), it will be demonstrated that if the main source of degradation is amplifier noise, the proposed fitting approach can indeed be very interesting.

It is worth noting that the results for the distorted histograms can be improved by including more Gaussian distributions in the objective function. Now each Gaussian distribution has a independent amplitude, not being correlated with the standard deviation as was the case in equation (3.20). This does however significantly increases the required calculation time. Therefore this is not interesting for a practical implementation.

Partial fitting

The fitting result displayed in Fig. 3.7 illustrates a clear limitation of the proposed approach if a Q_{avg} estimate has to be made in the presence of cross-point data. The fact is that the fitting does not make any distinction between the origin of the **P**-entries with respect to the

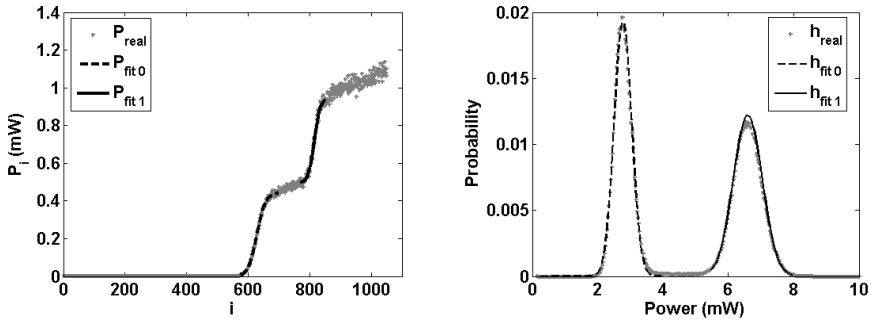

(a) (b)

Figure 3.8: Illustration of the resulting histogram (b) after partial fitting of the **P**-vector if a noisy signal is applied. The two separate fitted parts of **P** are depicted in (a). The original and the extracted Q_{avg} are 5.41 and 5.42 respectively. The transfer curve used for this simulation is depicted in Fig. 3.19.

signal, which is different from the approach used in the Q_{avg} calculation, where the data corresponding to the bit flanks are partially discarded. This brought us to a fitting approach in which we tried to take as much as possible the same parts into account as done during the Q_{avg}-extraction.

An important note is however that this has to be done in an iterative way, since the only initial information we have is the measured average power vector **P**, whereas the parts considered by the Q_{avg} algorithm are defined by the means and standard deviations of the fitted Gaussian distributions to the probability distribution as explained in section 2.2.1. The proposed algorithm can be summarized as follows:

1: The histogram is estimated by taking the derivative of a smoothed version of **P**. The corresponding Q_{avg} is calculated.
2: The extracted parameters in the Q_{avg}-calculation are used to select the parts of **P** that should be incorporated in the fitting. An explanation of how the parts of the **P**-vector corresponding to the marks resp. spaces are defined is given below.
3: The selected **P**-segments are fit separately to the product of the corresponding rows of **O** and the entire **X**-vector. Depending on the slope of **P** between the selected parts a noisy or a distorted parametric expression of the histogram is used. If the slope is small, **X** consists of a single Gaussian (noisy signal), whereas if a big slope is

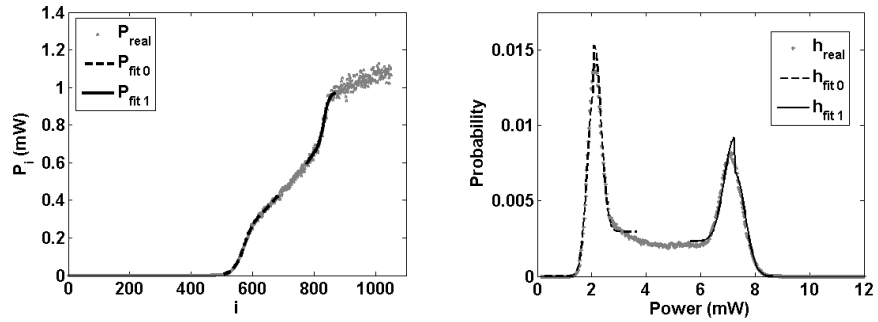

(a) (b)

Figure 3.9: Illustration of the partial fitting algorithm in the case of a distorted signal. Note the discontinuities at both peaks in the fitted histogram (b) due to the piecewise constant component in the objective function. The fitted **P**-vector parts are depicted in (a). The original and the extracted Q_{avg} are 5.96 and 6.11 respectively. The transfer curve used for this simulation is depicted in Fig. 3.19.

obtained **X** is build up out of the sum of a Gaussian distribution and a piecewise constant term representing the cross-point data (distorted signal). The piecewise constant component reaches from the top of the Gaussian peak until the lower bound of the fitting region representing the marks (resp. the upper bound for the spaces region).

4: Q_{avg} is calculated out of the fitting of a single Gaussian to both fitted histogram parts separately.

5: If the difference between the new and the old Q_{avg} is more then .5% we return to step 2.

The way the parts of **P** are selected, are based on the fact that an optical gate is used with an inverted characteristic (i.e. low output power for high input power and vice versa). In practise, certain power intervals are selected based on a process similar to the cut-and-delete technique. Once those power limits are chosen, the corresponding indices of the **P**-vector are calculated.
For the part corresponding to the "zeros", the considered power interval is ranging from the lowest interval edge till the interval edge the closest to $\mu_0 + \alpha(\mu_1 - \mu_0)$. For the "ones" we choose the powers closest to $\mu_1 - \alpha(\mu_1 - \mu_0)$ and $\mu_1 + \alpha(\mu_1 - \mu_0)$. The reason why we do not take the entire high power region into account, as we do with the low

power region in the case of the "zeros", is that in the "one" region the **P**-entries are influenced by the entire histogram. This makes the fitting inaccurate. In the case of the zeros however, this is not the case if the low output power of the gate is sufficiently low. This can be understood by noticing that even if only a few rows of **O** and a few entries of **P** are present in the expression to be minimized, **X** always remains entirely present. For the case of the "zeros" this can be written as:

$$\min_{\mathbf{X}\in f(t)} \|\mathbf{O}(1:pos_{0stop},1:n)\mathbf{X}-\mathbf{P}(1:pos_{0stop})\|_2 \tag{3.22}$$

whereas for the "ones" this results in:

$$\min_{\mathbf{X}\in f(t)} \|\mathbf{O}(pos_{1start}:pos_{1stop},1:n)\mathbf{X}-\mathbf{P}(pos_{1start}:pos_{1stop})\|_2 . \tag{3.23}$$

If on the other hand we would use a non-inverting optical gate, the intervals corresponding to the "zeros" should be limited instead of the "ones". Important to note is that in the case we have a transfer which is less steep, a shift proportional to the inverse of the slope has to be added to the estimated power intervals, in order to select the correct parts of **P**.

Fig. 3.8 and 3.9 illustrate the results of the proposed fitting approach in the case the same signals as used in Fig. 3.6 and 3.7 are applied. We can see this indeed leads to a significantly better estimate of Q_{avg} in the case of distorted signals. It should be noted that this iterative fitting algorithm takes of course more time as compared to the fitting of two Gaussian distributions.

3.5 Qualification of a good result

Before starting with the discussion of the simulation results, it is important to explain the methodology used to qualify an extracted histogram as a "good" result.

As mentioned before, we will calculate the averaged Q-factor corresponding to the extracted histogram. In a practical implementation this value will lead to a corresponding (synchronous) Q-factor, thereby often resulting in a BER estimate via equation (2.2). Due to the relationship between Q and the BER, small deviations of the Q-factor can lead to a significant difference in the corresponding BER, certainly if Q increases. In fact, this is a common problem that all the BER estimators based on direct Q-factor measurements have to deal with. Of course we

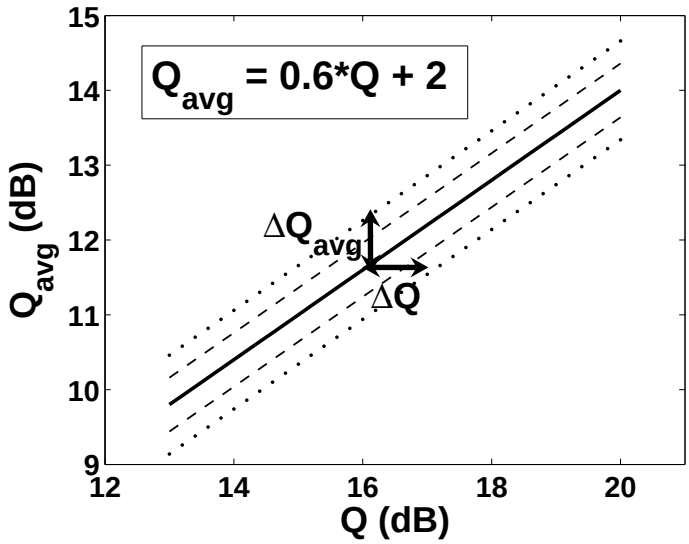

(a)

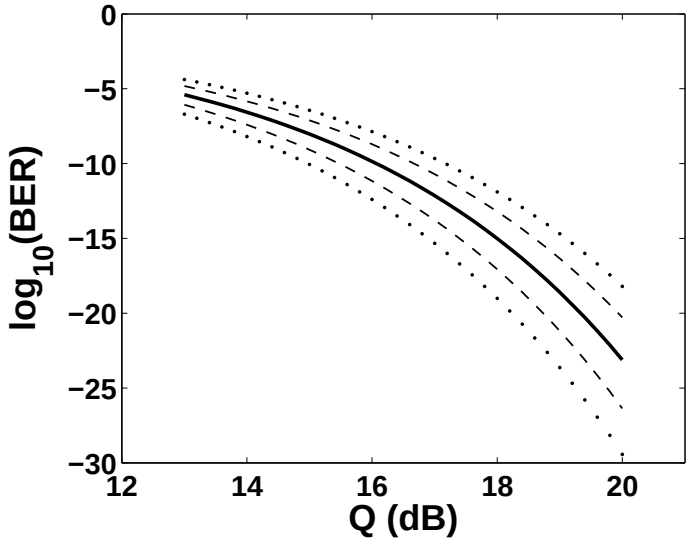

(b)

Figure 3.10: In (a) a Q_{avg}-Q relation as obtained in [43] is drawn by the full line. The corresponding linear expression is given in the inset. The dashed and the dotted lines represent the Q_{avg}-values corresponding to $Q \pm .6$ and $Q \pm 1.1$ respectively. In (b) the BER corresponding to the different lines in (a) are depicted.

retain the advantage that the measurement can be performed in-service by tapping a small part of the power. Actually, the real BER can only be measured out of service. Once in-service techniques are used based on either analog (e.g. Q-factor and optical signal-to-noise-ratio) or digital (e.g. error block detection, error count in forward error correction) parameters, only rough BER estimates can be provided. The degree of roughness of the results will depend on the different techniques and be inversely proportional to the complexity. Therefore in general a compromise has to be made between the obtained BER accuracy and the complexity of the method.

In the different experimental (and theoretical) setups presented making use of the averaged Q-factor for BER estimation, a linear relation was found between the averaged Q-factor and the synchronous Q-factor (obtained from the BER measurement) if both were expressed in dB (a.o. [4] and [45]). In [43] the dependence of the slope of this relation on several parameters such as optical and electrical bandwidth, α-value, etc. was extensively studied in the case signals were applied perturbed only by optical noise. It turned out that in most of the cases a slope between 0.4 and 0.7 was obtained. The fact that the slope is smaller than one is intuitively clear, since in the averaged Q-factor also part of the cross-point data are included, acting as some kind of unwanted information. The smaller α gets, the steeper the relation will become.
In literature [45], one result could be found in which the slope was slightly bigger than one. This was probably due to different bandwidths used in the measurement of the synchronous and asynchronous Q-factor respectively.

To illustrate the applied quality measure of the extracted Q_{avg}, a relation as obtained in [43] is depicted in Fig. 3.10(a), together with the corresponding mathematical expression. In Fig. 3.10(b) the full line shows the BER corresponding to different values of the Q-factor. The required accuracy of a histogram method can now be expressed as a limit on the tolerated deviation of the extracted Q-factor as compared to the real Q-factor, expressed in dB. As an example we assume a maximal $\Delta Q = 0.6$ dB, which approximately corresponds to a difference in BER between 10^{-10} and 10^{-9}. This can be seen in Fig. 3.10(b) were the two dashed lines represent the BER's corresponding to resp. $Q - \Delta Q$ and $Q + \Delta Q$. It is clear that by defining such a requirement to the extraction accuracy, this results in different bounding edges of the extracted BER's. I.e. for BER's in the vicinity of 10^{-9}, the BER will be extracted within one order of magnitude, but for lower BER's this won't be the

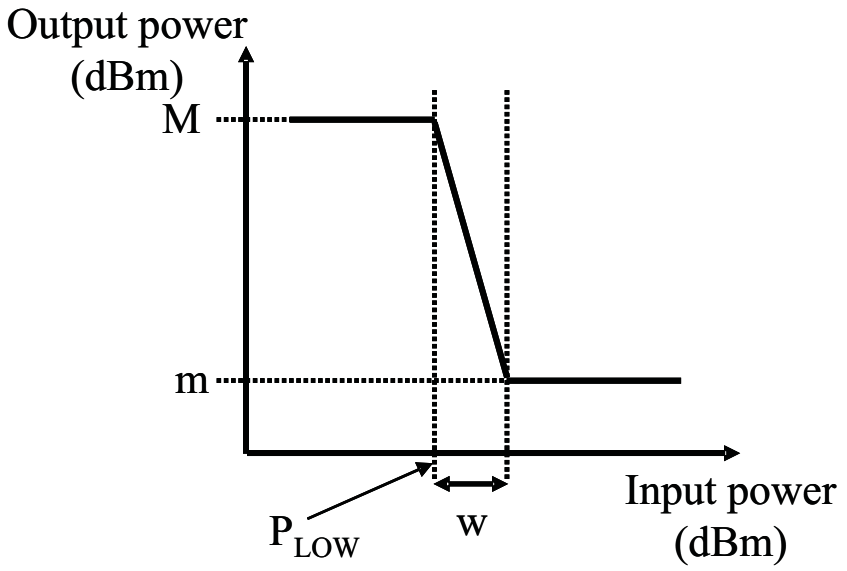

Figure 3.11: The general step-like transfer characteristic, with the different parameters.

case. For higher BER's the imposed constraint results in a more tightly bounded BER extraction. Due to the linear relation between Q_{avg} and Q, the required ΔQ_{avg} can be expressed as:

$$\Delta Q_{avg} \leq slope.\Delta Q. \tag{3.24}$$

In the given example this results in the requirement $\Delta Q_{avg} = 0.36\ dB$. Note that in this case the interesting range of Q_{avg} values is only situated between 10 and 14 dB (approximately between 3 and 5 on a linear scale).

In the case a more rough BER estimate is tolerated, e.g. two order of magnitudes at a BER of 10^{-9}, the requirements do relax to $\Delta Q = 1.1\ dB$ and $\Delta Q_{avg} = 0.66\ dB$. This is depicted on Fig. 3.10(a) and 3.10(b) by the dotted lines.

3.6 Limits and requirements curves

Before starting the search for a practical regenerator configuration suitable for the described application, it is important to define some kind of criterion on which the choice of a 'good' curve can be based.

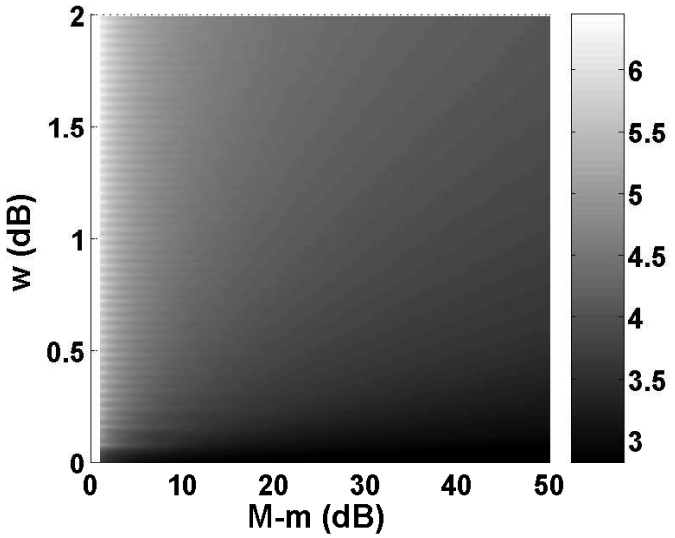

(a)

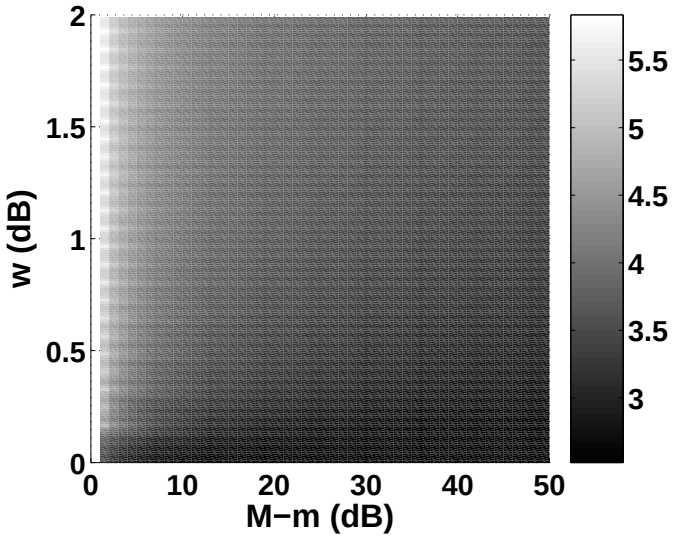

(b)

Figure 3.12: The logarithm of the minimal condition number of a system matrix constructed out of an ideal curve as depicted in Fig. 3.11 for a 20 dB wide power span. Interval widths were resp. (a) .04 and (b) .08 dB.

Since in the original idea an ideal step curve was used, the suitability of several versions of an ideal curve as depicted in Fig. 3.11 was investigated. First of all the condition numbers, as defined in Eq. 3.2, were calculated for a 20 dB wide power span, divided in intervals of .04 dB and .08 dB respectively. In both cases an additional power span of 1 dB was included to obtain some extra equations in the linear system. The condition numbers were minimized by properly choosing the position of the initial power span with respect to the non-linearity. It came forward that the optimal choice was to take the lower edge of the power span somewhere within $[P_{low}, P_{low} + d[$, with P_{low} the input power at which the output power starts to fall (see Fig. 3.11) and d the interval width. Doing this ensures that the complete power span has been shifted over the non-linearity in any case, i.e. for any value of w.
The logarithms of the resulting condition numbers are depicted in Fig. 3.12 for the two dimensional space spanned by the width and the relative height of the step. Those two parameters are actually the most important with respect to the conditioning of the resulting system matrix. The condition number turned out to be independent of the absolute step height. This is intuitively clear since the degree of linear dependence of the different rows does not change anything if the matrix is multiplied with a scalar. Analysis of Fig. 3.12 shows that globally spoken the most interesting transfers are those showing a steep transition in combination with a large relative step. This can be intuitively understood by thinking that the difference between subsequent rows does increase when we use those kinds of regenerators (think about the extreme case of a perfectly linear power transfer, that would result in an infinite condition number). Due to the significantly lower condition numbers for small values of the step width, the steepness is more influencing the conditioning as compared to the relative step height.
The discontinuities appearing in function of the step width for the smallest steps are caused by the discrete nature of the transfer. This results in a sudden increase of the linear dependency of different rows of the system matrix in the case the step width is a multiple of the interval width. It is however the global trend that is important in the selection of a decent regeneration curve, since those kinds of 'perfect' transitions will never appear in a practical implementation.

As a conclusion we can say that a power transfer with a **sharp transition** is highly desirable, combined with a **high relative difference in output power** between the on and off state.
An important note is that not only the condition number as such is im-

			$log_{10}(K)$	
w (dB)	**M (dB)**	**m (dB)**	d = .04 dB	d = .08 dB
0.75	0	-2	5.5855	5.1463
0.75	0	-6	4.7308	4.2748
1	10	-10	4.1546	3.7577
1	0	-20	4.1546	3.7577
1	-10	-30	4.1546	3.7577
1	10	-20	3.9747	3.6263
1	10	-30	3.8508	3.5622
0.5	0	-40	3.5773	3.2305
1.00E-06	0	-20	2.8469	2.6177
0.08	0	-24	3.1095	2.5813

Table 3.2: Parameters and corresponding condition numbers for the different versions of Fig. 3.11 used in the simulations. A fixed 20 dB wide power span starting at the middle of the transition was taken. d: interval width.

portant for the feasibility of a given configuration. We have to keep in mind that for a practical implementation a compromise has to be found between the steepness of the input-output power relation and the resemblance of the static and the dynamic power relation. It is intuitively clear that an extremely steep static power relation will be harder to be followed under dynamic conditions as compared to a less steep relation.

In order to demonstrate the correlation between the condition number of a given configuration and its suitability for the application, several versions of the ideal transfer of Fig. 3.11 were used as non-linear component in the simulation frame described in section 3.3. The parameter values of the different transfers, together with the corresponding condition numbers are given in Table 3.6. Note that a broad range of condition numbers is covered. In this case a fixed 20 dB wide power span with the lower edge equal to the center of the non-linearity was chosen. So in this case no optimization of the conditioning of the system matrix was performed.

We applied 650 different signals of the noisy type with Q_{avg}-values equally distributed between 9.9 and 17.5 dB to the different configurations. After perturbation of the calculated mean power vector with a normally distributed noise vector on a logarithmic scale, the histogram was extracted via the forward multiplication scheme with 2 Gaussian distributions and via the TSVD with GCV and L=I resp. L3. In Fig. 3.13

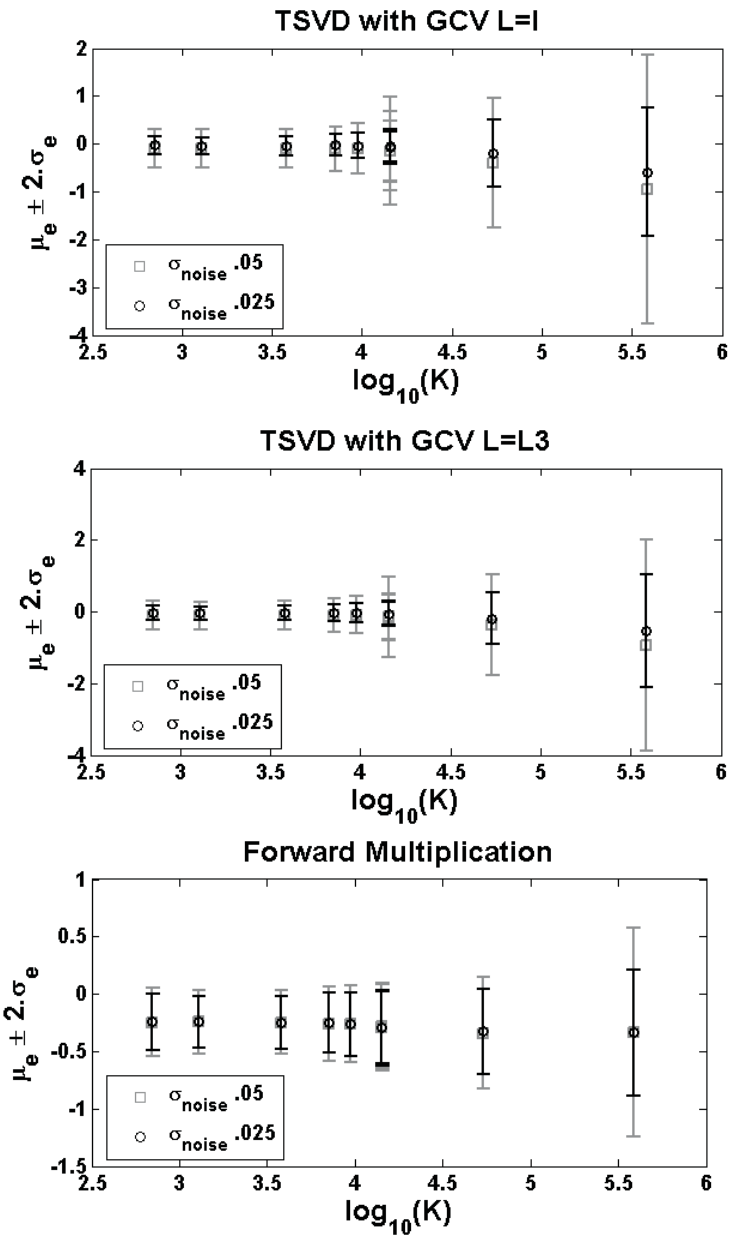

Figure 3.13: Average difference between the extracted and the real Q_{avg} if expressed in dB for the regenerator configurations listed in Table 3.6. The error flags are drawn at $\pm$ twice the standard deviation of the set of results. In the X-axis, the logarithms of the condition numbers are given.

the average deviation from the real Q_{avg}-values together with the corresponding error flags are depicted for the case 0.04 dB intervals were used and the noise vector had a standard deviation as mentioned in the legend. The error flags are drawn at $\pm$ twice the standard deviation of the set of results. We can clearly see the correlation between the obtained accuracy and the condition number, especially in the case of the regularization methods. In the case of the forward multiplication the dependence is somewhat less pronounced as compared to the two regularization approaches. Note also that conclusions about the trend of the quality in function of K are the most important to make, thereby ignoring small deviations into the 'wrong direction' (i.e. a slight increase in the quality of the result with increasing K). This can be simply caused by the fact a finite number of results is considered, thereby sometimes being influenced by only a few very bad results. However, the small differences between the standard deviations corresponding to different configurations that have equal condition numbers (i.e. the different entries for $log_{10}(K) = 4.15$) illustrate the significance of the considered set of signals. By comparing the results for the forward multiplication and the two regularization approaches in the case of the smallest noise additions, we see the occurrence of more accurate results for the regularization cases if well-conditioned transfers are used. This changes however rapidly, when the condition number increases. In that case the forward multiplication still renders acceptable results, whereas the regularization methods get very inaccurate. If we go even further, and increase the amplitude of the perturbation to .05 dB, we get better results with no matter which transfer in the case of the forward multiplication (cf. Fig. 3.13). Note that in the case the standard deviations get bigger, the degree of reliability gets smaller. This can be seen by the increased difference between different entries for the same condition numbers. Again this is caused by the presence of a few 'very' bad results.

As can be seen in Table 3.6 and by comparing Fig. 3.12(a) and Fig. 3.12(b), the condition number decreases by enlarging the interval width. It seems that the condition number corresponding to a certain non-linear configuration is proportional with the dimension of the system matrix. Care should however be taken in interpreting this decrease in condition number. By analyzing Fig. 3.14 it becomes clear that in the case of the forward multiplication approach this decrease in condition number can indeed be reflected in a slightly, more accurate Q_{avg}-extraction. However, only a very small difference is found. In the case of the regularization methods on the other hand the opposite

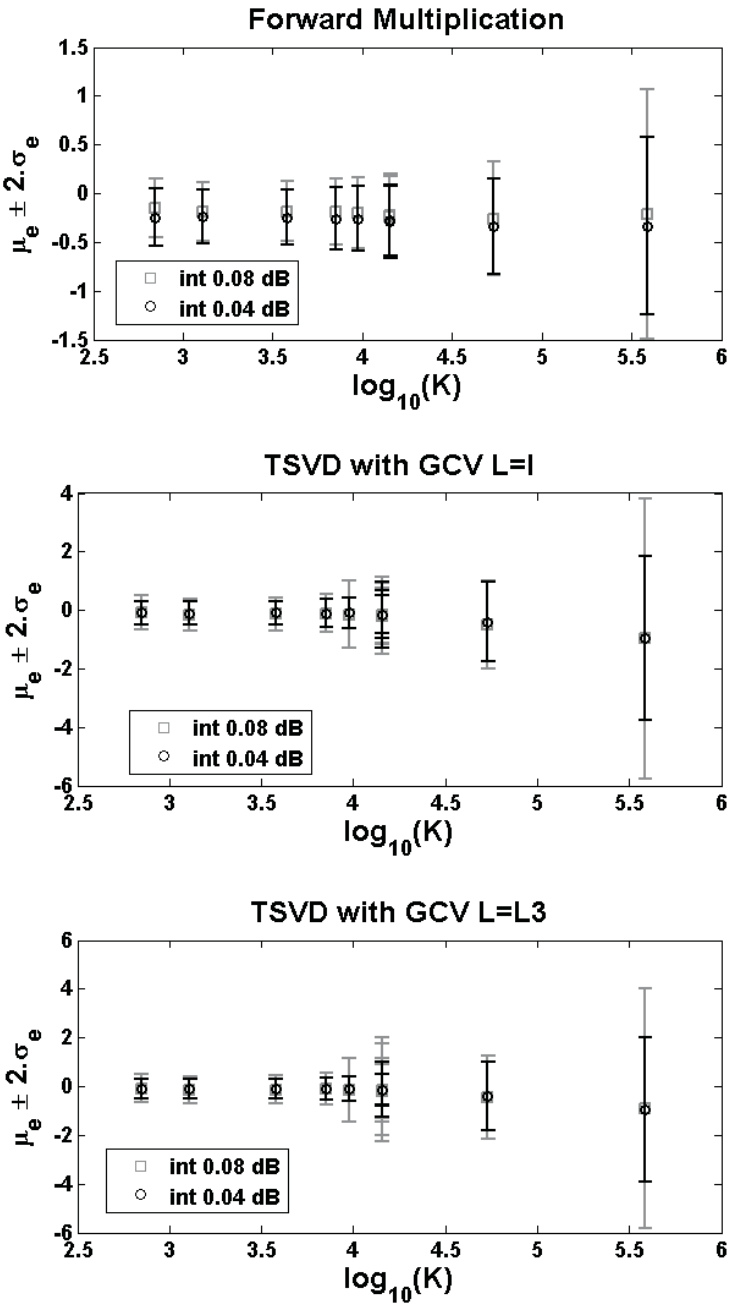

Figure 3.14: Same kind of results as in Fig. 3.13. Now, the results for two different interval widths are depicted. To allow comparison, both series are plotted in function of the condition numbers corresponding to the 0.04 dB intervals. A noise vector with a standard deviation of 0.05 dB is applied.

happens, i.e. a decrease of the extraction accuracy is observed in all studied cases. This indicates that the regularization methods get more profit out of the availability of extra measurement points as compared to the decrease of the conditioning degree. In the fitting approach on the other hand, it is more the per point perturbation that influences the final result. I.e. this approach sometimes gets already a slight advantage out of the averaging that takes place by only considering half of the measurement points.

As a conclusion we can state that the condition number is a useful tool for analyzing the feasibility of a given configuration. In addition it was illustrated that the forward multiplication approach can cope better with 'bad' transfers and noisy measurements as compared to the regularization methods. This is mainly due to the fact an initial shape is considered which resembles quite well with the actual histogram shape in the case of the noisy signals.
When comparing the condition numbers corresponding to system matrices of different dimensions, care should be taken.

3.7 In search for a practical implementation

From the previous "ideal case study", we concluded that the power transfer function of the non-linear component preferably should show a steep transition in combination with a large relative power jump. Therefore we looked deeper into some 2R regenerator configurations to check their feasibility, thereby taking into account **the theoretical as well as the practical limitations**. In other words, a configuration should be found that is mathematically feasible (reasonable condition number) and in addition enables a proof-of-principle experiment, i.e. a stable, easily reproducible power transfer should be provided. A short overview of the most important candidates considered during research will now be given in a chronological order, together with the justification of the choice of the regenerator configuration used for experimental verification.

3.7.1 Mach-Zehnder Interferometer (MZI) with two GCSOAs (MZI_GCSOA)

This component was developed in-house [68] and is based on the non-linear phase rotation of an optical signal during propagation through a GCSOA (Gain-Clamped Semiconductor Optical Amplifiers) [69]. The

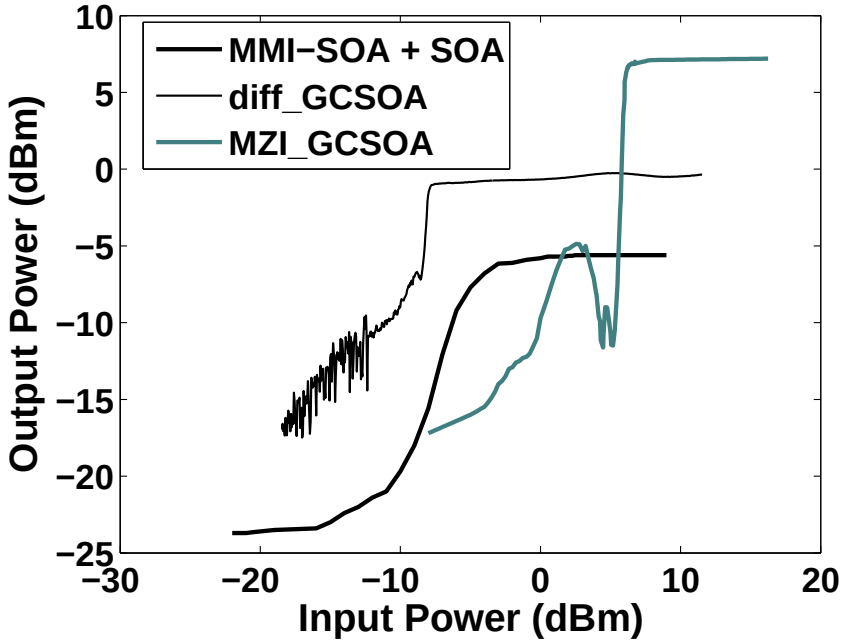

Figure 3.15: Experimentally obtained static regeneration curves corresponding to the configurations discussed in section 3.7.

working principle of the GCSOA will be explained in chapter 5, where a study of its behavior under small-signal optical modulation will be presented. An experimentally obtained static regeneration curve is depicted in Fig. 3.15. We immediately note the steep transition combined with the large relative jump (approximately 20 dB over a 1 dB input power range). This large jump is caused by the almost identical behavior of the two (identical, but slightly different biased) amplifiers at low optical input powers, resulting in an almost perfect destructive interference. Once both components are saturated, constructive interference takes place. For an in depth presentation of the static and dynamic properties we refer to [70].
Despite the interesting power transfer (cf. the small condition number in Table 3.3), the configuration could not be used in a practical monitoring setup since dynamical measurement were extremely difficult due to the fiber based interferometer present at our lab. Such a fiber interferometer is very vulnerable to environmental changes, such as tem-

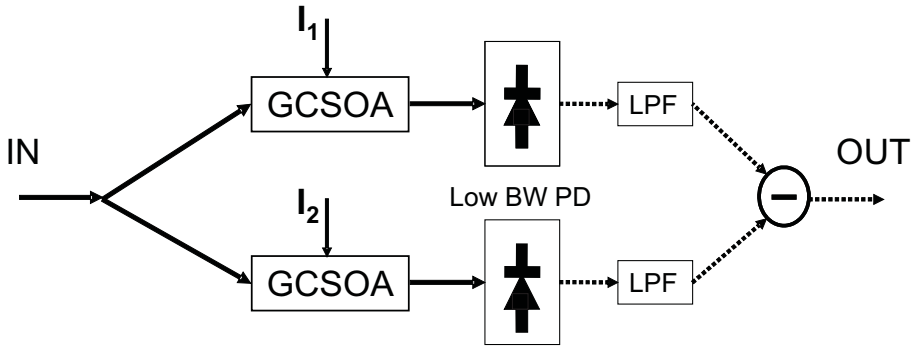

Figure 3.16: Schematic depiction of the non-linear configuration based on the difference in output power between two slightly different biased GCSOAs (diff_GCSOA). LPF: Low pass filter, low BW PD: Low bandwidth photodiode, I_1 and I_2: drive current of the GCSOAs.

perature, air displacement, etc. An integrated version could solve this problem, but was unfortunately not available.

3.7.2 Difference in optical output power of two differently biased GCSOAs (diff_GCSOA)

To overcome the practical difficulties encountered with the previous configuration, thereby hopefully enabling dynamical experiments, we came to the idea of using the difference of the optical output power of two differently biased GCSOAs (cf. Fig. 3.16). The advantage of this configuration is the independence of the power relation of an interference effect, thereby being less sensitive to environmental changes. In practice we used two times the same GCSOA driven with a different current. Fig. 3.15 depicts an experimentally obtained power transfer function corresponding to the difference in output power with the GCSOA biased at 145 and 125 mA respectively. The GCSOA used, was a packaged, commercial component supplied by Alcatel Optronics [71]. Note that for low power regions the output powers are almost equal, except for some difference caused by the non-linear gain suppression. Once both components are saturated, the difference remains almost constant. Note that the step height and steepness can be changed by adjusting the bias currents. A compromise should be found however. By properly choosing the currents, a transfer with a condition number comparable with the one obtained from the MZI_GCSOA configuration can be obtained (cf. Table 3.3).

	Interval width (dB)		
Configuration	**0.3**	**0.2**	**0.1**
MZI_GCSOA	2.32	2.9	3.5
diff_GCSOA	2.63	3.0	4.1
SOA/DFB	1.87	2.12	2.7
MMI-SOA + SOA	4.15	4.2	5.7

Table 3.3: For the different configurations, the logarithm of the condition number for an optimally chosen power span (i.e. with the lower edges in the vicinity of the threshold input power) of the system matrix corresponding to a power span of 10 dB divided into intervals with the respective interval widths.

It is interesting to note that the practical implementation proposed here is actually a combination of the two different approaches presented in section 3.1, i.e. the method with variable signal combined with the method with variable characteristic. Unfortunately it was exactly this last property that limited the stability, reproducibility and accuracy of the measurements. After several experiments the fact that the same signal had to be applied **at a different moment in time** to the same component driven by a different bias current, turned out to be the limiting factor of the configuration. We believe that the availability of 2 separate, identical GCSOAs and 2 optical power meters could solve this problem. In addition this would halve the measurement time.

It is important to note that not every good working 2R regenerator configuration is suited for our monitoring application. This can be seen by calculating the condition number corresponding to an experimentally obtained static power transfer from a regenerator consisting of an MZI with a Multi Mode Interference (MMI)-SOA and SOA combination [72] (cf. Fig. 3.15). In Table 3.3 we observe a difference of more than one order of magnitude, which will severely limit the tolerated perturbations.

3.7.3 Mutually coupled SOA/DFB laser combination

Finally we came to the idea of using a regeneration concept based on a combination of a DFB (Distributed FeedBack) laser diode and a SOA (Semiconductor Optical Amplifier) in an optical feedback scheme, as described in [74] and schematically depicted in Fig. 3.17. It has been demonstrated by simulations as well as by experiments that a very steep transition in the signal output power ($P_{sig,out}$) in function of the

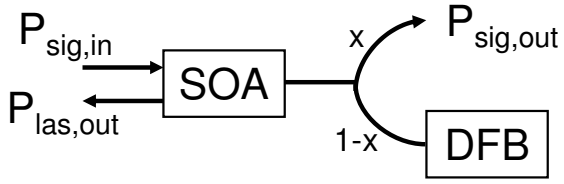

Figure 3.17: Principal scheme of the regenerator based on the DFB/SOA combination. $P_{las,out}$ is the output power used in our simulations and experiments.

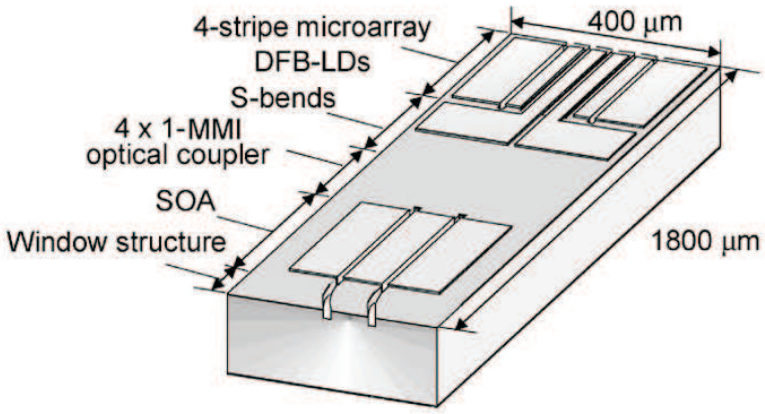

Figure 3.18: Schematic view of the wavelength selectable source presented in [73] used for the first monitoring experiments. ©IEEE

signal power injected into the SOA ($P_{sig,in}$) can be achieved if the currents of both components are chosen properly. This sharp transition in the input-output power relation is caused by an abrupt change from a regime in which the SOA is saturated by the laser light injected from the right hand side, to a regime in which the SOA is saturated by the signal light injected from the left hand side. This is accompanied by a change of the spatial hole burning (longitudinal carrier distribution) in the SOA. Due to the fact that the SOA is saturated at every moment (either by the signal power or by the laser power), high speed operation can be achieved if care is taken that the laser never completely switches off, thereby avoiding relaxation oscillations [75].
Observation of the laser power coming out of the SOA ($P_{las,out}$) revealed an even higher relative power step. I.e. due to the feedback

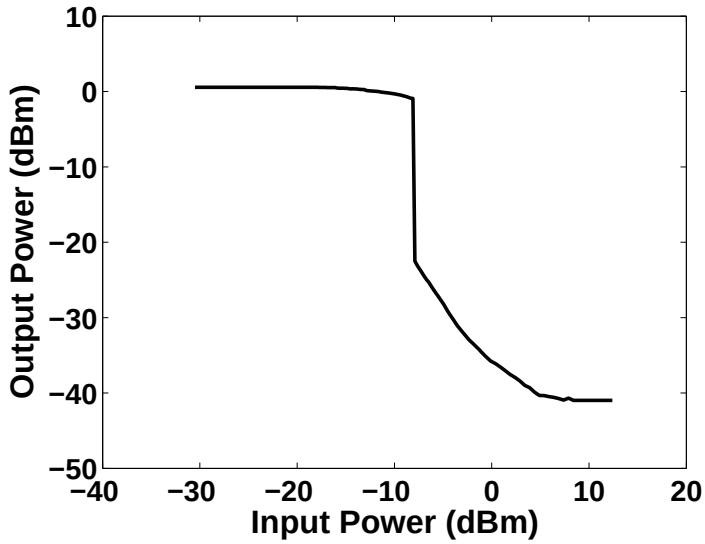

Figure 3.19: Experimentally obtained static regeneration curve corresponding to the SOA/DFB combination discussed in section 3.7.3 and depicted in Fig. 3.18.

scheme, an extremely sharp cut-off behavior of the DFB laser could be achieved. In some cases this cut-off behavior showed some hysteresis in function of the input power, but by adjusting the current combinations this could be brought to a negligible level.

It is now this steep transition of the laser power in function of the signal input power that will be **used during the rest of this work**. Next to the attractive power transfer, also the fact that this is achieved by using a single integrated component of which the working principle is not depending on any interference effect made it a potential candidate for the intended purpose.

The first experiments making use of this component were performed using a wavelength-selectable laser diode [73], delivered to us by NEC Corporation. It consisted of a DFB array of 4 laser diodes fed to a single SOA after passive combination by a 4x1 MMI-coupler. An illustration is given in Fig. 3.18. The component was delivered to us on a naked chip. An experimentally obtained static laser power transfer is depicted in Fig. 3.19. Note the small condition numbers that are achieved as denoted in Table 3.3. As will be explained in the next chapter, this component could not be used for the dynamic experiments. However, we

have used this power transfer for the simulations presented in the next section.

3.8 Case study: SOA/DFB combination

From the previous section, it became clear that the regenerator consisting out of a SOA/DFB laser combination in an optical feedback scheme was the most suitable candidate for a practical implementation of the proposed monitoring scheme at our laboratory. Therefore, some more in depth simulations were performed using an experimentally obtained static transfer curve (Fig. 3.19) in order to get a view on the feasibility of a proof of principle experiment.

Minimization of the condition number revealed a $log_{10}(K)$=4.15 and 3.54 for 0.02 and 0.04 dB intervals respectively. Those numbers seem reasonable, if compared with the different entries of Fig. 3.14. In Fig. 3.20 results are given for the two forward multiplication approaches presented in section 3.4.2 and for 2 regularization methods (TSVD combined with GCV, with resp. L=I and L=L3). The results are depicted as the mean deviation between the extracted and the real Q_{avg}value if expressed in dB, together with the corresponding error flags. Those error flags should be interpreted as: "the probability that the extracted Q_{avg} lies within the interval spanned by the two errorflags is 95% in the case the solutions are normally distributed". The results were calculated from a set of 260 signals (130 of the noisy type and 130 of the distorted type). Noise additions were done on a logarithmic scale with the standard deviations as given in the legend.

At a first glance we note that it will not be easy at all to obtain very accurate Q_{avg}-estimates. In the case of the noisy signals, the forward multiplication approach using two Gaussian distributions results in the most accurate results. Even for the higher noise addition, still accurate results can be obtained by this approach. In the case of the distorted signals however, this does not work any more due to the bad resemblance between the objective function and the real histogram shape. The results were that bad, they were left out of the figure to enhance the visibility of the other (useful) results. A significant underestimation was achieved in any case, due to the presence of the large amount of cross-point data.

The partial fitting approach rendered reasonable results for both types of signals, be it less accurate as compared to the previous fitting approach in the case of the noisy signals. The obtained results showed

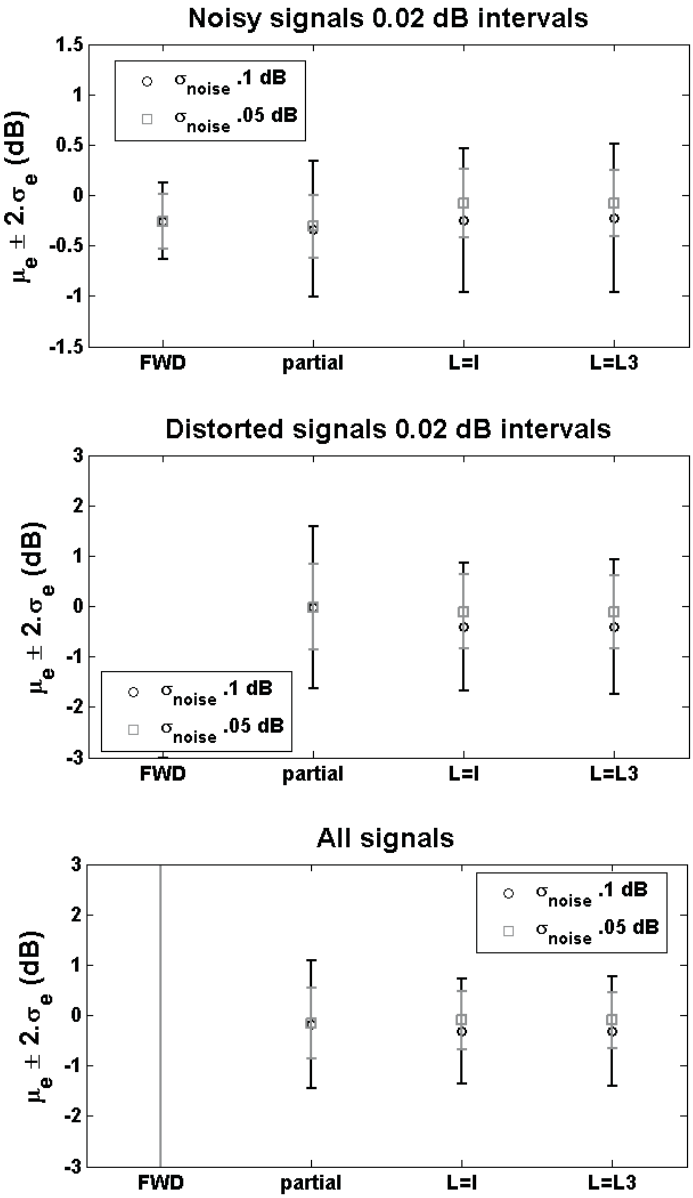

Figure 3.20: The average deviations of the extracted Q_{avg}-values are depicted together with the corresponding error flags. The transfer from Fig. 3.19 was used. A 20 dB wide power span was considered, divided into intervals of 0.02 dB. The results of 4 methods are depicted, FWD and partial are the two fitting approaches of section 3.4.2, whereas $L = I$ and $L = L3$ represent the TSVD regularization method using GCV and the respective smoothness operators.

the same degree of accuracy as the tested regularization methods. For the smallest noise addition the deviations seem to be tolerable, whereas for the second noise addition, a high loss of accuracy is observed. An important note is that the computational time needed for the partial fitting is significantly higher as compared to the regularization methods. Therefore, if the only goal is to extract Q_{avg}, the partial fitting occurs to be less interesting.

For the case of the .04 dB intervals, the results showed exactly the same trends. They were in any case a little bit less accurate. The difference was however not very big (a maximal increase of standard deviation of .18 dB as compared to the 0.02 dB intervals was found). So the slight improvement we noticed in the quality of the results obtained by the forward multiplication approach during the study of the ideal curves is not observed here.

In general we observe that the methods have **more difficulties to deal with the distorted signals** as compared to the signals only perturbed by noise. For the fitting approaches this is quite obvious, since in both the partial and the Gaussian fitting case the resemblance between objective function and original histogram shape is much better for the noise signals as compared to the distorted signals.
For the regularization methods, on the other hand it was found that the norm of the relative error was bigger in the case of the distorted signals than for the noisy signals,whereas for both types of signals the relative norm of the initial error and of the system matrix are equal. The regularization methods as such are therefore better suited for the noisy signals. Probably, an adjustment of the smoothness operator can help in improving the results for the distorted signals. This however undermines again the transparency of the method.

Important to mention is that a bad approximation of the Q_{avg} corresponding to a data signal does not necessarily implies a complete useless solution. This is illustrated in Fig. 3.21. In this example, both the partial fitting approach and the regularization with L=L3 deliver Q_{avg} estimates with an inaccuracy of more than 1 dB. Analyzing the shape of the results does however still allow distinguishing between the possible sources of degradation. This can be concluded out of the plateau that is clearly present between the two peaks in the case of the distorted signal. In the case of the regularized solution, this can be concluded out of a smoothed version of the cross-point data. Thus, if an inaccurate estimation of the quality parameter is obtained, the histogram can still

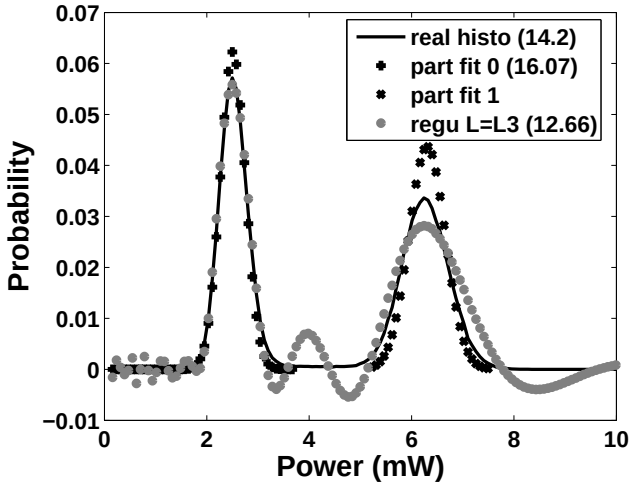

(a) Noisy signal

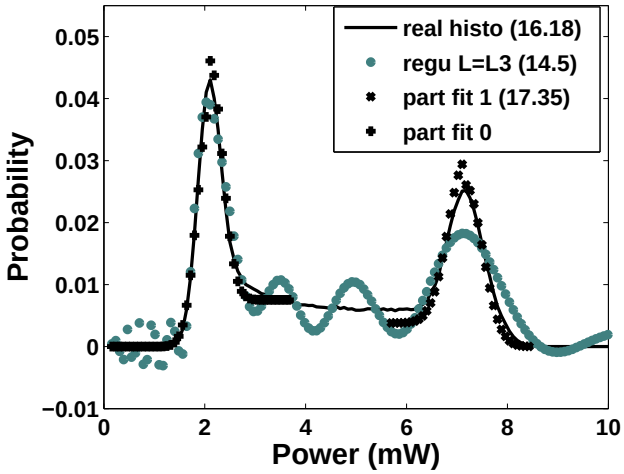

(b) Distorted signal

Figure 3.21: Illustration of two inaccurate solutions with respect to the Q_{avg}-estimation (Q's expressed in dB are given in the legend). The results correspond to a mean power vector to which a noise vector with a standard deviation of .3 dB is added. This illustrates that still information concerning the main source of degradation can be extracted.

contain information about the main source of degradation, which is an interesting property for an optical performance monitoring application.

3.9 Conclusion

A thorough theoretical study of the introduced asynchronous signal histogram construction method was presented. The method is based on the analysis of the change of the average optical output power of a non-linear optical component, to which subsequently altered versions of the original data signal are applied. This results in a linear system of equations containing the histogram probabilities as unknowns. Several approaches to solve the ill-conditioned system were investigated. It turned out that some a priori assumptions considering the shape of the histogram could be very advantageous concerning the achievable extraction accuracy. I.e. by limiting the set of solutions to a predefined histogram shape, the difficult and inaccurate inversion of the ill-conditioned system matrix can be avoided.
Mathematical regularization methods did however also deliver useful information, be it slightly less accurate, but of course being more transparent, since no a priori information had to be included.

A first indication of the feasibility of a given non-linear component could be found in the minimal condition number corresponding with the system matrix constructed from the static power transfer function. Practical issues such as the dynamic behavior, stability, reproducibility, etc. of the configuration have also to be considered as very important, since the histogram extraction turned out to be vulnerable to small deviations of the measurements of the assumed behavior.

A search for a decent configuration, which allows experimental verification at our laboratory, brought us to a 2R regenerator based on a DFB laser diode and a SOA in an optical feedback scheme. A theoretical study showed that experimental verification should be possible if care is taken concerning the practical implementation. This experimental verification will be presented in the next section.

Chapter 4

Experimental verification of monitoring method

4.1 Introduction

As was explained in the previous chapter, several practical regenerator configurations were taken under consideration as a key building block for the proposed monitoring method. This investigation brought us to a 2R regenerator consisting of a SOA/DFB laser diode combination in an optical feedback scheme presented in [74] as being the best candidate available at our laboratory. An extreme sharp transition could be achieved in the output laser power as function of the signal input power (cf. Fig. 3.19).

As was explained, in order to obtain a reasonable estimation of the average Q-factor out of the extracted asynchronous histogram, a very accurate mean power vector has to be measured. This accuracy will be influenced by numerous factors, a.o. stability of the configuration, noise sources present in the setup, resemblance between the behavior of the non-linear component under static and dynamic conditions, etc. It turned out that in a first series of experiments, the stability and reproducibility of the measurement setup/regenerator combination actually were the limiting factors to achieve reasonable results. For the different regenerators used in the experiments, it was explained in section 3.7 what the main reason for failure was.

The SOA/DFB combination delivered to us by NEC (cf. section 3.7.3 and Fig. 3.18) at first sight showed a very attractive performance, but did however suffer from some disadvantages with respect to long term stability. Since this component was mounted on a naked chip,

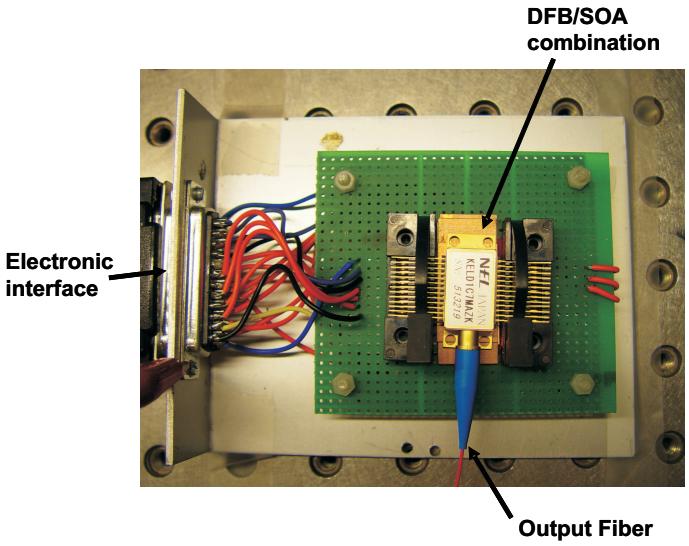

Figure 4.1: A picture of the packaged 2R regenerator used for the dynamical experiments.

the optical signal had to be coupled into the component using a lensed fiber mounted on a translation stage. This made the coupling very sensitive to a.o. environmental changes. Since the transition taking place in the output laser power was extremely sharp, a small change in coupling efficiency could result in a significant change of the behavior of the component. Therefore it was very difficult to construct a correct system matrix. Also the fact that currents had to be applied via probes, combined with the high dependence of the non-linearity on the actual current settings, turned out to be a limiting factor. The techniques of lensed fibers and probes are commonly used in measurement setups, but it is exactly the high demand of long term stability, combined with the high sensitivity of the component to changes in input optical power and current that made them infeasible for our application.

By using a packaged version of the component, we could significantly reduce the influence of the mentioned disadvantages. Therefore, a customized version of a wide-band wavelength tunable laser array consisting of 12 DFB lasers coupled to an integrated SOA was ordered, similar to the one presented in [76]. The customization consisted out of the removal of the isolator present in the commercial component, since this would not allow power injection. A picture of the component is shown in Fig. 4.1. Using this device it was again possible to obtain the

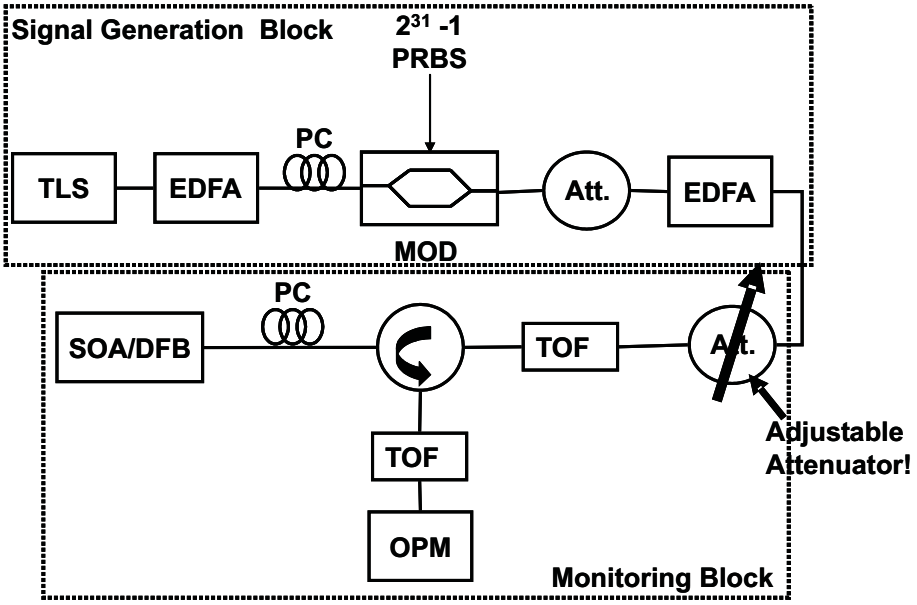

Figure 4.2: Schematical overview of the setup used for the dynamical measurements. TLS: Tunable light source, EDFA: Erbium Doped Fiber Amplifier, PC: Polarization Control, MOD: High speed optical modulator, Att.: Attenuator, TOF: Tunable optical filter, SOA/DFB: used regenerator configuration (Fig. 4.1), OPM: Optical power meter, PRBS: Pseudo-Random Bit Sequence electrical data signal.

sharp cut-off behavior of the laser diode in function of the input power, but in addition a **much more stable and reproducible** behavior could be achieved. The only disadvantage as compared to the naked NEC chip was the fact that due to the low coupling between the laser diodes and the SOA ($<$ 10% versus 25% for the NEC component), different lasers had to be turned on simultaneously in order to virtually increase the coupling between SOA and lasers, thereby enabling the sharp transition in the laser power. Moreover, the lasers could only be biased slightly above threshold. This resulted in a dynamical behavior which was less attractive and in addition less predictable due to the unknown interaction occurring between the different lasers. However, the experiments resulted in much more useful quality information as compared to the previous attempts.

4.2 Measurement setup

To perform dynamical experiments, a setup as schematically depicted in Fig. 4.2 was used. Roughly spoken it consisted out of two parts, i.e. the part responsible for the generation of a data signal with varying signal quality on one hand and the part representing the monitoring equipment on the other hand.

The data signal was generated using a tunable laser source, followed by an attenuator/EDFA (Erbium Doped Fiber Amplifier) combination, a polarization controller and an optical modulator with a modulation bandwidth of approximately 13 GHz. The modulator was driven by a $2^{31}-1$ electrical PRBS (Pseudo Random Bit Sequence) signal generated by a pattern generator driven with a clock signal with adjustable repetition rate. The modulator also had a DC electrical input to adjust the output extinction ratio. The polarization controller was indispensable since the modulator was highly polarization dependent. The attenuator/EDFA combination following the modulator was only needed to compensate for the loss of the modulator, in the case a high input power was needed to achieve the non-linear power transition. In the case of the packaged component this was actually not necessary due to the only weakly biased lasers, resulting in a small input threshold power of the non-linear characteristic.
The described setup enabled **the generation of Non Return to Zero (NRZ) signals with an adjustable signal-to-noise-ratio (SNR) and extinction ratio (ER)**.

The monitoring block consisted of a high precision adjustable attenuator, followed by a circulator guiding the signal light to the regenerator and guiding the counterpropagating light to an optical power meter. The signal was filtered before entering the component by a 0.6 nm wide optical filter, whereas the laser signal was selected by an even smaller filter (0.3 nm) before the detection by the optical power meter.The attenuator has to be very precisely adjustable, preferably via remote operation. The attenuator was set by a PC, which also collected the measured optical power from the optical power meter. All this was coordinated by a Labview program.

In order to obtain the real asynchronous signal histogram, a 30 GHz optical oscilloscope was connected to the output of the 0.6 nm optical filter. Afterwards, the extraction of the histogram and corresponding quality parameters out of the measured mean power vector was performed by some Matlab programs.

4.3 Results and discussion

The numerous experiments performed in order to get a proof of the monitoring principle presented in this work revealed that several factors make an accurate averaged Q-factor estimation extremely difficult.
First of all, there is the compromise that has to be made between the steepness of the curve and the resemblance between static and dynamic behavior. Of course we want both of them to be optimal, since a decrease of steepness does severely limit the tolerated perturbations in a pure mathematical way. On the other hand, it is intuitively clear that a very steep static regeneration curve will be a lot harder to be followed perfectly once a dynamic signal is applied. This is certainly the case when using semiconductor based devices of which the working principle is based on the depletion of carriers, since they suffer from patterning effects. It is worth mentioning that non-linear components based on the ultra-fast Kerr effect could probably solve this problem. The bit rate dependency of the behavior of the regenerators used in our experiments manifested itself as a flattening of the measured mean power vector when increasing the bit rate of the data signal. This resulted in a gradual disappearance of the two distinctive transitions, corresponding to respectively the zeros and the ones in the mean power vector.
In addition, a stringent requirement is put on the all-over stability of the configuration. A stable environment is necessary, together with a setup showing almost no reflections, a negligible polarization dependence, etc. Those requirements can be fulfilled by carefully constructing the measurement setup and especially carefully choosing the non-linear component. Doing this, resulted in extracted information that probably fell short of expectations of obtaining very accurate estimations, but **did certainly contain useful information** with respect to the detection of severe degradations occurring in a data link.

Fig. 4.3(a) demonstrates that in some cases rather good estimations could be obtained. The figure contains histograms extracted from the mean power vector depicted in Fig. 4.3(b), measured with an attenuation increment of 0.02 dB. Both the forward multiplication approach using two Gaussian distributions and the regularization approach resulted in histograms corresponding quite well to the original, apart from a slight underestimation of the extinction ratio. The signal studied was a 100 Mb/s NRZ signal. Note also the two dips present in the mean power vector corresponding to the zero and the one transition. Their visibility is however not that good since for this experiment only

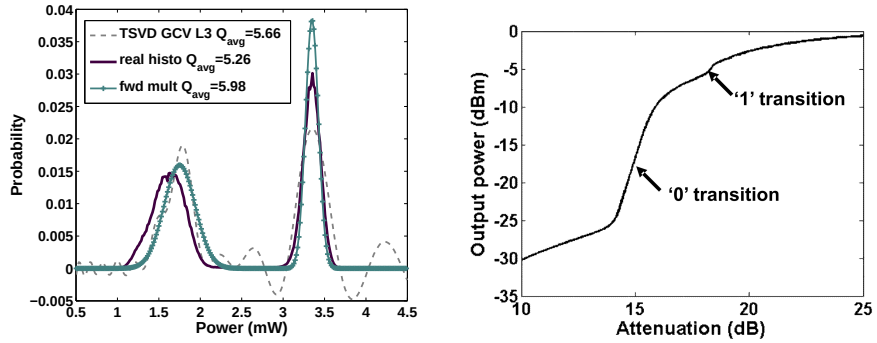

(a) (b)

Figure 4.3: (a) depicts an example of a histogram obtained from the mean power vector depicted in Fig. (b) corresponding to a 100 Mb/s signal and an interval width of 0.02 dB. The results obtained by both the forward multiplication using 2 Gaussian distributions and the regularization approach using L=L3 are given.

one laser was biased, rendering a less steep static transfer function. From the obtained smoothness of the experimentally obtained mean power vector two things can however be concluded. First of all it is demonstrated that indeed very small "noise"additions are present, as assumed in the simulations. Thereby, the modeling of the measurement perturbations as a normally distributed power addition on dB-scale with only a small standard deviation is justified. On the other hand, we have to conclude that the difference between the measurement results and the expected is caused by a deviation from the assumed static power relation under dynamic conditions, and not by the only small addition.

An important remark to make is that although good approximations could be achieved in certain cases, it was rather difficult to find a consistent relation between the extracted and the real histograms. One thing could however certainly be concluded. I.e. if we gradually applied a more and more polluted signal, this trend could also be found in the extracted quality parameters. An example of this statement is illustrated by the results depicted in Fig. 4.4. The figure contains the Q_{avg} and extinction ratio as obtained from the monitoring experiment performed for a 100 Mb/s signal of which the quality was gradually modified by changing the DC voltage supplied to the optical modulator. This resulted in an increase of the extinction ratio, accompanied

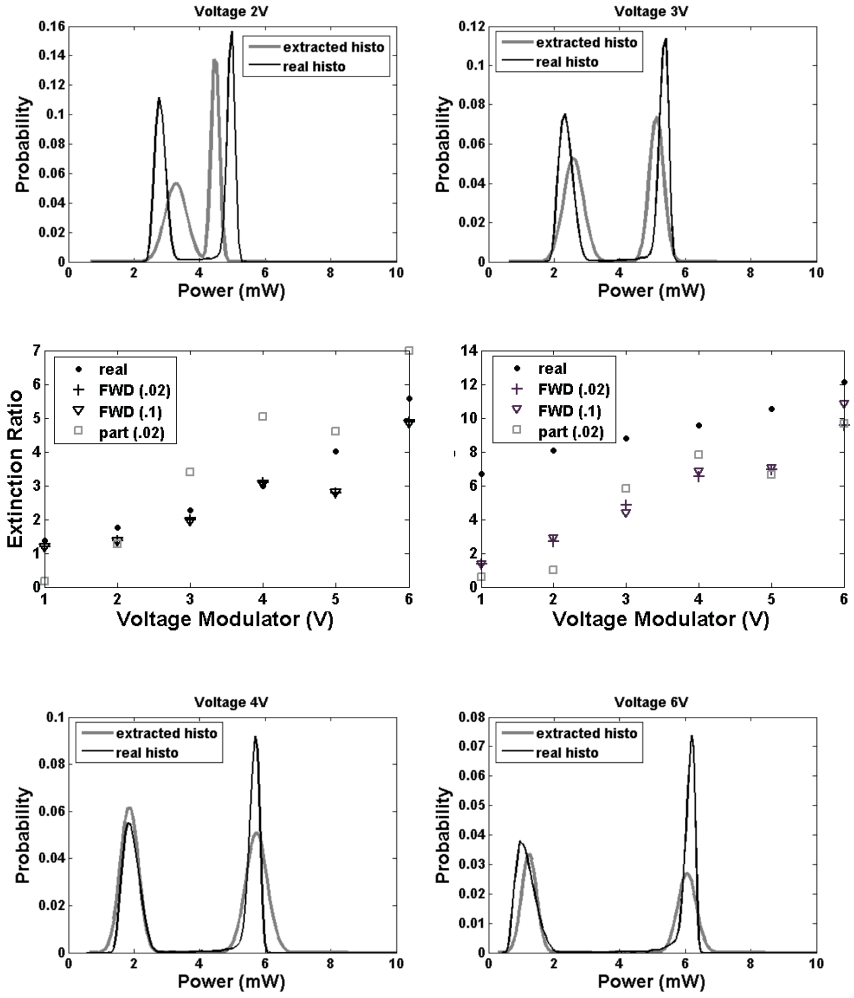

Figure 4.4: Overview of results obtained with the static regeneration curve of Fig. 4.5 corresponding to a 100 Mb/s signal with varying signal quality. In the central figures, the Q_{avg} and ER values as obtained by the two fitting approaches are given. The used interval width are given in the legend. (FWD: 2 Gaussian approach, part: partial fitting approach)

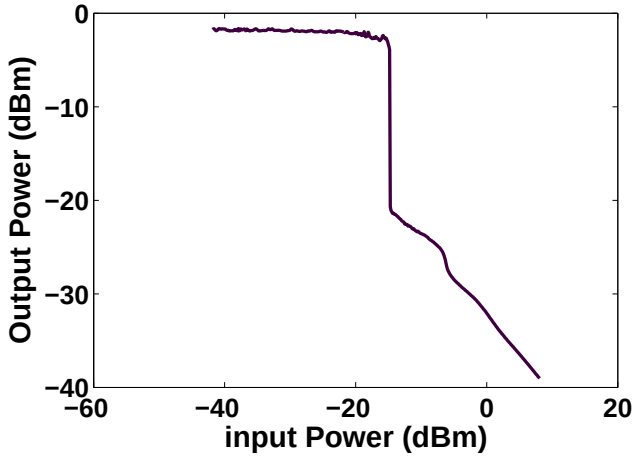

Figure 4.5: static regeneration curve of the NEL component used for the dynamical experiments of Fig. 4.4.

by a Q-factor increase. The static transfer function as depicted in Fig. 4.5 was used and average power measurements were performed with an increment of the attenuation of 0.02 dB. For the results obtained by the forward multiplication using 2 Gaussian distributions, two things can be concluded that are representative for all the measurements performed. The extinction ratio could be extracted rather accurate (except for one single entry) in almost every case. This is intuitively clear, since this is actually only dependent on the average power of the ones and zeros separately. This means that as long as the regenerator used can follow the data signal in a decent way, an influence will be found in the average output power at the moment the ones, respectively the zeros cross the non-linear transition. The widths of the peaks in the histogram are much more difficult to extract correctly, since the reaction of the component on the noise components is rather frequency dependent. Therefore, the deviation between the static and the dynamic behavior of a given non-linear component will be first manifested in the extraction of inaccurate standard deviations of the peaks corresponding to marks and spaces.

In Fig. 4.4 also the extracted parameters corresponding to intervals of 0.1 dB width are depicted, as obtained with the forward multiplication approach using two Gaussian distributions. We note that almost no difference occurs. Therefore this is even more interesting since this reduces the measurement time to a fifth of the previous. In addition

this also relaxes the requirements put on the accuracy of the attenuator used in the monitoring block.

Fig. 4.4 also contains the results obtained by the partial fitting approach. We note that also those results clearly show the trend of the change in signal quality, however less accurate as compared to the other fitting approach (especially the extracted ER is less consistent). This is in accordance to the conclusions made out of the simulations of the previous chapter (cf. section 3.8).

We have to mention that in the experiments, only the forward multiplication approaches resulted in decent histograms in all cases. The regularization approach did fail sometimes, therefore not resulting in consistent results in all cases. In most of the cases, solutions exhibiting high-frequency components were found, showing a clear under-regularized behavior. This is probably caused by the bigger robustness of the fitting approaches to variations in the averaged power vector, but even more on variations in the assumed system matrix.

4.4 Conclusion

As a conclusion we can state that accurate parameter extraction in any given case was not achieved experimentally. It was however demonstrated experimentally at a rather low bit rate of 100 Mb/s that it is indeed possible in some cases. A consistent relation between the trend of the real signal quality and the extracted Q_{avg} could be found. I.e. **a gradual degradation of a data signal could certainly be detected**. In addition in most of the cases, a rather good estimation of the extinction ratio could be achieved by the method using the forward multiplication by two Gaussian distributions. In general, the results obtained by the two fitting approaches showed the highest robustness to the practical inaccuracies.

Chapter 5

Small-signal analysis of gain clamped semiconductor optical amplifiers

In the study of the monitoring method presented in the previous chapters, different types of semiconductor optical amplifiers played an important role. This is confirmed by noting that all the regenerator configurations considered as potential candidates for the monitoring application used some kind of SOA (cf. section 3.7). Therefore a good understanding of the dynamics of such components was not without merit.

Originally, a lot of attention was paid to a 2R regenerator on the basis of gain-clamped SOAs ([37], [68]). Therefore, two types of gain-clamped SOAs (LOA and GCSOA) were studied under small-signal optical modulation conditions. We will start with a brief overview of the literature on the dynamics of the given components, and briefly explain the difference between both components. The time domain model developed for the simulation of the LOA will be explained. The biggest part of the chapter will obviously be devoted to the in depth theoretical and experimental investigation of the behavior of the LOA and GCSOA under small-signal optical modulation. The structure of this chapter is based in great extent on the publication of our results in [77].

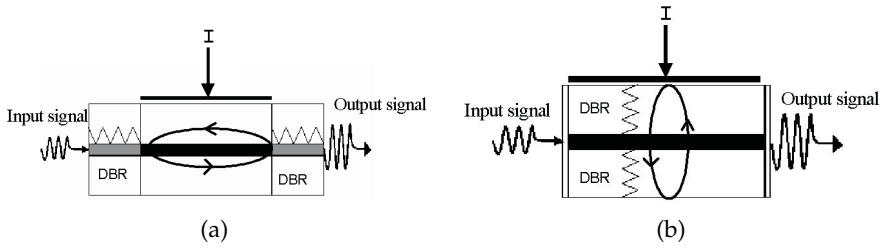

Figure 5.1: Schematic structure of the two types of gain clamped SOAs. GCSOA (a) and LOA (b).

5.1 Introduction

In order to suppress signal induced gain fluctuations of SOAs in WDM systems when using intensity modulated signals, up till now two types of linear optical amplifiers were developed as alternative for the well-known classical traveling wave SOA. In the middle of the nineties, this was achieved by the so-called GCSOA (Gain Clamped Semiconductor Optical Amplifier) [69]. This component is in fact a semiconductor optical amplifier in which a longitudinal laser cavity is incorporated. It basically consists of an active region, surrounded by two distributed Bragg reflector (DBR) sections. The structure is schematically depicted in Fig. 5.1(a). The GCSOA operates based on the gain clamping by laser oscillation and thereby provides a constant gain independent of injected current and input optical power (up to the input saturation power) if the signal wavelength is chosen sufficiently far from the lasing wavelength .
The second approach used to reduce the interchannel crosstalk was introduced in 2001 and is called the Linear Optical Amplifier (LOA) [78]. Now a vertical laser cavity is used to clamp the gain (cf. Fig. 5.1(b)). The vertical cavity further reduces the transient fluctuations present in the signal gain caused by input power variations. This is due to the more effective capture of the input power variation by the laser power [79]. Both types of components proved already their potential in several high-speed applications both using the linear (e.g. [69], [80], [81] and [82]) and the non-linear properties (e.g. [68], [83] and [84]).

To our knowledge, only few studies have been presented concerning the dynamic behavior of the GCSOA under small-signal optical modulation. In [85] a small signal model was proposed and used to explain a resonance phenomenon in the crosstalk. In the case of semi-

conductor lasers, several experimental approaches to determine intrinsic parameters using small-signal optical modulation techniques were presented [86]. Thereby the parasitic-free modulation response of a laser diode can be obtained, as contrary to the electrical modulation approach. Also the suitability of the component for CATV networks has been studied previously theoretically as well as experimentally [80]. Thorough co- and counter propagating crosstalk measurements were however not yet performed.
For the LOA, a resonance behavior was observed in the output of a small-signal model for a co-propagating probe signal [87]. This was confirmed by a few experiments in [88]. The crosstalk under large signal modulation on the other hand was briefly studied in [79]. All this illustrates that up till now **no systematic or in-depth investigation of the complex small-signal dynamics of both GCSOAs and LOAs has been reported**.

In this chapter, the crosstalk occurring in both types of amplifiers in two different injection schemes will be investigated by simulations, and by experiments. Also the effect the gain modulations have on the amplification of the RF input signal will be discussed. We believe those studies can help in the further understanding of the dynamical behavior of the given components.

5.2 Simulation tools

Since the LOA was a rather new component, a simulation model was developed in order to make extensive numerical investigation possible. The model is a one dimensional rate equation model based on the models presented in [79] and [89]. It is described by the following equations:

$$\begin{aligned}\frac{\partial N(z,t)}{\partial t} = &\frac{1}{q}.\frac{I}{w.d.L} - A.N(z,t) - B.N^2(z,t) - C.N^3(z,t) \\ &- \frac{\Gamma_{sig}.g(z,t)}{w.d}.\sum_i \frac{1}{h.\nu_i}.P_i^{\pm} - \frac{\Gamma_L.g(z,t)}{w.L}.\frac{1}{h.\nu_L}.P_L\end{aligned} \tag{5.1}$$

$$\frac{1}{v_g}.\frac{\partial P_i^{\pm}(z,t)}{\partial t} \pm \frac{\partial P_i^{\pm}(z,t)}{\partial z} = \left(\Gamma_{sig}.g(z,t) - \alpha_{\text{int}}\right).P_i^{\pm}(z,t) \tag{5.2}$$

$$\begin{aligned}\frac{\partial P_L(z,t)}{\partial t} = &\left(\Gamma_L.g(z,t).v_g - \frac{1}{\tau_{ph}}\right).P_L(z,t) \\ &+ \beta.V_{act}.B.N^2(z,t).\frac{v_g}{2.L}.h.\nu_L\end{aligned} \tag{5.3}$$

with

$$g(z,t) = a.(N(z,t) - N_0).\left(1 - \varepsilon_{sig}.\Gamma_{sig}.P_{sig}(z,t) - \varepsilon_{sig}.\frac{d}{L}.\Gamma_L.P_L(z,t)\right) \quad (5.4)$$

N(z,t) denotes the carrier density in the active layer at position z on time t. P_L stands for the laser power, whereas P_i^+ and P_i^- represent respectively the forward and backward propagating signal at frequency ν_i. The other symbols used in the equations are explained in Table 5.1, together with the typical values used in the simulations [90].

The specific structure of the LOA is reflected in a separate laser equation (Eq. 5.3) for each segment along the component. This segmental approach (segments of approximately 10 μm) enabled modeling of effects caused by the longitudinal spatial hole burning, which will be very important. A wavelength independent gain model was used, including the ultra-fast non-linear gain suppression mainly caused by carrier heating and spectral hole burning [91]. Random noise sources were not included, since they were not relevant in our study. Signals could be injected at both sides of the component.

For the modeling of the GCSOA, an in-house developed computer model called CLADISS could be used [93]. This is a longitudinal multimodal model for the analysis of the static, dynamic and stochastic regime of laser diodes with distributed feedback. An extension to model amplifiers was available, offering the possibility of injecting signals at both facets. The material parameters were chosen as in [94]. The dimensions together with the gain suppression factor are given in Table 5.2. Note that the gain suppression factors of GCSOA and LOA are identical if expressed in cm^3 (i.e. 8.8x10^{-18} cm^3).

5.3 Small-signal amplification under CW injection

Two different injection schemes were studied, namely the co- respectively counter-propagating setup. In the **co-propagating** case, we injected a CW signal at the left side of the component, on which a RF sinusoidal component with an amplitude equal to 10% of the CW power was superposed. In the **counter-propagating** setup on the other hand, a raised sinusoidal RF signal was injected on the right hand side of the component at the same wavelength of the CW signal, which was still injected on the left side. In a first study, we checked the amplitude of the sinusoidal component in both configurations, when leaving the

Parameter	Value	Description
τ_{ph}	10^{-12} s	Photon lifetime [89]
A	1.66x10^{8} s^{-1}	Nonradiative recomb. const.
B	10^{-10} cm^3s^{-1}	Bimolecular recomb. const.
C	3x10^{-29} cm^6s^{-1}	Auger recomb. const.
d	.2 μm	Active layer thickness
w	1 μm	Active layer width
L	1200 μm	LOA length
Γ_{sig}	.45	Confinement factor signal
Γ_L	.65	Confinement factor laser light
α_{int}	26.8 cm^{-1}	Effective loss coeff.
β_{sp}	1x10^{-4}	SE coupling coeff.
N_0	1x$10^{18}cm^{-3}$	Transparency carrier density
a	2.7x$10^{-16}cm^2$	Differential gain coeff.
ν_{sig}	193.55 THz	Signal frequency
ν_L	192 THz	Laser frequency
v_g	8.33x$10^{7}ms^{-1}$	Group velocity
ε_{sig}	3.885 W^{-1}	Gain suppression coeff. [92]
I	$175mA$	Injected current

Table 5.1: Physical parameters of the LOA used in the simulations. SE: Spontaneous Emission, recomb.: recombination

amplifier. The so-called small-signal gain is defined as the ratio of this amplitude to the amplitude of the RF component at the input of the device. The dependence of this gain on the CW input power and the RF frequency was investigated.

5.3.1 Simulations

Fig. 5.2(a) depicts the simulated small-signal gain as obtained for a GCSOA driven with a current of 120 mA for different CW input powers. We clearly observe several regimes, depending on the degree of saturation. At low input powers, as compared to the input saturation power which is approximately -4.5 dBm, a fairly frequency independent amplification is obtained. The gain remains clamped to the CW gain under all excitation frequencies. A look into the component showed that for all frequencies, apart from a little spatial hole burning in the front and the back of the amplifier, the gain is equal along the entire length of the GCSOA. At input powers in the vicinity of, but

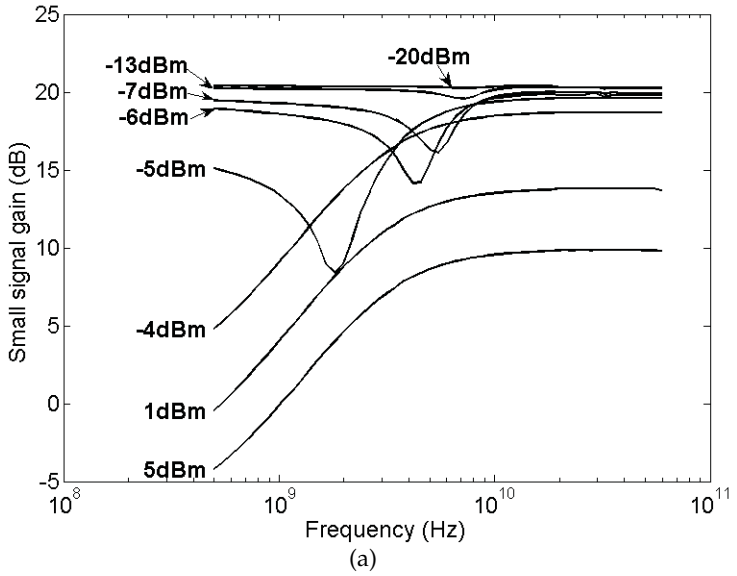

(a)

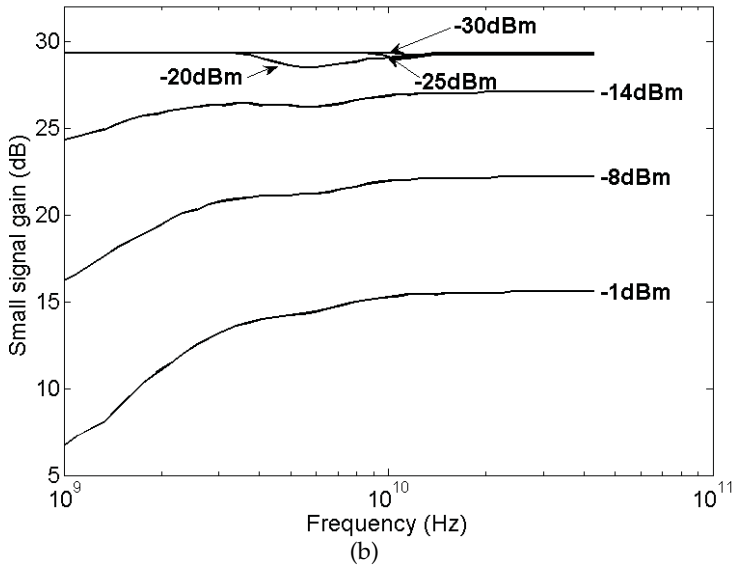

(b)

Figure 5.2: Small-signal gain in the co-propagation regime for different CW input powers resulting from the simulation of a GCSOA driven with 120 mA (a) and a LOA driven with 175 mA (b).

Description	Value
Length active region	1000 μm
Length left reflector	400 μm
Length right reflector	400 μm
Width	2 μm
Thickness	.15 μm
Injected current	$120mA$
Gain suppression coefficient	2.59 W^{-1}

Table 5.2: Physical parameters of the GCSOA used in the simulations

smaller then the input saturation power, a clear resonance phenomenon is observed, resulting in a decrease in small-signal gain. A simple, one sectional small-signal calculation neglecting the gain suppression can help to explain this [85]. The analysis resulted in the following equations for the variations of the carrier density and the signal power:

$$\frac{\Delta N}{\Delta S_{sig}(z=0)} = \frac{j.\Omega.K}{(\Omega^2 - \Omega_R^2) - j.\Omega.\gamma} \tag{5.5}$$

$$\frac{\Delta S_{sig}(z=L)}{\Delta S_{sig}(z=0)} = G_{sig}^0(1 + S_{sig}(z=0).\frac{L}{v_g}.\Gamma.a.\frac{\Delta N}{\Delta S_{sig}(z=0)}) \tag{5.6}$$

with Ω the frequency of the applied sine, K a constant proportional to G_{sig}^0 (i.e. the CW signal gain per second). Ω_R and γ are the well-known resonance frequency and the damping of the incorporated laser under injection of an optical signal. The second order resonant behavior observed in the carrier density variations (Eq. 5.5) leads to a maximum amplitude at the resonance frequency while being in anti-phase with the input signal variations. This obviously results in a dip in the small-signal gain. The resonance frequency turned out to be proportional to the remaining laser power in our simple calculations, which explains the shift to lower frequencies of the dip at higher CW input powers. This was the case for all the currents applied in our study (up to 300 mA). This shows that the reduction of Ω_R by the decrease of the laser power was dominant over the possible increase of Ω_R due to the self- and cross-gain saturation effects [86].

From the simulations we could conclude that the higher carrier density variations occurring when less laser power was present resulted in an increasing dip depth of the small signal gain. This also shows that

even if there isn't a clear maximum in the laser power oscillation any more due to an increased damping, there still exists a clear maximum in the carrier density variations, thereby still inducing a clear minimum in the small-signal gain. Once the laser oscillation is quenched (i.e. once we exceed the input saturation power), we get the well-known high-pass characteristic of a SOA [95]. At intermediate input power, slightly lower than the input saturation power, a gradual transition takes place from the resonance regime to the SOA-regime.
It should be noted that in any case the low frequency limit is formed by the derivative of the gain versus input power, whereas the high frequency limit equals the CW gain.

The small-signal gain of an LOA driven with a current of 175 mA in the co-propagation setup is depicted in Fig. 5.2(b). Different regimes can again be observed, however significantly differing from the GCSOA case. To ease the explanation, it is important to note that a LOA can be seen as a concatenation of "independent"lasing sections. With increasing input power, subsequently lasers will be quenched, starting at the back of the LOA. This means that a part of the LOA is already acting as a simple SOA, while the front part is still in the gain clamping regime. At input powers for which the lasing is still present over the entire length of the component (e.g. -30 dBm) we see that again an almost frequency independent amplification. Once a part of the LOA stopped lasing (e.g. -20 dBm) the lasers with only a little laser power remaining in the cavity again start to influence the small-signal gain. Since it is only the result of several oscillating laser sections, each providing a small part of the total gain, the strength of the resulting dip is however much smaller as compared to the GCSOA. Detailed inspection however again revealed an increasing dip depth and a very small decrease of the resonance frequency with increasing input power. The increasing dip depth mainly originates from the increasing number of oscillating sections which are close to cut-off, together with the increased amplitude of the carrier density oscillations. Once a significant part of the component stopped lasing, this part acts as an SOA, with an associated high pass nature. This causes the drop in gain of the low frequencies at higher input powers. There exists a much more gradual transition to the pure high pass SOA characteristic as compared to the GCSOA. [77]

In the counter-propagation regime, a different behavior is observed in both components. Fig. 5.3(a) depicts the small-signal gain of the same GCSOA as used above, in the counter-propagation setup. Due to the big reservoir of laser power stored in the cavity, we obtain again

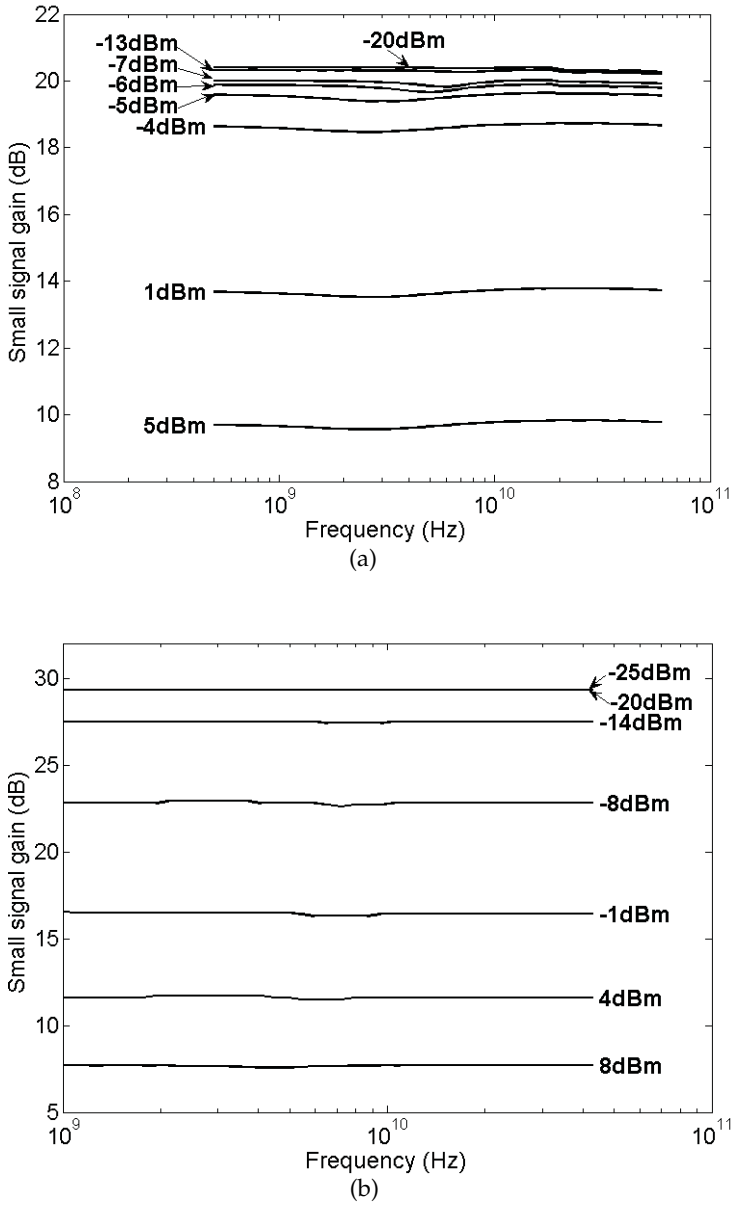

Figure 5.3: Simulated small-signal gain in the counter-propagation regime for different CW input powers injected in a GCSOA driven with 120 mA (a) and a LOA driven with 175 mA (b). In (b) the curves corresponding with -20 dBm and -25 dBm coincide.

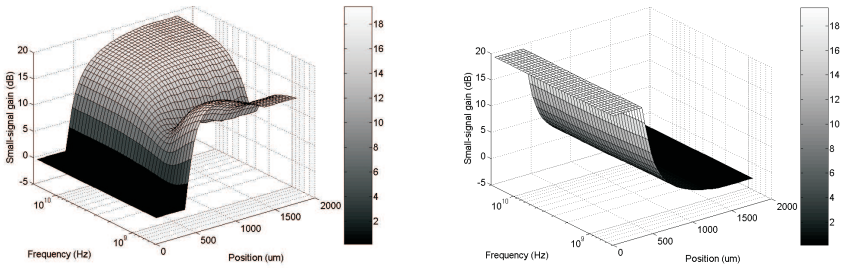

(a) (b)

Figure 5.4: Evolution of the amplitude of the injected sine (expressed in dB relative to input amplitude) versus length in the co-propagation case (a) and counter-propagation case (b) for a GCSOA with an injected CW power of -5 dBm. Notice that in the co-propagating case the signal is injected from the left hand side and the gain increases from left hand side to right hand side, while in the counter-propagating case it is the other way around. In both cases however, the amplifier is saturated in the back part.

an almost frequency independent gain relation for low input powers. When approaching the input saturation power, things change again. In this case however, only a weak resonance phenomenon is observed. As high-frequency limit, we get again the CW gain is found as was the case for the co-propagating RF component. The low frequencies however are inducing a relatively small laser power oscillation, as compared to the previous case. This is mainly caused by the fact that the amplitude of the sine is still relatively small in the part of the amplifier were the saturation is most present, being most vulnerable to input power variations. This can be understood by comparing Fig..5.4(a) and Fig. 5.4(b). In Fig. 5.4(a) we see a clear resonance combined with low frequency absorption occurring in the right, gain flattening part of the component. In Fig. 5.4(b) on the other hand we can see that in this part the backward propagating signal still has a very small amplitude, which only becomes significant in the less saturated front part of the component. The difference in laser modulation amplitude induced by co- and counter-propagation was logically the biggest for input powers in the transition zone mentioned in the co-propagation analysis. For the same reason, also in the SOA regime we get a fairly constant small signal frequency response, equal to the CW gain.
Similar results were found for the case of the LOA. Results corresponding to the same LOA as in the co-propagation case are given in

Fig. 5.3(b). The less pronounced resonance in any case is even more logical in this case, since the amplitude of the excitation in the vicinity of the oscillating laser sections is much smaller as compared to the forward case.

As a **conclusion** we can state that in both amplifier types a clear resonance phenomenon is observed for input powers in the vicinity of the input saturation power in the gain felt by a RF component co-propagating with a CW signal. This results in a decrease of the RF gain. In the LOA this is however less pronounced due to the local gain clamping mechanism versus the global clamping of the GCSOA gain.
If the RF component and the CW signal are injected from opposite sides, the resonant behavior is much weaker, mainly due to the small amplitude of the sine in the part of the component saturated by the CW signal. This is the case for both types of amplifiers.

5.3.2 Experiments

Experimental setup

Experiments were performed in order to validate the results found in the simulations. A setup as depicted in Fig. 5.5 was used. The input signal was generated using a tunable laser emitting at 1550 nm.
For the co-propagation case (Fig. 5.5(a)) the signal was modulated by a weak sinusoidal electrical signal generated by a RF signal generator. In this way, a CW signal with a sinusoidal modulation with approximately 10% modulation depth was obtained. The EDFA was used to compensate for the loss induced by the modulator. Keeping this part fixed, the VOA following the EDFA could now be used to change the input CW power, thereby retaining a constant modulation depth in all cases. The component, surrounded by two isolators, was followed by an optical filter to select the data signal. Finally an electrical spectrum analyzer was used to measure the strength of the RF component in the output signal. By sweeping the RF input frequency, the wanted characteristics could be obtained. Important to note is that a scaling on the frequency response of the modulation characteristic of the modulator had to be done. The bandwidth turned out to be little more then 10 GHz, thereby limiting the reliability region of the measurements.
In the counter-propagation setup (Fig. 5.5(b)), the input CW signal was split and only a small part was guided towards the modulator. This small part was modulated by a sine with a modulation depth of approximately 100%. The EDFA/attenuator combination was used to ad-

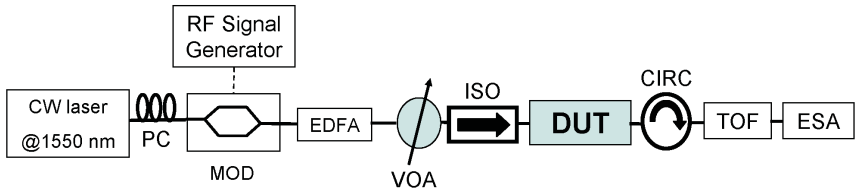

(a)

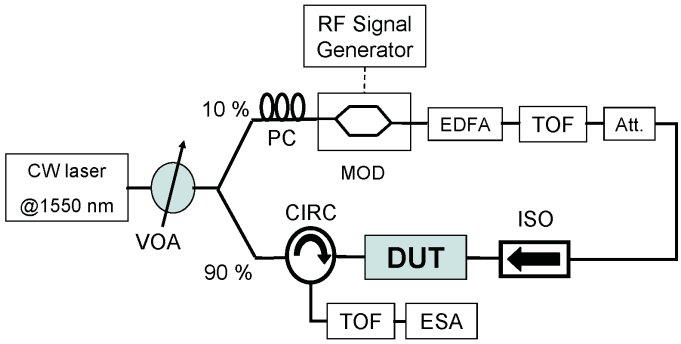

(b)

Figure 5.5: Experimental setups used for the determination of the small-signal gain of a RF signal co-propagating (a) and counter-propagating (b) with a CW pump. Abbreviations used are PC: Polarization Control; MOD: 10 Gb/s optical modulator; VOA: Variable optical attenuator; ISO: isolator; DUT: Device under test; CIRC: circulator; TOF: Tunable optical filter; ESA: Electrical spectrum analyzer; Att.: Attenuator.

just the mean of this modulated signal to a tenth of the CW input signal. An isolator and circulator fed the two components to the DUT on the opposite sides. Again, an optical filter combined with an electrical spectrum analyzer were used to determine the output amplitude of the RF component. The attenuator following the tunable light source was used to adjust the input CW power. The output spectrum was now scaled on every input spectrum, thereby avoiding inclusion of non-linearities of the optical modulator.

The GCSOA used during the experiments was a commercially available component acquired from Alcatel [69] some years ago. The lasing wavelength was 1508 nm. During the experiments the GCSOA was driven with 120 mA. It had a DC gain of 18 dB for the given sig-

nal wavelength. It should be noted that the probe and signal wavelength were both sufficiently detuned from the lasing wavelength of the GCSOA used during the experiments to avoid injection locking [96] and internal reflections. The LOA used was a prototype fabricated by Genoa, [78]. It was driven at 150 mA. It had a DC gain of 16.5 dB for the signal wavelength.

Results

Small-signal gain characteristics for the GCSOA and LOA obtained from experiments corresponding to different CW input powers are given in Fig. 5.6 for the co-propagation setup. In order to visualize the weak resonant behavior, at an input power of -11 dBm, for the case of the LOA only a small input power region is depicted. The behavior resembles in both cases very good with the simulation results. For the GCSOA we observe indeed a rather strong dip of the co-propagation AM gain when approaching the input saturation power (approximately -9.5 dBm). Whereas for low input power, an almost constant SSFR (small-signal frequency response) is obtained. For the GCSOA, a sudden switch to the high-pass SOA characteristic can be observed once the input saturation power is exceeded, in contrast with a more gradual transition in the LOA. The biggest difference was observed in the value of the resonance frequency of the LOA, which is little more than 1 GHz, whereas this was much higher (somewhat smaller than 10 GHz) in the simulations. A similar difference was found between the measurements presented in [88] and the model of [87] (i.e. approximately 3 GHz and 10 GHz respectively). However, this absolute value is not that important in understanding the effects discussed here. Of course the lower resonance frequency leads to much smaller crosstalk at higher bit rates, which is advantageous in WDM applications.

The counter-propagation setup resulted in the characteristics depicted in Fig. 5.7. A fairly constant SSFR is obtained for all the input powers, within the given measurement accuracies. This corresponds again good to the conclusions drawn from the simulations. By comparison with the co-propagation measurement we see that the obtained constant gain is almost equal to the high frequency limit of the previous case, with a small deviation in the saturated case possibly caused by a little consumption of the DC gain by the counter-propagating modulated signal.

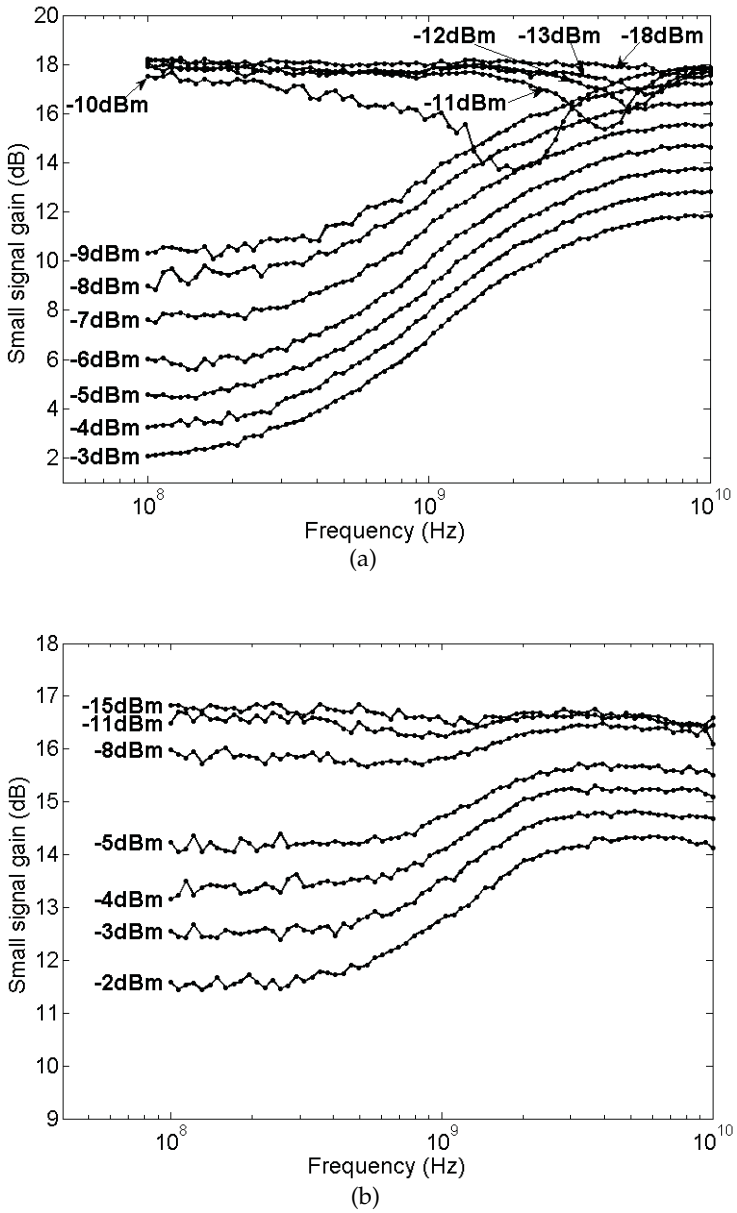

Figure 5.6: Experimentally obtained small-signal gain curves of a GCSOA driven with 100 mA (a) and of a LOA driven with 150 mA (b) in the co-propagation regime.

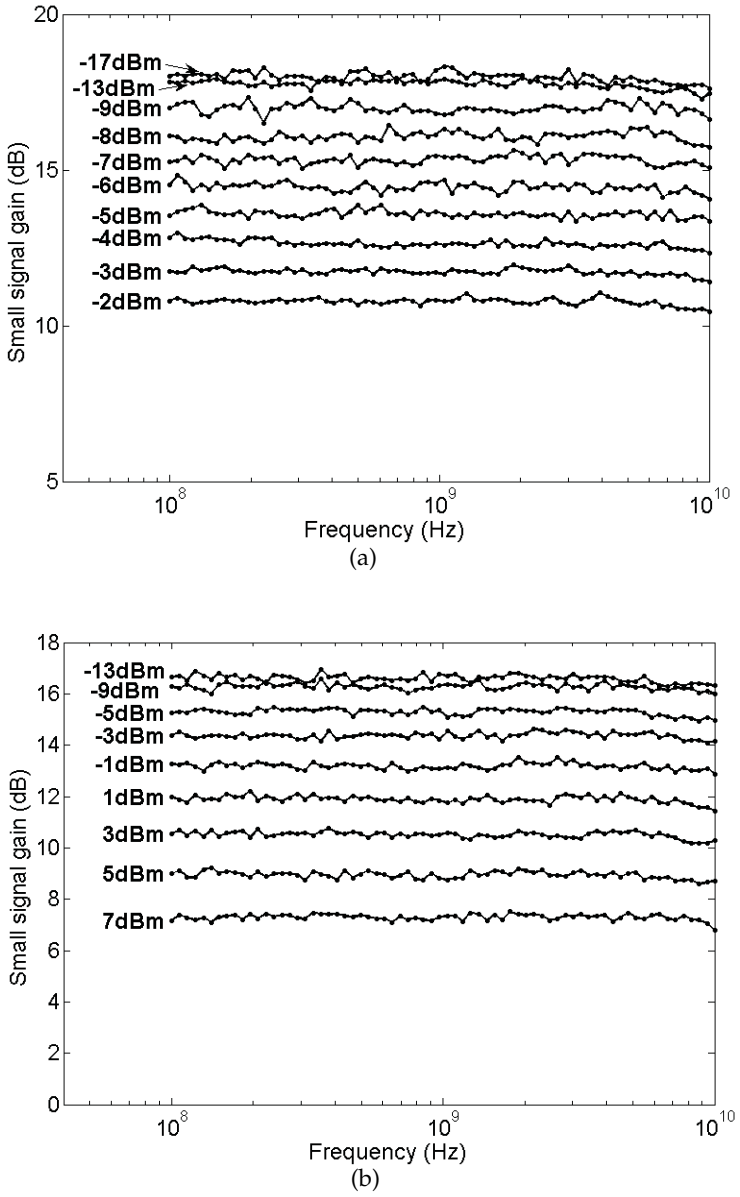

Figure 5.7: Experimentally obtained small-signal gain curves of a GCSOA driven with 100 mA (a) and of a LOA driven with 150 mA (b) in the counter-propagation regime.

5.4 Small-signal crosstalk behavior

5.4.1 Simulations

In addition to the small-signal gain it is also interesting to check how the effective fluctuations of the gain felt by a weak probe behave as function of input CW signal power and frequency. These crosstalk characteristics were calculated by observation of the amplitude of the modulation induced on a CW probe with an input power of -50 dBm, injected at the front (forward propagating crosstalk) and the back (backward propagating crosstalk) of the amplifier. The wavelength of the probe was chosen 3 nm smaller then the signal wavelength. The small-signal crosstalk was defined as the ratio of the amplitude of the probe output power variations to the mean probe output power, in accordance to [78]. Again both the co- and counter-propagation injection scheme were studied.

Results obtained in this way for the GCSOA used in the simulations of the small-signal gain are depicted in Fig. 5.8(a) for the co-propagation setup. As long as a significant amount of laser power is still present in the cavity, a clear maximum is observed in the crosstalk on both the forward and backward propagating probe. For those low input powers, the amount of crosstalk is proportional to the input CW power. Since the gain modulation is proportional to the modulation of the carrier density (combined with some gain suppression), this resonant behavior could also be concluded out of Eq. 5.5. Such a resonance was predicted theoretically for a forward propagating signal under large signal modulation in [85] and for small-signal modulation in [80]. At high and low frequencies, a very low crosstalk can be observed. At low input powers, this is due to the fact that the laser power oscillation is still in anti-phase with the injected RF signal. This renders an almost constant average power present in the active layer. At high frequencies the low crosstalk is the result of the finite carrier lifetime, due to which the fast variations of the input signal can not be followed by the carrier density any more. At high input powers, we observe the convergence to the low pass characteristic of a SOA, showing a small overshoot due to the finite loss in the cavity [97]. It can be seen that this crosstalk is always larger than in any gain clamped regime.

The crosstalk on the backward propagating probe turns out to be smaller than the one induced on the forward probe in any case. This can be intuitively understood by noting that in the case of the forward probe, the source of the gain variations is constantly accompa-

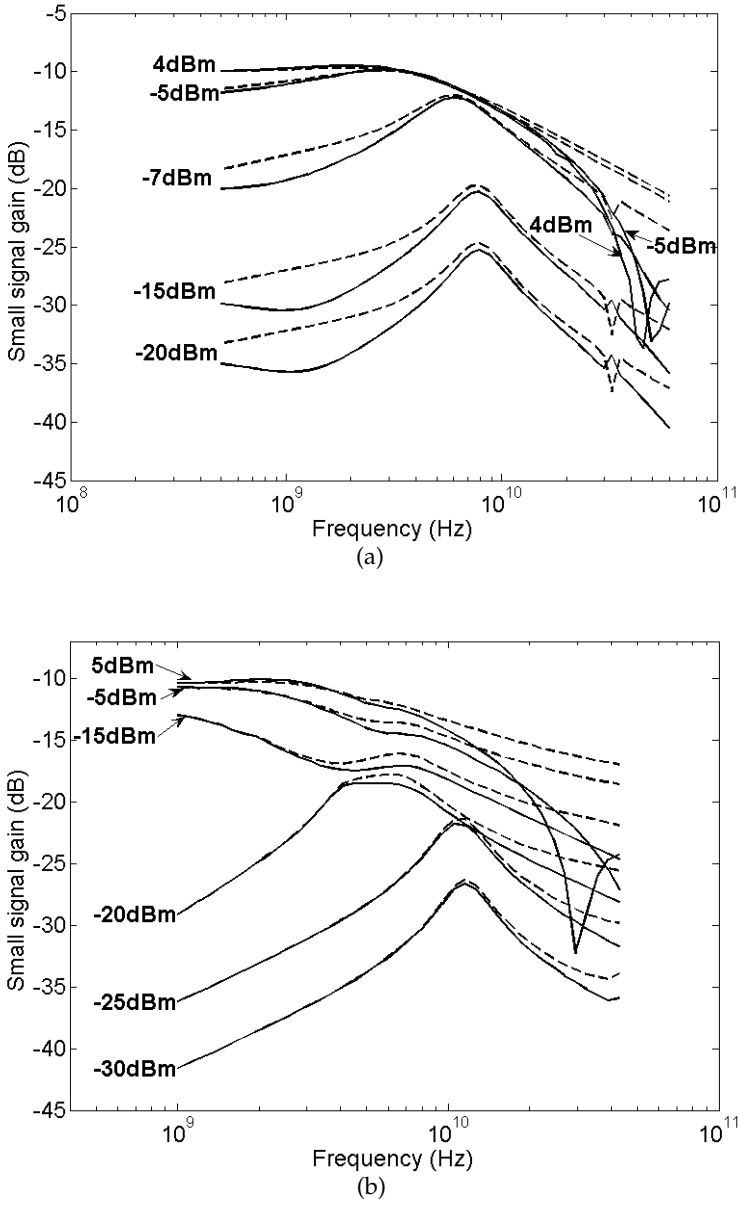

Figure 5.8: Simulated crosstalk induced on a weak probe signal of -50 dBm in the co-propagation regime for different CW input powers in the case of the GCSOA (a) and of the LOA (b). Full lines and dashed lines correspond to backward and forward propagating probes respectively.

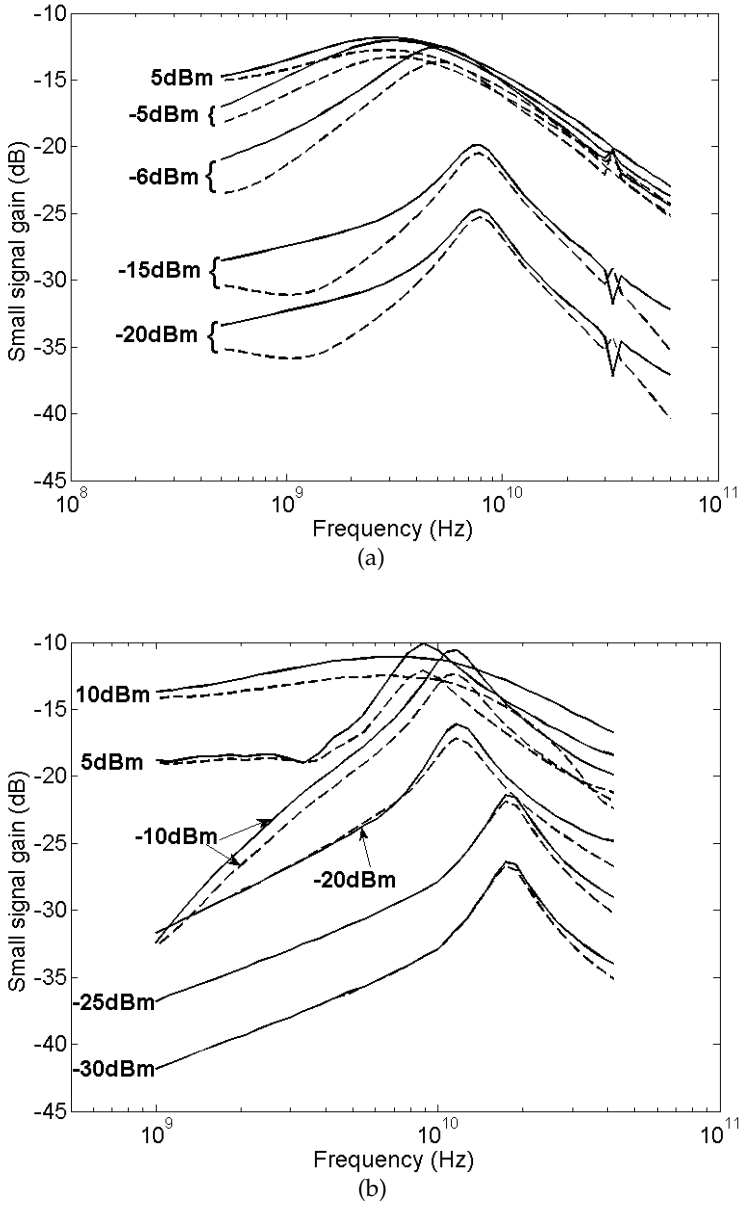

Figure 5.9: Simulated crosstalk induced on a weak probe signal of -50 dBm in the counter-propagation regime for different CW input powers in the case of the GCSOA (a) and of the LOA (b). Full lines and dashed lines correspond to backward and forward propagating probes respectively.

nied by the probe itself. At very low frequencies, this is also the case for the backward propagating probe, which results in an identical low frequency limit for both propagation directions of the probe. As the signal frequency increases however, a phase difference exists between the local carrier density modulation (due to the signal and forward and backward propagating laser powers) and the probe modulation (already accumulated during earlier propagation). This results in a difference between the crosstalk in both directions. A similar difference could be observed between the modulation of the forward and backward propagating laser powers. At higher frequencies we observe a stronger decrease of the backward crosstalk due to the fact that if the components transit time becomes comparable with the period of the signal, the backward propagating probe signal only feels an average of the carrier density change. This walk-off effect has been mentioned before as being a bandwidth limiting factor for wavelength conversion using XGM in a SOA in the counter-propagating regime [98]. For the case of no remaining laser power we see this even leads to a minimum when half of the period of the input signal is equal to the propagation time in the component ($\approx$ 12 ps). [77]
In [99] a resonance in the laser power modulation at a frequency equal to the inverse of the round trip time ($\approx$ 2x1400 μm) was reported due to the excitation of one of the optical sidemodes of the cavity. This resonance results in a discontinuity in the crosstalk at this frequency.

Crosstalk simulations corresponding to the co-propagation injection scheme using the LOA are given in Fig. 5.8(b). At low input powers, a resonant behavior can again be observed. This was already reported by a small-signal analysis in [87] and by experiments in [88]. Once a part of the component is saturated, a gradual transition takes place from this resonant behavior to the low-pass behavior of a simple SOA. The walk-off effect discussed above causes again a decrease of the backward propagating crosstalk at higher frequencies. A minimum can be found at a frequency equal to the inverse of half of the propagation time of the saturated part. Therefore, this frequency decreases as the LOA gets more and more saturated. A discontinuity as was observed in the case of the GCSOA due to the excitation of an optical sidemode of the cavity will not be observed here due to the smaller cavity length of typically a few μm (resulting in a much higher frequency). In addition also the model would not have allowed to predict this. The differences between forward and backward crosstalk observed at lower frequencies in the case of the GCSOA are not present in this case. This stems

from the local coupling between the (local) laser field and the signal in the LOA, whereas in the GCSOA there is a global coupling between the z-dependent laser field and the z-dependent signal.

Results obtained for the crosstalk simulations for both components in the counter-propagation scheme are depicted in Fig. 5.9.

For the GCSOA a crosstalk almost identical to the co-propagation scheme can be found as long as only a small CW input power is injected. When the component is used deeper into saturation, significant differences are observed, with overall a smaller crosstalk for the counter-propagating case. As was the case for the small-signal gain, this is mainly caused by the smaller amplitude of the RF signal in the most saturated part of the amplifier. The walk-off effect observed at higher frequencies in the co-propagating case is now less pronounced. This could also be seen in the saturated case, where the previously mentioned minima are not that strong anymore since in parallel with the weak forward propagating probe signal, there is also the strong CW signal. In the SOA case, a more explicit overshoot is observed as compared to the co-propagation case. In [97] it was stated that for the counter-propagating case an overshoot exists regardless of the magnitude of the waveguide loss, which explains the difference. This results in an increase of the 3 dB XGM bandwidth for both propagation directions, be it with a smaller efficiency.

Results of the LOA show that in the input power region where almost no saturation exists characteristics with almost the same peak values as in the co-propagation case are obtained. The resonance occurs at higher frequencies due to the fact that this resonance is induced in the front part, still containing more laser power. For higher input powers a gradual convergence takes place from the resonant behavior to the low pass behavior of a simple SOA. Detailed inspection revealed a decreasing resonance frequency for higher input powers and an increase of the SOA 3 dB bandwidth. This resonance contribution stays relatively important over a larger input power range as was the case in the co-propagation scheme since now the remaining laser power is present in the part were the amplitude of the variation is bigger. For input powers at which the lasing stopped in the entire component, a low pass characteristic with significant overshoot is found.

5.4.2 Experiments

Experimental setup

For the crosstalk measurements an extra probe signal with an amplitude of -25 dBm was added to the setups of Fig. 5.5, generated by a DFB laser diode emitting at 1542 nm. To measure the forward and backward crosstalk in the co- and counter-propagation setup respectively this could be simply done by adding the probe to the signal path, and to retune the TOF to the probe wavelength. In order to measure the crosstalk in the opposite direction of the modulated signal, the circulator and the isolator must be switched place. The crosstalk was in any case measured by the ESA as the ratio of the amplitude of the induced modulation to the average detected power.

Results

The forward and backward crosstalk characteristics obtained in the co-propagation injection scheme from the experiments for the GCSOA and the LOA are given in Fig. 5.10(a) and (b) respectively. For clarity reasons, the curves corresponding to only a few input powers are depicted.

A good agreement with the simulation results is found in the case of the LOA. The gradual transition from the resonant to the low pass regime is observed, with the combination of both in between. Also the walk-off effect discussed previously for the backward probe at higher frequencies can be observed in the difference in slope. The minimum could however not be observed due to the high frequency at which this occurs.

In the case of the GCSOA, somewhat less accurate measurements were obtained in the low frequency range, however they still were suitable to illustrate the most important trends. Detailed inspection showed again the difference in slope between forward and backward propagating crosstalk in the saturated case. At low input powers we can clearly see the explicit resonance. The deviation between backward and forward propagation in the low frequency is somewhat less explicit as was the case in the numerical study however still visible. [77]

The crosstalk results of both components in the counter-propagation regime are summarized in Fig. 5.11.

LOA results do agree again rather good with the simulations. The increase of the slope at low frequencies for input powers in the transi-

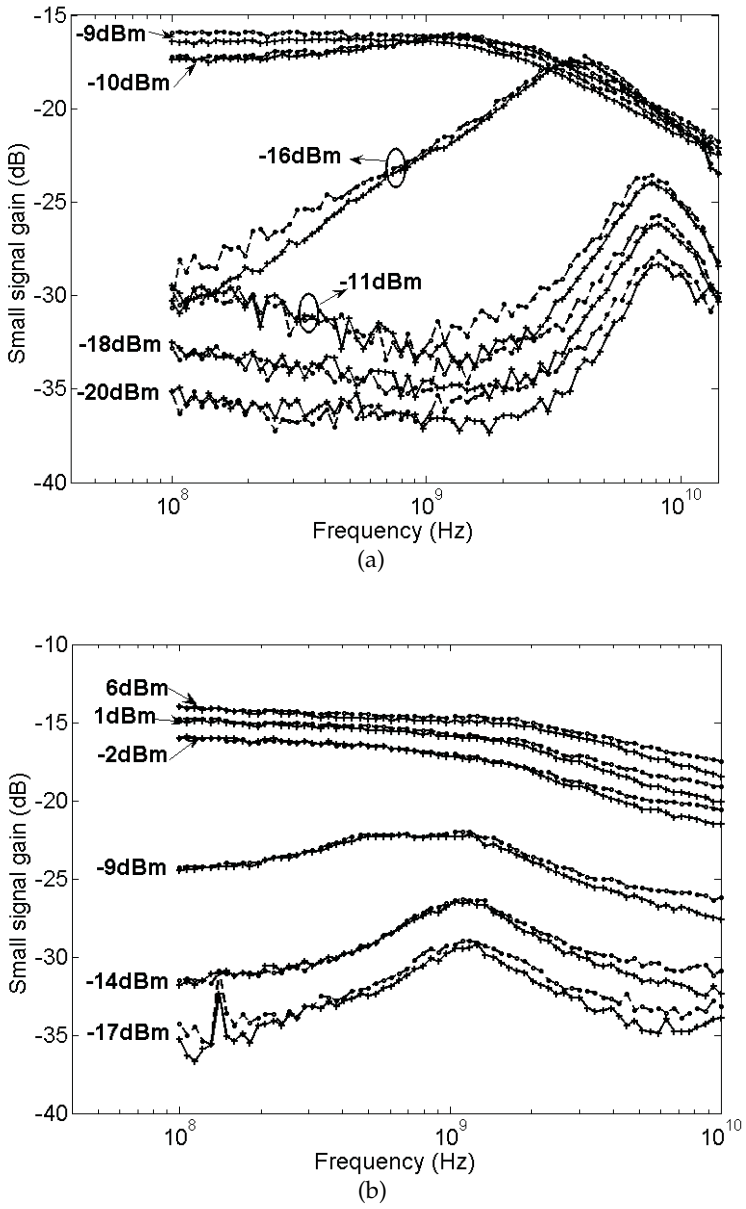

Figure 5.10: Experimentally obtained crosstalk in the co-propagation setup of a forward and a backward probe of -25 dBm with the GCSOA driven with 100 mA (a) and the LOA driven with 150 mA (b). Dashed line with circles: forward probe; full line with crosses: backward probe.

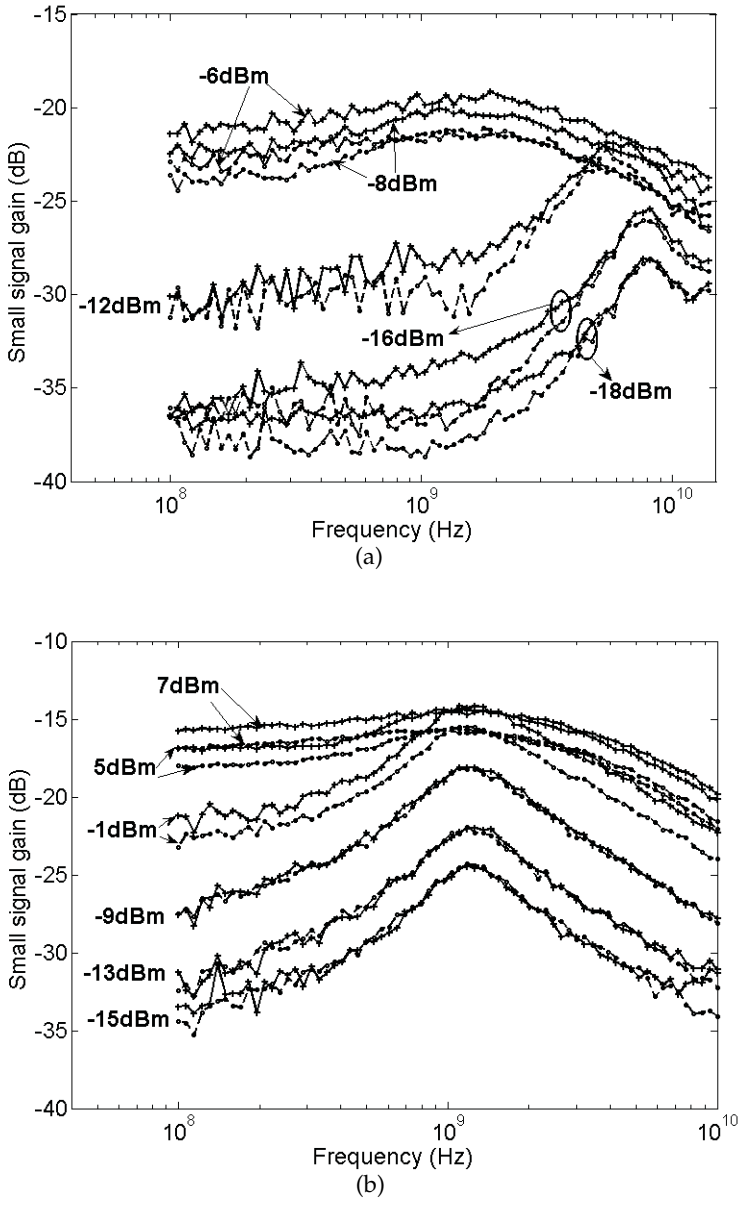

Figure 5.11: Crosstalk obtained from experiments of a forward and a backward probe of -25 dBm in the counter-propagation setup with the GCSOA driven with 100 mA (a) and the LOA driven with 150 mA (b). Dashed line with circles: forward probe; full line with crosses: backward probe.

tion zone is less pronounced here due to the lower resonance frequency, thereby not differing much from the cut-off frequency of the SOA low pass characteristic. The more explicit overshoot in the SOA low pass characteristics as compared to the forward case can also be observed. In agreement with the simulations, a less pronounced walk-off effect is present.

Results obtained with the GCSOA tend to be a little less accurate, but as was the case above show most of the trends discussed above.

5.5 Conclusion

The behavior under small-signal optical modulation of two types of gain-clamped optical amplifiers was extensively studied. Both simulations and experiments were performed. For the LOA a time domain simulation model was developed, whereas for the GCSOA the simulation tool CLADISS was used.

A first study determined the amplification of a RF component coresp. counter-propagating with a CW signal in function of the frequency for different values of the CW input powers. In the first injection scheme, a clear resonant behavior could be observed which resulted in a dip in the small-signal gain in function of the frequency as long as laser power was present in the cavity. This dip was significantly more pronounced in the case of the GCSOA due to the global clamping mechanism. In the LOA the gain turned out to be more locally clamped, thereby less influencing the total single pass gain. If the RF and the CW signal were injected from opposite sides on the other hand, an almost frequency independent gain was found. This was caused by the smaller amplitude of the injected RF signal in the parts of the component that were most vulnerable to input power variations. Experiments confirmed the findings of the simulations in all cases.

A second study consisted of the determination of the crosstalk induced on both a forward and a backward propagating probe signal in both injection schemes. A clear resonant behavior could be observed again as long as laser power was present in the cavity. Now this rendered a peak in the crosstalk, that shifted to lower frequencies for higher CW input powers. In function of the input power, a transition took place to the well-known low-pass behavior of a SOA. In the GCSOA this transition occurred much more instantly as compared to the LOA. Again this was caused by the way the internal laser action changed in function of the input power. A clear walk-off effect was observed , re-

sulting in a faster decrease for the backward propagating cross-talk as compared to the forward in the co-propagation scheme. In the counter-propagating regime this was less pronounced. In the lower frequency range, a difference in the crosstalk in the two propagation directions could be observed due to the shared propagation direction of signal and laser optical powers. This was not observed in the case of the LOA.

The difference of the clamping mechanism is most influencing the small-signal gain characteristics. The crosstalk on the other hand is behaving more similar. In the experiments the resonance of the crosstalk induced in the LOA turned out to be less pronounced. The study showed that when explicit resonance effects are unwanted the components can be best used at low saturation degrees.

Chapter 6

All-optical signal reshaping based on a simple MZI

As explained in section 1.3, degraded signals should be regenerated at intermediate distances. In the context of this work an all-optical reshaping element was developed showing clear regeneration potential if combined with a linear optical amplifier.
The proposed interferometer configuration contains one active arm, which results in the full exploitation of the dynamic properties of the components, without losing the bit rate transparency. Moreover, the scheme becomes very attractive if implemented as a multi-wavelength regenerator (by several MZIs operating in parallel) because the absence of a second active interferometer arm is advantageous concerning the power consumption and heat sinking. Our reshaping element exhibits a slightly smaller steepness than some other pass-through schemes that have been proposed so far (e.g. [68]). However, this is not a big issue since for a large number of cascaded links even moderate reshaping can significantly improve the signal quality and compensate for an increase of the amplifier noise figures [100].

In this chapter, first a motivation will be given for the proposed configuration. Then simulation as well as experimental results will be presented, and finally a conclusion will be drawn.

6.1 Principle of operation

The all-optical reshaping configuration has a MZI structure with one active arm, while the other arm is left transparent. The structure is

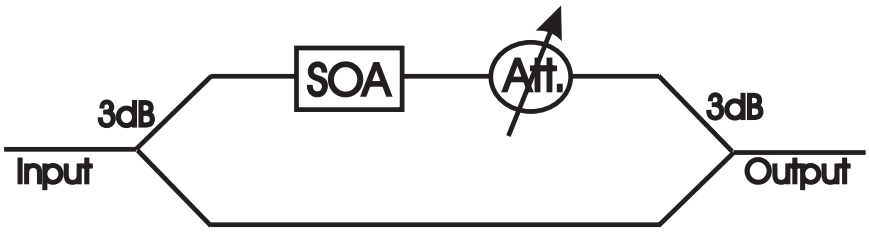

Figure 6.1: Schematic of the proposed configuration. Att.: variable attenuator, 3dB: 3 dB-splitter

schematically depicted in Fig. 6.1. In the arm containing the SOA a variable attenuator is inserted, which enables an efficient destructive interference at the output for low input levels. The necessary non-linear phase shift is thus only induced in one of the two interferometer arms, and is used to suppress the '0' level. A similar configuration, used as a wavelength converter, was previously proposed in [101]. However, in such a wavelength converter the phase change typically is only induced in one interferometer arm and therefore it makes less difference whether the other arm is active or transparent.

The main advantage of our regenerator scheme as compared to the all-active layouts (e.g. [72]), is the ability to regenerate much faster data rates when SOAs with similar properties are used. This can be understood as follows. Inherent to the all-active scheme, the input power levels of the zeroes are restricted to the vicinity of the lowest of the input saturation power levels of the SOAs. This is because the induced phase difference between both SOAs only changes in the input power region where one SOA is starting to saturate, while the other is still unsaturated. In the input power region where both SOAs are saturated or unsaturated, the induced phase shift difference remains constant, independent of the input power. Deep saturation of both SOAs, which results in a higher recovery speed [95], is therefore unachievable. Applying a higher current, another alternative to speed up an SOA [95], also gives rise to a higher amount of amplified spontaneous emission (ASE). This makes an enhancement of the speed at moderate input powers possible, but also results in a higher amount of ASE added to the regenerated signal, which is of course undesirable.

Those restrictions are not encountered when using a scheme as proposed here, because the necessary phase shift is only induced in a single active component. Thereby we can increase the input power for which destructive interference results, without being limited to a certain po-

wer range once the current is set. This will significantly enhance the dynamic properties. Other techniques proved to be feasible for much higher bit rates (e.g. 84 Gb/s in [39]), making use of e.g. differential schemes, but they all suffer from being bit rate dependent. It should be stressed that the technique proposed here won't reach such high speeds, but has a bit rate independent nature and in addition is much simpler.

6.2 Simulation results

To simulate the proposed regenerator, a one dimensional longitudinal multi-section single mode Finite Difference Time Domain (FDTD) SOA model was developed, based on the traveling wave field equations and longitudinal carrier density equations. The different equations used are given by:

$$\begin{aligned}\frac{\partial N(z,t)}{\partial t} &= \frac{I(t)}{qwdL} - AN(z,t) - BN^2(z,t) - CN^3(z,t) \\ &- \frac{G_{sig}(z,t)}{h\nu_{sig}wdv_g}\left[P_{sig}(z,t) + P_{ASE,F}(z,t) + P_{ASE,B}(z,t)\right]\end{aligned} \tag{6.1}$$

$$\frac{dP_{sig}(z,t)}{dz} = \left(\frac{G_{sig}(z,t)}{v_g} - \alpha_{\text{int}}\right) P_{sig}(z,t) \tag{6.2}$$

$$\frac{dP_{ASE,F}(z,t)}{dz} = \left(\frac{G_{ASE}(z,t)}{v_g} - \alpha_{\text{int}}\right) P_{ASE,F}(z,t) + \frac{1}{2}h\nu\beta_{sp}BN^2(z,t)wd \tag{6.3}$$

$$-\frac{dP_{ASE,B}(z,t)}{dz} = \left(\frac{G_{ASE}(z,t)}{v_g} - \alpha_{\text{int}}\right) P_{ASE,B}(z,t) + \frac{1}{2}h\nu\beta_{sp}BN^2(z,t)wd \tag{6.4}$$

$$\frac{d\phi(z,t)}{dz} = -\frac{1}{2}\alpha\Gamma a(N(z,t) - N_0) \tag{6.5}$$

with

$$G_{sig}(z,t) = \frac{\Gamma a(N(z,t) - N_0)}{(1 + \varepsilon\Gamma P_{sig}(z,t))}v_g \tag{6.6}$$

$$G_{ASE}(z,t) = \Gamma a(N(z,t) - N_0)v_g \tag{6.7}$$

To make the study of the carrier dynamics along the length of the SOA possible, the SOA is segmented into a number of smaller segments (e.g. 10 μm long). The electron rate equation (Eq. 6.1), in which

Parameter	Value	Description
A	1.66x10^8 s^{-1}	Nonradiative recomb. const.
B	10^-10 cm^3s^{-1}	Bimolecular recomb. const.
C	3x10^{-29} cm^6s^{-1}	Auger recomb. const.
d	.3 μm	Active layer thickness
w	.7 μm	Active layer width
L	2000 μm	SOA length
Γ	.59	Confinement factor
α_{int}	26.8 cm^{-1}	Effective loss coeff.
β_{sp}	1x10^{-2}	SE coupling coeff.
N_0	1x10$^{18}cm^{-3}$	Transparency carrier density
a	3x10$^{-16}cm^2$	Differential gain coeff.
ν_{sig}	193.55 THz	Signal frequency
v_g	8.33x10$^7ms^{-1}$	Group velocity
ε	3.7x10$^{-3}mW^{-1}$	Gain suppression coeff. [92]
I	$350mA$	Injected current
α	4	Chirp parameter [92]
q	1.60217733x10^{-19} C	Electric charge per electron
h	6.6260755x10^{-34} Js	Planck's const.

Table 6.1: Physical parameters of the SOA used in the simulations. SE: spontaneous emission, recomb.: recombination

N stands for the carrier density within a certain section, is then applied to each section of the cavity. Thereby, effects caused by longitudinal spatial hole burning are included. The propagating signal power ($P_{sig}(z,t)$) can be calculated by Eq. 6.2, which uses a linear gain model (Eq. 6.6) combined with a gain suppression factor ε. The latter is mainly caused by spectral hole burning. It is included because it significantly influences the dynamics. Equations 6.3 and 6.4 represent the amplification and generation of the forward ($P_{ASE,F}(z,t)$) and backward ($P_{ASE,B}(z,t)$) propagating ASE respectively. The spontaneous emission coupling factor β_{sp} is two orders of magnitude higher than the common value, because in this case we need the total amount of ASE present in all the modes, all contributing to the carrier depletion. The value was chosen such that a realistic static input saturation power of -19 dBm and a small-signal gain of 35 dB was obtained. In the gain relation of the ASE (Eq. 6.7), the spectral hole burning is left out due to the broadband nature of the ASE. Eq. 6.5 finally represents the phase change of the amplified signal during its propagation through

the SOA. The phase is denoted by ϕ(z,t). In the phase relation, as opposed to the gain suppression in the gain relation, no ultrafast effects are included. This stems from the fact that the ultrafast α-factors are relatively small compared to the α-factor associated with interband recombinations [102]. Table 6.1 shows the meaning of the other SOA parameters and physical constants used in the equations, together with the typical values used in the simulations [90]. The dimensions of the active layer, together with the associated optical confinement factor are based on SOAs reported in [103].

The interferometer output was constructed from the original input data signal (P_{in}) and the corresponding SOA output signal (P_{SOA} with phase ϕ_{SOA}) to which an adjustable but constant attenuation (A) and phase shift (Ph) was added. This can be expressed by the following equation:

$$P_{out} = \frac{1}{2}.\left(P_{in} + \frac{P_{SOA}}{A} + 2.\sqrt{P_{in}.\frac{P_{SOA}}{A}}.\cos(\phi_{SOA} + Ph)\right). \quad (6.8)$$

In practice the additional phase shift can be adjusted by slightly changing the drive current of the SOA.

The ultimate performance of the configuration was tested by means of the static reshaping curves. They revealed that an adjustable reshaping curve can be achieved, with specifications depending on the value of both adjusting parameters (phase and attenuation). Fig. 6.2(a) depicts some simulated static regeneration curves corresponding to different phase/attenuation combinations. We observe that a significant ER improvement can be achieved for a limited range of input ERs. The limited input power dynamic range is the result of the continuous increase of the phase difference with increasing input power. Note that the regenerator can also be optimized to perform efficient noise suppression.

For the dynamic simulations, a $2^9 - 1$ PRBS NRZ data signal was constructed with Gaussian distribution of the zero and one levels, in combination with a small amount of timing jitter. In Fig. 6.2(b) the output versus input ER is plotted for 3 series of 40 Gb/s NRZ signals. Each serie has a constant zero power level. We can see that for an input ER from 3 dB to 7 dB an improvement between 6 dB and 11 dB can be achieved. An example of an input and output eye diagram is depicted in Fig. 6.3. We also observe a clear noise suppression on both spaces and marks. The phase recovery time, the most important parameter

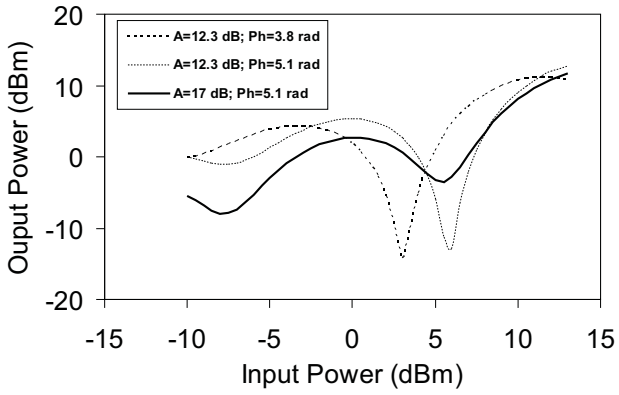

(a)

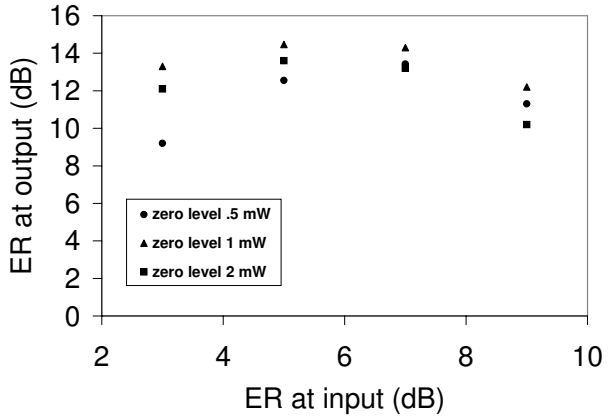

(b)

Figure 6.2: (a) Static regeneration curves obtained from the simulations for different phase/attenuation combinations.The values are printed in the inset box (A: attenuation, Ph: phase) (b) Simulated input versus output ER for three different series of 40 Gb/s NRZ signals. Each serie has a constant zero level.

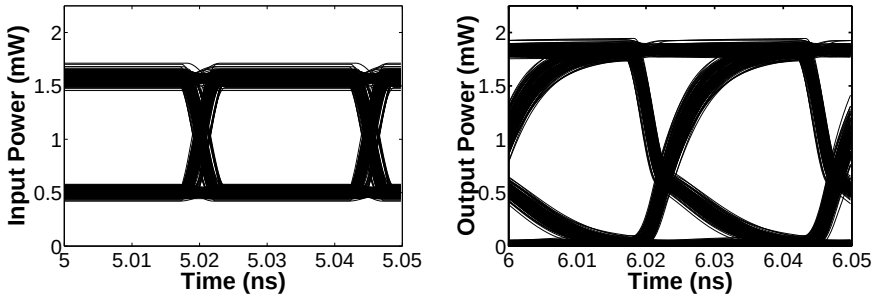

Figure 6.3: Simulated eye diagrams of a 40 Gb/s NRZ signal. Left hand side: the input signal to the SOA, right hand side: the output signal of the regenerator.

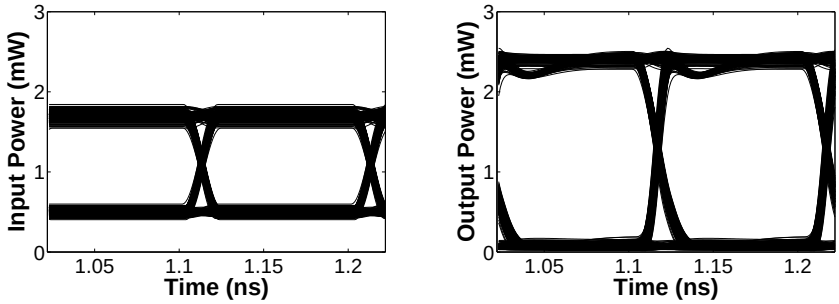

Figure 6.4: Simulated eye diagrams of a 10 Gb/s NRZ signal. Left hand side: the input signal to the SOA, right hand side: the output signal of the regenerator.

concerning the fast interference, was found to be approximately 14 ps in the case of deep saturation of the SOA. This corresponds to experimentally obtained values presented in [104]. The horizontal closure of the output eye diagram illustrates that 40 Gb/s will be close to the limit at which this configuration can work. By observing the eye diagrams corresponding to a 10 Gb/s signal in Fig. 6.4 it becomes clear that at such a data rate this horizontal closure is not an issue any more.

The simulations give proof of the reshaping properties of the given configuration up to bit rates of approximately 40 Gb/s when an SOA optimized for high speed operation could be used. Such an SOA should have a small active area, combined with a high optical confinement factor and a high differential gain.

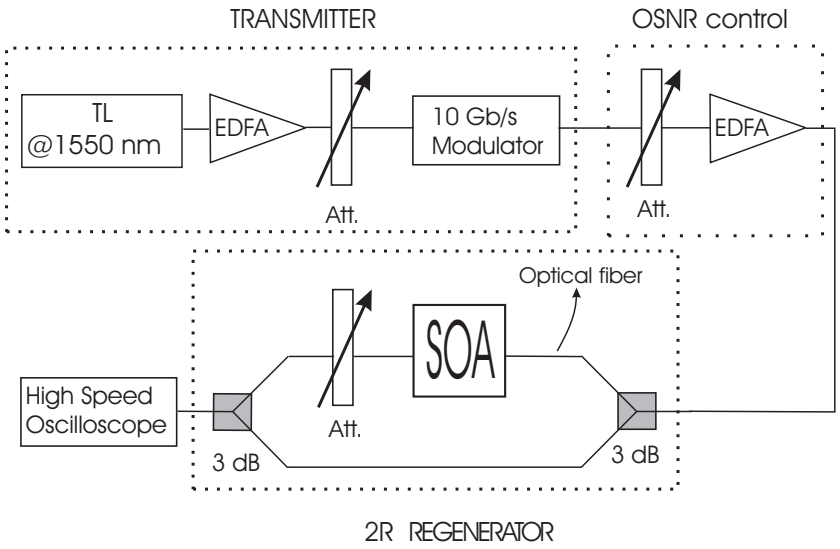

Figure 6.5: Experimental setup for the regeneration measurements. TL: Tunable Laser. Att: Variable attenuator.

6.3 10 Gb/s experiments

Fig. 6.5 shows the used experimental setup. At the transmitter side, the 10 Gb/s NRZ data signal was formed by externally modulating a CW signal from a tunable laser with a $2^{31} - 1$ PRBS bit sequence. An attenuator/EDFA pair is inserted, which serves as an optical signal-to-noise-ratio (OSNR) control subblock. The interferometer was constructed using two 3 dB splitters, a commercial SOA and a variable attenuator. As SOA, the same LOA was used as for the small-signal modulation experiments of chapter 5. This was not a problem since the LOA behaves like a simple SOA if used in deep saturation. The passive arm was formed by a single mode optical fiber. The output signal was detected using a high speed oscilloscope. The SOA was however not optimized for high speed operation.

In Fig. 6.6.(a) some static input versus output power curves obtained by applying different SOA currents are drawn. We clearly see that good reshaping can be achieved. We observe that an ER improvement of 13 dB is possible in combination with a suppression of the noise on the zero level. Moreover, it is possible to adjust the decision threshold. It should be noted that the different curves in Fig. 6.6(a) are all

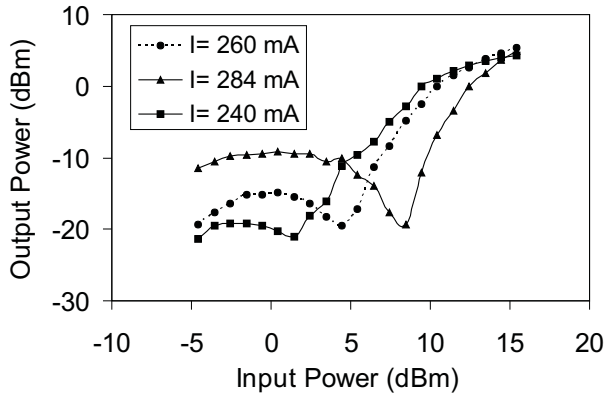

(a)

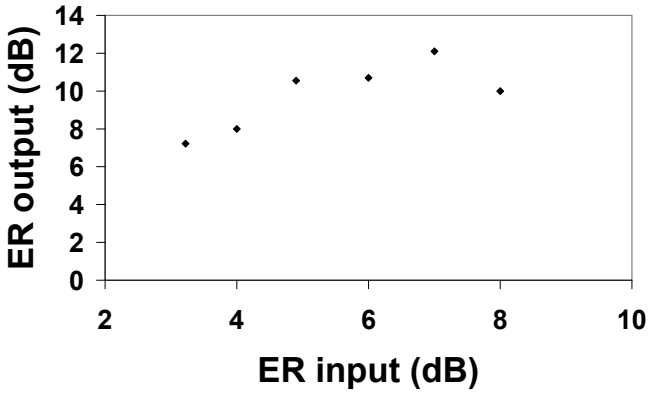

(b)

Figure 6.6: (a) Some experimentally obtained static regeneration curves corresponding to different currents applied to the SOA. (b) Input versus output ER obtained from the measurements for a 10 Gb/s NRZ signal by optimization for a maximum output ER.

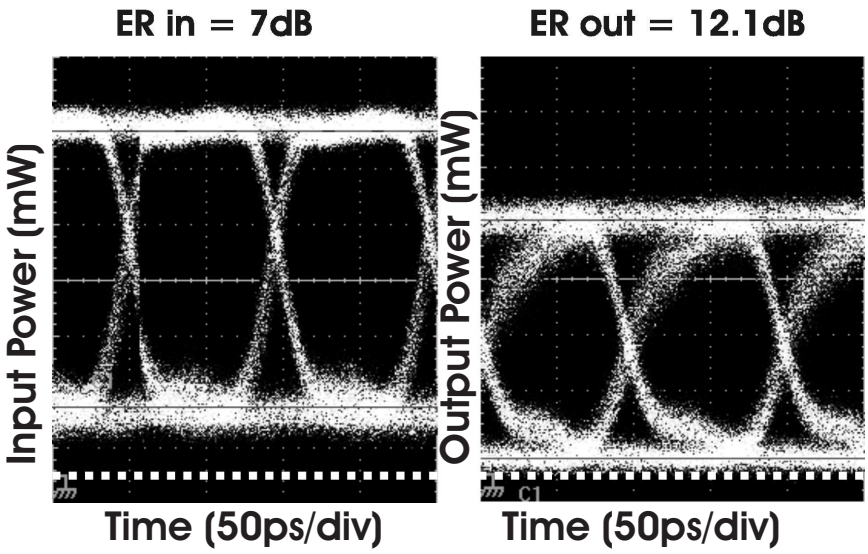

Figure 6.7: Measured eye diagrams of a 10 Gb/s NRZ signal. Left the input signal to the interferometer is drawn after 10 dB attenuation, right the 5 dB attenuated output signal of the regenerator. The dashed white line depicts the zero power level.

obtained with the same attenuation in the active arm, so by only adjusting the SOA current.

The performed dynamic measurements were eye diagram measurements. BER measurements were impossible due to the unstable nature of the fiber based interferometer. As in the simulations we measured the output versus input ER relations. The results are depicted in Fig. 6.6.(b). We observe an ER improvement of at least 4 dB over a range of 4 dB of input ERs. Also a small noise suppression on the mark and space levels could be observed. Due to the absence of a random noise generator in the SOA model, slightly lower values of the ER improvement as compared to the simulations were obtained. Therefore a nearly complete destructive interference could be obtained in the simulations, which obviously resulted in a higher output ER. Moreover, the slower dynamics of the component used made it impossible to optimize the result only towards a maximal ER improvement. The ER improvement had to be maximized, while keeping the horizontal eye closure acceptable. In Fig. 6.7 an example of an in- and output eye diagram is shown. We note that this optimization was achieved by adjusting only the SOA

current (and not the attenuation). The fact that a variable attenuation is not really necessary would make fabrication or use of a photonic integrated circuit version easier. A fixed loss is obviously easier to fabricate as compared to an adjustable loss.

The horizontal closure of the eye in Fig. 6.7 is mainly caused by the poor dynamic properties of the SOA used in the experiments. This indicates that higher bit rates should be achievable if a better SOA is used (e.g the SOA presented in [104]).

6.4 Conclusion

We presented a simple Mach-Zehnder interferometer configuration for the purpose of regeneration. It consists of one active arm, while the other arm is left transparent. This resulted in a better exploitation of the dynamic properties of the used amplifier due to the ability of using the component in deep saturation. The development of a 1D FDTD SOA model enabled dynamical simulations of the proposed configuration. This proved that reshaping up to bit rates of 40 Gb/s should be feasible if a component optimized for high speed operation could be used.

10 Gb/s NRZ experiments were performed using a prototype SOA in a fiber based interferometer. It proved the feasibility of the configuration of performing significant ER improvement in combination with a certain noise suppression. If a linear optical amplifier is added to the configuration, 2R regeneration becomes possible.

The experiments in combination with the simulations show that higher bit rates (at least 40 Gb/s) should be achievable, when a better SOA could be used in an integrated design. This integrated design should also allow BER measurements.

Chapter 7

Conclusions and Perspectives

All-optical signal monitoring

The main part of this PhD was devoted to all-optical performance monitoring. Due to the increased complexity of the optical communication networks, this has become a very important issue. An ideal optical performance monitoring application should be able to provide accurate signal quality information, to localize a fault in the network and additionally provide useful information about the origin of the signal quality degradation.

A lot of experimental and theoretical studies presented up till now demonstrated that the construction of a signal histogram (i.e. the probability distribution of the signal power) can be very interesting in this context. Synchronous as well as asynchronous histograms contain a lot of useful information concerning signal health and cause of degradation. We opted for the asynchronous approach since, despite the lack of timing information, they are still capable to identify degradation caused by noise, chromatic dispersion, non-linearities and crosstalk. Obviously they are also more easy to construct since the difficult synchronization is avoided. The asynchronous Q-factor, which is a generalization of the well-known (synchronous) Q-factor, has been identified as a very powerful tool for signal quality monitoring. In certain cases it can even provide a good BER estimate.

The current methods for the construction of signal histograms always make use of some kind of sampling system. Those sampling systems can be either electrical, opto-electrical or all-optical. In all cases

however this leads to rather complex and expensive setups. In this work, a new approach was presented to construct an asynchronous signal histogram that does not use any high frequency electronics. This is done by measuring the average output power of a highly non-linear optical component. This is repeated for the same input signal to which an increasing attenuation is applied. Doing so, we obtain a linear system with the probabilities as unknowns. The method does only require a fast optical component which shows a strong non-linear behavior with respect to the input power.
A simulation platform was developed to model the proposed method. Several approaches were used in order to extract meaningful solutions out of the ill-conditioned linear system. We concluded that including some a priori knowledge concerning the shape of the histogram could help to improve the overall robustness of the method. Of course this resulted in a decrease of the transparency. An approach that did not suffer from the latter was using so-called regularization techniques. This also clearly enhanced the achievable accuracy, be it not to the same extent. Both extraction strategies have therefore pro's and contra's. The choice of the correct approach can be triggered by the knowledge of the network part that has to be monitored.

In order to find a non-linear component suitable for a practical implementation, it was demonstrated that the condition number of the resulting system matrix could be used as a first indicator of the feasibility. Practical issues such as dynamical behavior, stability, reproducibility, etc. were however just as important. The 2R regenerator based on a SOA and a DFB laser placed in an optical feedback scheme was identified as the best candidate available at the lab. This was mainly due to the extreme sharp cut-off behavior of the laser power as function of the signal input power. A theoretical study proved that a decent extraction should be possible if the dynamic power transfer followed the assumed static transfer very accurately and in addition only a small amount of measurement noise was present.
The study indicated however that in any case a very accurate histogram was needed to result in accurate Q-values. This is inherent to any histogram construction method. In order to identify degradation mechanisms on the other hand, only the shape of the histogram can already be very helpful.

An experimental setup for a low bit rate proof-of-principle experiment was build. We used a commercial SOA/DFB combination as non-linear component. The experiments revealed that trends in the signal

quality could certainly be monitored. In other words, a sudden decrease of extinction ratio or signal to noise ratio could clearly be signalized. This can be interesting in a practical network, since the place at which the alarm occurs will probably also give an indication of the reason of the failure. Accurate Q_{avg} extraction was however not achieved. This was mainly caused by the deviation between the assumed static power transfer as compared to the practical power transfer under dynamic conditions.

Future work can consist of a few things. First of all a switch to ultra fast, fiber based non-linear components could probably solve the main problem. Care should however be taken with issues such as stability and polarization dependency. In any case this would provide a bit rate independent power transfer. Therefore, the performed theoretical study can become very useful once an power transfer can be provided. Secondly, more thorough and extensive automated experimental testing can possibly lead to a (bit rate dependent) relation between the extracted and the real histogram. This also includes the system specific relation between the bandwidth of the component and the bandwidth at the receiver side. This relation is important if eventually BER estimates are wanted.

GCSOA/LOA modeling

Since in the context of this PhD we often used various types of SOAs, the dynamical properties of two types of gain clamped SOAs were studied more in depth. It consisted of the LOA and the GCSOA, i.e. a SOA in which a vertical respectively longitudinal laser cavity is incorporated.

A study of the behavior under small-signal optical modulation revealed that a resonance in the carrier density and laser power oscillation resulted in a decrease of the small-signal gain in the vicinity of the corresponding resonance frequency. In the GCSOA this was clearly more pronounced. Injection of the RF component at the back facet resulted in a more frequency independent gain in both amplifier types.
A similar resonance was obviously observed in the small-signal crosstalk. It turned out that in the case of the small-signal gain, the local clamping mechanism of the LOA rendered a more stable, frequency independent behavior as compared to the global clamping mechanism in the GCSOA. To avoid explicit frequency dependent effects, both amplifiers can best be used in the weakly saturated input power region.

The developed LOA model can be used for the time domain analysis of future applications incorporating a LOA.

All-optical signal reshaping

Finally, also a simple MZI configuration for all-optical reshaping purposes was presented. It consisted of a MZI with one active arm, while the other arm was left transparent. This resulted in a better exploitation of the active component, since it could be used in deep saturation, rendering a better dynamic behavior. A SOA model was developed to simulate the configuration. Simulations proved that reshaping of high bit rate signals (40Gb/s) could be achieved if a high speed SOA could be used. Eye diagram measurements using a non-optimized SOA in an instable fiber-based interferometer demonstrated that at 10 Gb/s clear ER improvement could be achieved, combined with some noise suppression.
Future work can consist of the testing of integrated versions of the configuration, that are currently in production at the Technical University of Eindhoven. Using those devices, BER measurements should become possible.

Appendix

Appendix A

Acronyms

2R	Re-amplification Reshaping
3R	Re-amplification Reshaping Retiming
ASE	Amplified Spontaneous Emission
a.u.	arbitrary unit
AWG DEMUX	Arrayed Waveguide Demultiplexer
BER	Bit Error Rate
CD	Chromatic Dispersion
CW	Continuous Wave
DBR	Distributed Bragg Reflector
DC	Direct Current
DFB	Distributed Feedback
DUT	Device Under Test
(D)WDM	(Dense) Wavelength Division Multiplexing
EDFA	Erbium Doped Fibre Amplifier
ER	Extinction Ratio
ESNR	Electrical Signal to Noise Ratio
FDTD	Finite Difference Time Domain
FEC	Forward Error Correction
FWM	Four Wave Mixing
GCSOA	Gain Clamped Semicondutor Optical Amplifier
GCV	Generalized Cross-Validation
ISI	Inter Symbol Interference
LOA	Linear Optical Amplifier
MMI	Multi Mode Interference
MZI	Mach-Zehnder Interferometer
NOLM	Non-Linear Optical Loop Mirror

NRZ	Non Return to Zero
OADM	Optical Add Drop Multiplexer
OPM	Optical Performance Monitoring
OSNR	Optical Signal to Noise Ratio
OXC	Optical Cross-connect
PDF	Probability Density Function
PMD	Polarization Mode Dispersion
PRBS	Pseudo Random Bit Sequence
RF	Radio Frequency
SCM	Sub Carrier Multiplexing
SDH	Synchronous Digital Hierarchy
SFG	Sum Frequency Generation
SLA	Service Level Agreement
SOA	Semicondutor Optical Amplifier
T(G)SVD	Truncated (Generalized) Singular Value Decomposition
TOF	Tunable Optical Filter
VOA	Variable Optical Attenuator
XGM	Cross Gain Modulation
XPM	Cross Phase Modulation

Figures

Tables

Bibliography

[1] "http://www.c-i-a.com/pr0904.htm."

[2] G. Rossi, T. Dimmick, and D. Blumenthal, "Optical performance monitoring in reconfigurable WDM optical networks using subcarrier multiplexing," *J. Lightwave Technol.*, vol. 18, pp. 1639–1648, Dec. 2000.

[3] "http://www.ist-stolas.org/."

[4] I. Shake, H. Takara, and S. Kawanishi, "Technology for flexibly monitoring optical signal quality in optical communications," *NTT Technical Review*, vol. 2, pp. 29–34, May 2004.

[5] V. Chan, K. Hall, E. Modiano, and K. Rauschenbach, "Architectures and technologies for high-speed optical data networks," *J. Lightwave Technol.*, vol. 16, pp. 2146–2168, Dec. 1998.

[6] A. Kirstädter, M. Wrage, G. Göger, W. Fischler, and B. Spinnler, "Current aspects of optical performance monitoring and failure root cause analysis in optical WDM networks," *Proc. International Conference Asia Pacific Optical Communications (APOC), Beijing, China*, Nov. 2004.

[7] D. Kilper, R. Bach, D. Blumenthal, D. Einstein, T. Landolsi, L. Ostar, M. Preiss, and A. Willner, "Optical performance monitoring," *J. Lightwave Technol.*, vol. 22, pp. 294–304, Jan. 2004.

[8] R. Friskney, K. Warbrick, S. Poliakoff, and R. Heath, "Link-based photonic path performance prediction and control," *Proc. ECOC*, p. 7.4.3, Sep. 2002.

[9] P. Vorreau, D. Kilper, and J. Leuthold, "Optical noise and dispersion monitoring with SOA-based optical 2R regenerator," *IEEE Photon. Technol. Lett.*, vol. 17, pp. 244–246, Jan. 2005.

[10] C. Larsen and P. Andersson, "Signal quality monitoring in optical networks," *Optical Networks Magazine*, pp. 17–23, Oct. 2000.

[11] S. Dods, D. Hewitt, P. Farrell, and K. Hinton, "A novel broadband asynchronous histogram technique for optical performance monitoring," *Proc. Opt. Fiber commun. Conf.*, vol. 4, pp. 190–192, Mar. 2005.

[12] S. Yamamoto, H. Takahira, and M. Tanaka, "5 Gbit/s optical transmission terminal equipment using forward error correcting code and optical amplifier," *IEE Electron. Lett.*, vol. 30, pp. 254–255, Feb. 1994.

[13] G. Bendelli, C. Cavazzoni, R. Girardi, and R. Lano, "Optical performance monitorings techniques," *Proc. ECOC*, pp. 113–116, Sep. 2000.

[14] A. Liu, G. Pendock, and R. Tucker, "Chromatic dispersion monitoring using time-multiplexed in-band RF tones," *Proc. Opt. Fiber commun. Conf.*, p. OThH6, Mar. 2005.

[15] T. Takahashi, T. Imai, and M. Aiki, "Automatic compensation technique for timewise fluctuating polarisation mode dispersion in in-line amplifier systems," *IEE Electron. Lett.*, vol. 30, pp. 348–349, Feb. 1994.

[16] D. Kilper, S. Chandrasekhar, L. Buhl, and A. Agrawal, "Spectral monitoring of OSNR in high speed networks," *Proc. ECOC*, p. 7.4.4, Sep. 2002.

[17] G. Jacobsen, L. Gillner, and O. Franson, "On the use of OSNR for BER monitoring in wdm systems and optical networks," *J. Opt. Commun.*, vol. 21, no. 1, pp. 20–23, 2000.

[18] S. Yamamoto, N. Edagawa, H. Taga, Y. Yoshida, and H. Wakabayashi, "Observation of BER degradation due to fading in long-distance optical amplifier system," *IEE Electron. Lett.*, vol. 29, pp. 209–210, Jan. 1993.

[19] J. Lee and Y. Chung, "Improved OSNR monitoring technique based on polarisation-nulling method," *IEE Electron. Lett.*, vol. 37, pp. 972–973, Jul. 2001.

[20] A. Chraplyvy, R. Thack, L. Buhl, and R. Alferness, "Phase modulation to amplitude modulation conversion of CW laser light in optical fibers," *IEE Electron. Lett.*, vol. 22, pp. 409–411, Apr. 1986.

[21] N. Liu, W.-D. Zhong, Y. Xiaoke, W. Yixin, and L. Chao, "Chromatic dispersion monitoring using the power ratio of two RF tones with a dispersion offset," *Proc. Opt. Fiber commun. Conf.*, vol. 1, pp. 23–27, Feb. 2004.

[22] I. Shake and H. Takara, "Chromatic dispersion dependence of asynchronous amplitude histogram evaluation of NRZ signal," *J. Lightwave Technol.*, vol. 21, pp. 2154–2161, Oct. 2003.

[23] N. Hanick, A. Gladisch, C. Caspar, and B. Strebel, "Application of amplitude histograms to monitor performance of optical channels," *IEE Electron. Lett.*, vol. 35, pp. 403–404, Mar. 1999.

[24] N. Kikuchi and S. Sasaki, "Polarization mode dispersion (PMD) detection sensitivity of degree of polarization method for PMD compensation," *Proc. ECOC*, vol. 2, pp. 8–9, Sep. 1999.

[25] E. Forestieri, G. Colavolpe, and G. Prati, "Novel MSE adaptive control of optical PMD compensators," *J. Lightwave Technol.*, vol. 20, pp. 1997–2003, Dec. 2002.

[26] M. Petersson, H. Sunnerud, M. Karlsson, and B.-E. Olsson, "Performance monitoring in optical networks using Stokes parameters," *IEEE Photon. Technol. Lett.*, vol. 16, pp. 686–688, Feb. 2004.

[27] R. Noe, D. Sandel, M. Yoshida-Dierolf, S. Hinz, V. Mirvoda, A. Schopflin, C. Gungener, E. Gottwald, C. Scheerer, G. Fischer, T. Weyrauch, and W. Haase, "Polarization mode dispersion compensation at 10, 20, and 40 Gb/s with various optical equalizers," *J. Lightwave Technol.*, vol. 17, pp. 1602–1616, Sep. 1999.

[28] N. Bergano, F. Kerfoot, and C. Davidsion, "Margin measurements in optical amplifier system," *IEEE Photon. Technol. Lett.*, vol. 5, pp. 304–306, Mar. 1993.

[29] R. Wiesmann, O. Bleck, and H. Heppner, "Cost effective performance monitoring in WDM systems," *Proc. Opt. Fiber commun. Conf.*, pp. 171–173, Mar. 2000.

[30] S. Otheru and N. Takachio, "Optical signal quality monitor using direct Q-factor measurement," *IEEE Photon. Technol. Lett.*, vol. 11, pp. 1307–1309, Oct. 1999.

[31] I. Shake, H. Takara, K. Uchiyama, and Y. Yamabayashi, "Quality monitoring of optical signals influenced by chromatic dispersion in a transmission fiber using averaged Q-factor evaluation," *IEEE Photon. Technol. Lett.*, vol. 13, pp. 385–387, Apr. 2001.

[32] M. Kossel and M. Schmatz, "Jitter measurements of high-speed serial links," *IEEE Des. Test. Comput.*, vol. 21, pp. 536–543, Nov.-Dec. 2004.

[33] D. Rouvillain, P. Brindel, F. Seguineau, L. Pierre, and O. Leclerc, "Optical 2R regeneratorbased on passive saturable absorber for 40 Gbit/s WDM long-haul transmissions," *IEE Electron. Lett.*, vol. 38, pp. 1113–1114, Sep. 2002.

[34] T. Otani, T. Miyazaki, and S. Yamamoto, "40-Gb/s optical 3R regenerator using electroabsorption modulators for optical networks," *J. Lightwave Technol.*, vol. 20, pp. 195–200, Feb. 2002.

[35] M. S. L. P. A. Bogoni, P. Ghelfi, "All-optical regeneration and demultiplexing for 160-Gb/s transmission systems using a NOLM-based three-stage scheme," *IEEE J. Select. Topics Quantum Electron.*, vol. 10, pp. 192–196, Jan.-Feb. 2004.

[36] M. Dülk, S. Fischer, E. Gamper, W. Vogt, E. Gini, H. Melchior, W. Hunziker, H. Poulsen, A. Clausen, A. Buxens, and P. Jeppesen, "Efficient regenerative wavelength conversion at 10 Gbit/s over C and L-band (80 nm span) using a Mach-Zehnder interferometer with monolithically integrated semiconductor optical amplifiers," *IEE Electron. Lett.*, vol. 36, pp. 241–243, Feb. 2000.

[37] M. Zhao, J. De Merlier, G. Morthier, and R. Baets, "Experimental demonstration at 10 Gbps of 2R regeneration in a fiber-based MZI with LOAs," *Proc. ECOC*, p. 7.3.6, Sep. 2002.

[38] D. Wolfson, A. Kloch, T. Fjelde, C. Janz, B. Dagens, and M. Renaud, "40 Gb/s all-optical wavelength conversion and regeneration and demultiplexing in an SOA-based all-active Mach-Zehnder interferometer," *IEEE Photon. Technol. Lett.*, vol. 12, pp. 332–334, Mar. 2000.

[39] Y. Ueno, S. Nakamura, and K. Tajima, "Penalty-free error-free all-optical data pulse regeneration at 84 Gb/s using a symmetric Mach-Zehnder-type semiconductor regenerator," *IEEE Photon. Technol. Lett.*, vol. 13, pp. 469–471, May 2001.

[40] P. Humblet and M. Azizoglu, "On the bit error rate of lightwave systems with optical amplifiers," *J. Lightwave Technol.*, vol. 9, pp. 1576–1582, Nov. 1991.

[41] I. Shake, H. Takara, S. Kawanishi, and Y. Yamabayashi, "Optical signal quality monitoring method based on optical sampling," *IEE Electron. Lett.*, vol. 34, pp. 2152–2154, Oct. 1998.

[42] K. Mueller, N. Hanik, A. G. H.-M. Foisel, and C. Caspar, "Application of amplitude histograms for quality of service measurements of optical channels and fault identification," *Proc. ECOC*, vol. 1, pp. 707–708, Sep. 1998.

[43] I. Shake and H. Takara, "Averaged Q-factor method using amplitude histogram evaluation for transparent monitoring of optical signal-to-noise ratio degradation in optical transmission system," *J. Lightwave Technol.*, vol. 20, pp. 1367–1373, Aug. 2002.

[44] M. Raszotovits-Wiech, K. Studer, and W. Leeb, "Bit error probability estimation algorithm for signal supervision in all-optical networks," *IEE Electron. Lett.*, vol. 35, pp. 1754–1755, Sep. 1999.

[45] P. André, A. Teixeira, M. J. N. Lima, J. L. Pinto, and R. F. Rocha, "Optical performance monitor based on asynchronous detection," *Proc IEEE Lasers and Electro Optics Society Annual Meeting*, pp. 30–31, Nov. 2001.

[46] I. Shake, E. O. andH. Takara, K. Uchiyama, Y. Yamabayashi, and T. Morioka, "Bitrate flexible optical signal quality monitoring utilizing optical sampling technique," *Proc. ECOC*, vol. 4, pp. 117–118, Sep. 2000.

[47] C. Anderson and J. Lyle, "Technique for evaluating system performance using Q in numerical simulations exhibiting intersymbol interference.," *IEE Electron. Lett.*, vol. 30, pp. 71–72, Jan. 1994.

[48] A. Teixeira, M. J. N. Lima, and R. F. da Rocha, "Bit error rate assessment in DWDM transparent optical networks using opti-

cal performance monitoring based on asynchronous sampling," *Proc. Opt. Fiber commun. Conf.*, pp. 749–750, Mar. 2002.

[49] T. Takahashi, M. Aoyama, M. Murakami, and M. Amemiya, "Modelling of intersymbol interference effect on signal to noise ratio measurement in long haul optical amplifier systems," *IEE Electron. Lett.*, vol. 31, pp. 2195–2197, Dec. 1995.

[50] C. Weinert, C. Caspar, M. Konitzer, and M. Rohde, "Histogram method for the identification and evaluation of crosstalk," *IEE Electron. Lett.*, vol. 36, pp. 558–559, Mar. 2000.

[51] N. Kikuchi, S. Hayase, K. Sekine, and S. Sasaki, "Performance of chromatic dispersion monitoring using statistical moments of asynchronously sampled waveform histograms," *IEEE Photon. Technol. Lett.*, vol. 17, pp. 1103–1105, May 2005.

[52] H. Chen, A. Poon, and X.-R. Cao, "Transparent monitoring of rise time using asynchronous amplitude histograms in optical transmission systems," *J. Lightwave Technol.*, vol. 22, pp. 1661–1667, Jul. 2004.

[53] P. André, A. Teixeira, M. J. N. Lima, R. Nogueira, R. F. Rocha, and J. L. Pinto, "Asynchronous sampled amplitude histogram model for optical performance monitoring in high speed network," *Proc IEEE Lasers and Electro Optics Society Annual Meeting*, vol. ThQ2, pp. 911–912, Oct. 2003.

[54] I. Shake, H. Takara, and S. Kawanishi, "Simple Q factor monitoring for BER estimation using opened eye diagrams captured by high-speed asynchronous electrooptical sampling," *IEEE Photon. Technol. Lett.*, vol. 15, pp. 620–622, Apr. 2003.

[55] M. Westlund, H. Sunnerud, M. Karlsson, and P. Andrekson, "Software-synchronized all-optical sampling for fiber communication systems," *J. Lightwave Technol.*, vol. 23, pp. 1088–1099, Mar. 2005.

[56] H. Takara, S. Kawanishi, A. Yokoo, S. Tomaru, T. Kitoh, and M. Saruwatari, "100 Gbit/s optical signal eye-diagram measurement with optical sampling using organic nonlinear optical crystal," *IEE Electron. Lett.*, vol. 32, pp. 2256–2258, Nov. 1996.

[57] J. Li, J. Hansryd, P. Hedekvist, P. Andrekson, and S. Knudsen, "300-Gb/s eye-diagram measurement by optical sampling using fiber-based parametric amplification," *IEEE Photon. Technol. Lett.*, vol. 13, pp. 987–989, Sep. 2001.

[58] C. Schmidt, C. Schubert, S. Watanabe, F. Futami, R. Ludwig, and H. Weber, "Complete optical sampling system with broad gap-free spectral range for 160 Gbit/s and 320 Gbit/s and its application in a transmission system," *Proc. ECOC*, p. 2.1.3, Sep. 2002.

[59] L. Noirie, F. Cérou, G. Moustakides, O. Audouin, and P. Peloso, "New transparent optical monitoring of the eye and BER using asynchronous under-sampling of the signal," *Proc. ECOC*, p. PD2.2, Sep. 2002.

[60] S. Verspurten, G. Morthier, and R. Baets, "Derivation of the amplitude histogram of an optical signal using an optical 2R regenerator," *Proc. ECOC*, pp. 678–679, Sep. 2003.

[61] G. Golub and C. V. Loan, *Matrix computations*. Johns Hopkins university press, 3rd ed. ed., 1996.

[62] "http://mathworld.wolfram.com/conditionnumber.html."

[63] P. Hansen, "Analysis of discrete ill-posed problems by means of the L-curve," *SIAM Review*, vol. 34, pp. 561–580, Dec. 1992.

[64] P. Hansen, "Regularization tools: A Matlab package for analysis and solution of discrete ill-posed problems," *Numerical Algorithms*, vol. 6, pp. 1–35, 1994.

[65] "http://www2.imm.dtu.dk/ pch/regutools/index.html."

[66] G. Golub, M. Heath, and G. Wahba, "Generalized cross-validation as a method for choosing a good ridge parameter," *Technometrics*, vol. 21, pp. 215–223, May 1979.

[67] A. Neumaier, "Solving ill-conditioned and singular linear systems: A tutorial on regularization," *SIAM Review*, vol. 40, pp. 636–666, Sep. 1998.

[68] G. Morthier, M. Zhao, B. Vanderhaegen, and R. Baets, "Experimental demonstration of an all-optical 2R regenerator with adjustable decision threshold and "true"regeneration characteris-

tics," *IEEE Photon. Technol. Lett.*, vol. 12, pp. 1516 – 1518, Nov. 2000.

[69] P. Doussiere, A. Jourdan, G. Soulage, P. Garabedian, C. Graver, T. Fillion, E. Derouin, and D. Leclerc, "Clamped gain travelling wave semiconductor optical amplifier for wavelength division multiplexing applications," *Proc. Int. Semiconduct. Laser Conf.*, pp. 185–186, Sep. 1994.

[70] M. Zhao, *All-optical signal regeneration based on Gain-Clamped Semiconductor Optical Amplifiers*. PhD thesis, Ghent University, 2002-2003.

[71] "www.avanex.com."

[72] J. De Merlier, G. Morthier, P. .Van Daele, I. Moerman, and R. Baets, "All-optical 2R regeneration based on an asymmetric Mach-Zehnder interferometer incorporating an MMI-SOA," *IEE Electron. Lett.*, vol. 38, pp. 238–239, Feb. 2002.

[73] K. Yashiki, K. Sato, T. Morimoto, S. Sudo, K. Naniwae, A. Satoshi, K. Shiba, N. Suzuki, T. Sasaki, and K. Kudo, "Wavelength-selectable light sources fabricated using advanced microarray-selective epitaxy," *IEEE Photon. Technol. Lett.*, vol. 16, pp. 1619–1621, Jul. 2004.

[74] W. D'Oosterlinck, G. Morthier, R. Baets, and M. Smit, "Very steep optical thresholding characteristic using a DFB laser diode and an SOA in an optical feedback scheme," *IEEE Photon. Technol. Lett.*, vol. 17, pp. 642–644, Mar. 2005.

[75] W. D'Oosterlinck, S. Verspurten, G. Morthier, R. Baets, and M. Smit, "Experimental demonstration at 10Gbit/s of a 2R-regenerator based on the mutual optical feedback," *IPRA*, p. IMC 2, Apr. 2005.

[76] H. Ishii, H. Oohashi, K. Kasaya, K. Tsuzuki, and Y. Tohmori, "High-power (40mW) L-band tunable DFB laser array module using current tuning," *Proc. Opt. Fiber commun. Conf.*, p. OTuE1, Mar. 2005.

[77] S. Verspurten, G. Morthier, and R. Baets, "Experimental and numerical small-signal analysis of two types of gain-clamped semi-

conductor optical amplifiers," *IEEE J. Quantum Electron.*, vol. 42, pp. 302–312, Mar. 2006.

[78] D. Francis, S. Dijaili, and J. Walker, "A single chip linear optical amplifier," *Proc. Opt. Fiber commun. Conf.*, p. PD13, Mar. 2001.

[79] J. Oksanen and J. Tulkki, "On crosstalk and noise in an optical amplifier with gain clamping by vertical laser field," *J. Lightwave Technol.*, vol. 21, pp. 1914–1919, Sep. 2003.

[80] L. Tiemeijer, P. Thijs, T. van Dongen, J. Binsma, E. Jansen, and H. van Helleputte, "Reduced intermodulation distortion in 1300 nm gain-clamped MQW laser amplifiers," *IEEE Photon. Technol. Lett.*, vol. 7, pp. 284–286, Mar. 1995.

[81] J. C. E. Tangdiongga, L. Spiekman, G. van den Hoven, and H. de Waardt, "Performance analysis of linear optical amplifiers in dynamic WDM systems," *IEEE Photon. Technol. Lett.*, vol. 14, pp. 1196–1198, Aug. 2002.

[82] H. Lee, J. Oh, D. Lee, G. Lee, and S. Hwang, "Demonstration of 16 x 10 Gb/s WDM transmission over 4 x 40 km of SMF using linear optical amplifiers combined with Raman-pumped dispersion compensation fibers under dynamic add/drop situations," *IEEE Photon. Technol. Lett.*, vol. 16, pp. 1576–1578, Jun. 2004.

[83] M. Zhao, J. De Merlier, G. Morthier, and R. Baets, "All-optical 2R regeneration based on polarization rotation in a linear optical amplifier," *IEEE Photon. Technol. Lett.*, vol. 15, pp. 305–307, Feb. 2003.

[84] E. Tangdiongga, J. Turkiewicz, G. Khoe, and H. de Waardt, "Clock recovery by a fiber ring laser employing a linear optical amplifier," *IEEE Photon. Technol. Lett.*, vol. 16, pp. 611–613, Feb. 2004.

[85] J. Sun, G. Morthier, and R. Baets, "Numerical and theoretical study of the crosstalk in gain clamped semiconductor optical amplifiers," *IEEE J. Select. Topics Quantum Electron.*, vol. 3, pp. 1162–1167, Oct. 1997.

[86] X. Jin, T. Keating, and S. L. Chuang, "Theory and experiment of high-speed cross-gain modulation in semiconductor lasers," *IEEE J. Quantum Electron.*, vol. 36, pp. 1485–1493, Dec. 2000.

[87] C.-Y. Jin, Y.-Z. Huang, L.-J. Yu, and S.-L. Deng, "Numerical and theoretical analysis of the crosstalk in linear optical amplifiers," *IEEE J. Quantum Electron.*, vol. 41, pp. 636 – 641, May 2005.

[88] D. Tong, M. Wu, and S. Dijaili, "Intrinsic intermodulation distortion characteristics of linear optical amplifier," *Conf. Lasers and Electro-Optics*, pp. 1414–1416, Jun. 2003.

[89] C.-Y. Jin, Y.-Z. Huang, L.-J. Yu, and S. Deng, "Detailed model and investigation of gain saturation and carrier spatial hole burning for a semiconductor optical amplifier with gain clamping by a vertical laser field," *IEEE J. Quantum Electron.*, vol. 40, pp. 513–518, May 2004.

[90] M. Asghari, I. H. White, and R. V. Penty, "Wavelength conversion using semiconductor optical amplifiers," *J. Lightwave Technol.*, vol. 15, pp. 1181–1190, Jul. 1997.

[91] L. Schares, C. Schubert, C. Schmidt, H. G. Weber, L. Occhi, and G. Guekos, "Phase dynamics of semiconductor optical amplifiers at 10-40 GHz," *IEEE J. Quantum Electron.*, vol. 39, pp. 1394–1408, Nov. 2003.

[92] K. Petermann, *Laser diode modulation and noise*. Kluwer Academic Publishers, 1988.

[93] P. Vankwikelberge, G. Morthier, and R. Baets, "CLADISS-a longitudinal multimode model for the analysis of the static, dynamic, and stochastic behavior of diode lasers with distributed feedback," *IEEE J. Quantum Electron.*, vol. 26, pp. 1728–1741, Oct. 1990.

[94] G. Morthier, J. Sun, T. Gyselings, and R. Baets, "A novel optical decision circuit based on a Mach-Zehnder or Michelson interferometer and gain-clamped semiconductor optical amplifiers," *IEEE Photon. Technol. Lett.*, vol. 10, pp. 1162–1164, Aug. 1998.

[95] T. Durhuus, B. Mikkelsen, C. Joergensen, S. Danielsen, and K. Stubkjaer, "All-optical wavelength conversion by semiconductor optical amplifiers," *J. Lightwave Technol.*, vol. 14, pp. 942–954, Jun. 1996.

[96] V. Annovazzi-Lodi, A. Scire, M. Sorel, and S. Donati, "Dynamic behavior and locking of a semiconductor laser subjected to external injection," *IEEE J. Quantum Electron.*, vol. 34, pp. 2350 – 2357, dec. 1998.

[97] M. Nielsen, D. Blumenthal, and J. Mørk, "A transfert function approach to the small-signal response of saturated semiconductor optical amplifiers," *J. Lightwave Technol.*, vol. 18, pp. 2151–2157, Dec. 2000.

[98] D. Marcenac and A. Mecozzi, "Switches and frequency converters based on cross-gain modulation in semiconductor optical amplifiers," *IEEE Photon. Technol. Lett.*, vol. 9, pp. 749–751, Jun. 1997.

[99] G. Morthier, R. Schatz, and O. Kjebon, "Extended modulation bandwidth of DBR and external cavity lasers by utilizing a cavity resonance for equalization," *IEEE J. Quantum Electron.*, vol. 36, pp. 1468–1475, Dec. 2000.

[100] J. Mørk, F. Öhman, and S. Bischoff, "Analytical expression for the bit error rate of cascaded all-optical regenerators," *IEEE Photon. Technol. Lett.*, vol. 15, pp. 1479–1481, Oct. 2003.

[101] T. Durhuus, C. Joergensen, B. Mikkelsen, and K. Stubkjaer, "Penalty free all-optical wavelength conversion by SOA's in Mach-Zehnder configuration," *Proc. ECOC*, pp. 129–132, Sep. 1993.

[102] R. Schreieck, M. Kwakernaak, H.Jackel, and H. Melchior, "All-optical switching at multi-100-Gb/s data rates with Mach-Zehnder interferometer switches," *IEEE J. Quantum Electron.*, vol. 38, pp. 1053–1061, Aug. 2002.

[103] A. Labrousse, *Conception et caractérisation d'interferomètres de Mach-Zehnder à base d'amplificateurs optiques à semiconducteur pour la régénération 3R "tout-optique"à haut débit (40Gbps)*. PhD thesis, U.F.R. de Sciences et Technique, Université de Rouen, 2003.

[104] M. Nielsen, M. Nord, M. Petersen, B. Dagens, A. Labrousse, R. Brenot, B. Martin, S. Squedin, and M. Renaud, "40 Gbit/s standard-mode wavelength conversion in all-active MZI with very fast response," *IEE Electron. Lett.*, vol. 39, pp. 385–386, Feb. 2003.